DYNAMICS AND MIXING IN A MICROTIDAL, WIND-DRIVEN ESTUARY

David Marshall

A dissertation submitted to the faculty at the University of North Carolina at Chapel Hill in partial fulfillment of the requirements for the degree of Doctor of Philosophy in the Department of Marine Sciences.

Chapel Hill
2018

Approved by:

Johanna Rosman

Jim Hench

Rick Luettich

Harvey Seim

John Bane

ABSTRACT

David Marshall: Dynamics and mixing in a microtidal, wind-driven estuary
(Under the direction of Johanna Rosman)

In estuaries, tides are considered to be the dominant mechanism driving the mixing of freshwater from rivers with the saline waters from the adjoining ocean, hence determining the along-estuary salinity gradient and strength of estuarine circulation. However, there are a number of microtidal estuaries, driven primarily by the wind and not tides. These estuaries are prone to human-induced water quality problems, as the episodic nature of wind leads to less vertical mixing and strong stratification, which when combined with eutrophication results in bottom-water hypoxia. This dissertation research aims to further our understanding of the dynamics and mixing in these wind-driven estuaries. Through field measurements collected in the Neuse River Estuary in 2013 and 2016, we first investigate the along-channel momentum and salt budgets to determine the primary balances in a wind driven estuary. Then we define a new set of mixing parameters to compare it to classical tidal estuaries. Finally, we characterize the nature and efficiency of turbulent mixing produced in the Neuse.

ACKNOWLEDGEMENTS

TABLE OF CONTENTS

LIST OF FIGURES

SUMMARY

Most previous work on the physical processes in estuaries has focused on tides as the primary mixing mechanism. However, there is a family of microtidal estuaries, driven primarily by the wind, which are not as well understood. Due to the episodic nature of the wind, vertical mixing is often weak, resulting in strong salinity stratification. In this dissertation, field studies were conducted to investigate the effects of time-varying, unsteady winds on circulation, salt transport and turbulent mixing in the Neuse River Estuary, one of these microtidal, wind-driven estuaries in eastern North Carolina.

The focus of the first field study was to investigate the circulation and salt transport in the Neuse. An analysis of the depth-averaged momentum equation demonstrated that the primary balance was between the wind stress and barotropic pressure gradient, indicating the presence of a wind-generated barotropic seiche. During periods of strong stratification, there was a two-layer circulation pattern, in which the wind stress was balanced by a combination of the interfacial stress, bottom stresses, and interfacial tilt. Up-estuary winds reduced the stratification and reduced or reversed the exchange flow, briefly causing a net transport of salt into the estuary until the water column became vertically mixed. Down-estuary winds enhanced the exchange flow and increased stratification, except when the wind stress was strong enough to overcome stratification and directly mix the water column. This asymmetric response to the predominantly down-estuary winds enhanced exchange flow, which when combined with a decrease in freshwater discharge, resulted in an observed net salt influx.

1

A new set of parameters were defined in order to compare the physics of a wind-driven estuary to classical tidal estuaries. Due to a wide range of wind speeds and durations, the Neuse experiences varying amounts of mixing, and thus can be classified differently, depending on the wind conditions. Strong winds resulted in well-mixed conditions, while weak winds generally resulted in strongly stratified conditions. Straining by moderate down-estuary winds caused the Neuse to behave like a wind-induced SIPS estuary.

In a second field study in the Neuse, we observed some of the strongest stratifications reported in estuaries, yet high turbulent dissipation rates. However, the observed turbulence was scarce and estimates of turbulent length scales indicated that the overturns were often so small that it was difficult to quantify the effects buoyancy and shear on turbulence properties. Application of a recently proposed framework suggested that some of the observed turbulence fell into an inertia-dominated regime, in which the turbulence was decaying, and eddies were no longer large enough to be affected by buoyancy or shear. Dissipation was generally larger than production and the mixing efficiencies associated with this turbulence were generally quite small. Turbulent mixing was more efficient in the shear and buoyancy-dominated regimes.

The observed turbulence in this study was generated by two distinct mechanisms: shear generation, associated with advection of a salt wedge, and wind mixing. The turbulence associated with the salt wedge appeared to be generated prior to being advected past the sensors. Most this turbulence appeared to have been decaying at the observed locations, and fell into an inertia-dominated regime with inefficient mixing. The turbulence generated by wind-shear in the upper part of the water, on the other hand, was generally anisotropic, occurring in the shear and buoyancy-dominated regimes. During periods of strong stratification this wind-generated turbulence produced efficient mixing.

CHAPTER 1: MOMENTUM AND SALT BUDGETS IN A WIND-DRIVEN, MICROTIDAL ESTUARY

Introduction

Estuaries are complex systems, driven by a variety of mechanisms, including freshwater flow, tides, and wind, which can produce energetic turbulence and strong density gradients. Averaging over short term variations in velocity, such as those produced by tides, reveals that estuaries are characterized by an exchange flow, in which there is a persistent outflow (seaward) at the surface and a persistent inflow (landward) near the bottom. This exchange flow transports salt to the coastal ocean at the surface, while importing salt near the bottom. Vertical mixing is important in maintaining the estuarine circulation and salt flux, as mixing affects the strength of the exchange flow.

Most previous work on estuarine circulation has focused on tides as the primary mixing mechanism (reviewed by MacCready and Geyer 2010, Geyer and MacCready 2014). Budgets of momentum and salt in these tidal systems have been studied extensively, dating back to Hansen and Rattray (1965). Despite the complexities of estuarine circulation, which include nonlinear coupling of velocity and density structures, classical analyses often simplify momentum and salt budgets to a single cross-section. In doing so, it is assumed that the along-channel variation in bathymetry is negligible, and the along-channel salinity gradient is constant over the cross-section.

The classical along-channel momentum budget (Hansen and Rattray, 1965) assumes a balance between the pressure gradient and the turbulent shear stress. The pressure gradient is composed of a barotropic and a baroclinic term, while the stress is expressed in terms of an eddy

viscosity and vertical shear. This along-channel momentum budget can be further simplified to a one-layer model, by integrating the momentum equation over the water depth. The only stress terms that remain are the bottom stress and surface wind stress. In fact, wind is traditionally ignored, so the only the bottom stress retained in a one-layer model. Although a one-layer model is often appropriate for well-mixed and some partially mixed estuaries (e.g., Chatwin, 1976), where the along-channel salinity gradient drives the exchange flow, in strongly stratified and salt wedge estuaries, the stress between the surface outflow and bottom inflow can have a large effect on the dynamics. To resolve the exchange flow, a two-layer model can be constructed by dividing the water column into two layers and then computing momentum balances for each layer (Geyer, 2000; Geyer and Ralston, 2011). An equation describing the dynamics of the exchange flow is obtained from the difference between the top and bottom layer momentum budgets. The differential flow between the top and bottom layers is driven entirely by the baroclinic pressure gradient, since the barotropic pressure gradient affects both layers equally and is eliminated by subtraction.

Because of the dynamical importance of the baroclinic pressure gradient term, the estuarine momentum budget is strongly coupled with the salt budget. As cast in Lerczak (2006), the salt budget consists of three terms: the salt loss due to river flow, the salt flux due to exchange flow, and tidal salt flux which has the form of a dispersion term. Increasing river flow pushes the salt intrusion seaward and increases the horizontal salinity gradient. The magnitude of this increase in along-estuary salinity gradient depends on the responses of the exchange flow and tidal salt fluxes to the increase in horizontal salinity gradient.

The coupled momentum and salt budgets reveal that the vertical shear is important to the creation and destruction of stratification. This mechanism, sometimes referred to as strain-

induced periodically stratification (SIPS), occurs when tidal variations in vertical shear drive

tidal variations in stratification (tidal straining). Hence, tidal variations in vertical mixing have

an important effect on the exchange flow (Simpson, 1990). The ratio of potential energy

generation due to straining of the density field by velocity shear in the bottom boundary layer

during ebb tide to production of turbulent kinetic energy by mixing in the bottom boundary layer

is traditionally quantified by the horizontal Richardson number (Simpson, 1990)

$$Ri_x = \frac{H^2 N_x^2}{u_{*b}^2} \tag{1.1}$$

where H is the water depth, u_{*b} is the bottom friction velocity, $N_x^2 = \frac{g}{\rho_0} \frac{\partial \langle \bar{\rho} \rangle}{\partial x}$, g is the gravitational

acceleration, ρ_0 is a constant reference density, and $\langle \bar{\rho} \rangle$ is the cross-sectionally averaged density.

When Ri_x is small, mixing in the boundary layer destroys stratification, leading to a well-mixed

water column. High values of Ri_x lead to runaway stratification, as straining generates

stratification that cannot be mixed by bottom boundary layer turbulence. In SIPS estuaries, Ri_x

takes intermediate values, as the water column becomes stratified during ebb tides and well

mixed during flood tides (Geyer and MacCready, 2014).

In order to quantify the effectiveness of mixing at the bottom boundary, it is necessary to

compute both the strength of the turbulent mixing and the time period over which that mixing

occurs, because the bottom boundary layer grows in height over a tidal cycle. Despite its merits,

Ri_x accounts for the strength, but not the time scale of mixing, and therefore is not suitable for

explaining how much of the water column becomes mixed. Geyer and MacCready (2014)

parameterized the growth of the bottom boundary layer analogously to the growth of a wind-

mixed layer:

$$\frac{dh_{BL}}{dt} = C \frac{u_{*b}^2}{N_\infty h_{BL}} \tag{1.2}$$

where h_{BL} is the height of the bottom boundary layer, N_∞ is the stratification above the bottom boundary, and $C \approx 0.6$ is a constant related to the mixing efficiency (Kato and Phillips, 1969; Trowbridge, 1992). They define a mixing number, M to determine the conditions in which the bottom boundary layer will extend into the entire water column within a half tidal cycle.

$$M^2 = \frac{u_{*b}^2}{\omega N_0 H^2} \tag{1.3}$$

where $N_0 = \sqrt{\beta g s_{ocean}/H}$ is the buoyancy frequency for maximum top-to-bottom salinity variation in an estuary, β is the coefficient of saline contraction, s_{ocean} is the salinity of ocean water, and ω is the tidal frequency. A mixing number $M \geq 1$ corresponds to bottom boundary layer growth to entire water column in a half tidal cycle. Geyer and MacCready (2014) proposed an estuarine classification scheme based on tidal mixing (M), and the freshwater inflow (Fr_f). Here $Fr_f = u_R/\sqrt{\beta g s_{ocean} H}$, is the freshwater Froude number which represents the ratio of river inflow to strength of the gravitational circulation and u_R is the velocity due to freshwater flow. By placing estuaries in $Fr_f - M$ parameter space (Fig. 1.16), they can be classified as salt wedge (e.g., Mississippi, Ebro), time dependent-salt wedge (e.g., Frasier, Merrimack), strongly stratified (e.g., Chesapeake, Hudson), partially stratified (e.g., James, San Francisco Bay), SIPS (e.g., Conwy, Willapa Bay), fjord (e.g., Puget Sound, Long Island Sound), or bay (e.g., Narragansett Bay). Several estuaries (e.g., Hudson, Chesapeake, San Francisco Bay) span partially mixed and strongly stratified, salt wedge, or SIPS during the spring-neap cycle.

In the above estuarine budgets, parameterizations, and classifications, wind has been neglected. However, there is increasing recognition that wind can also have important effects on mixing and circulation in estuarine systems. In fact, there is an entire family of microtidal estuaries in which tides are not the dominant mixing mechanism and it is the wind that drives

mixing and circulation patterns (e.g., Luettich et al., 2002). Unlike tides, the wind is inherently irregular and episodic, making it much more difficult to express the estuarine dynamics with simple models.

Much of what is known about the dynamics of shallow wind-driven systems originates from the study of stratified lakes (e.g., Spigel and Imberger, 1980; Bouffard et al., 2012). Unsteady winds can initiate barotropic and baroclinic motions by changes in wind forcing, which can continue to contribute to advection and modify stratification after a wind event. Wind blowing over the surface of a lake both generates a turbulent, wind-mixed layer and induces a vertically sheared circulation pattern that results in tilts of both the water surface and isopycnals. The relative strengths of the maximum baroclinic pressure gradient force associated with a fully titled pycnocline and the force due to the surface wind stress can be quantified by the Wedderburn number (Thompson and Imberger, 1980; Monismith, 1985)

$$W = \frac{g'h_1}{u_{*w}{}^2 L} \tag{1.4}$$

where g' is the reduced gravity, h_1 is the height of the surface wind-mixed layer, u_{*w} is the wind-generated surface friction velocity, and L is the length of the water body. The Wedderburn number is a measure of whether complete upwelling will occur. When $W > 1$, mixed layer deepening does not affect the baroclinic seiche motions (Spigel and Imberger, 1980). When $W < 1$, unsteady interfacial shear stress contributes to mixing. If the winds become strong enough ($W << 1$), the mixed layer deepens from the surface to the bottom and the lake is no longer stratified.

More recently, studies have considered wind effects in tidally dominated estuaries by focusing on steady wind forcing and mixing by turbulence generated by wind stress (Scully et al., 2005; Chen and Sanford 2009). These studies showed that wind-driven advection has significant effects on density stratification and the strength of the exchange flow. Wind stress

drives vertically sheared flow with the strongest speeds typically near the surface, enhancing

stratification for down-estuary winds and reducing stratification for up-estuary winds (Geyer,

1997; Scully et al. 2005). These effects on stratification feed back to the mixing (Chen and

Sanford 2009). Stronger stratification during down-estuary winds limits mixing and supports

larger vertical shear than when winds are directed up-estuary. Chen and Sanford (2009) defined a

modified version of the horizontal Richardson number to characterize the relative importance of

straining and mixing, due to the combined effects of tides and wind. They found that this

parameter was able to capture how the stratification increased and then decreased with increasing

down-estuary winds. From observations in Chesapeake Bay, Xie and Li (2018) found an

asymmetric stratification response, in which stratification decreased linearly with W for up-

estuary winds, but stratification was a parabolic function of W for down-estuary winds,

increasing at moderate wind speeds and decreasing at high wind speeds. Changes in wind speed

or direction have also been found to result in large transient salt fluxes (Chen and Sanford,

2009).

A recent study of a lagoonal estuary using a 3-D hydrodynamic model has given some

insights into the circulation dynamics of estuaries that are not just modulated, but driven by the

wind (Jia and Li, 2012). They found that the circulation was primarily driven by a balance

between the total pressure (barotropic plus baroclinic) gradient and stress divergence (wind stress

minus bottom stress). They also found that the baroclinic forcing was highly asymmetric

between up-estuary and down-estuary winds, which supports the findings of other studies that

the wind can strain the density field.

Despite these advances in our understanding of how wind modulates turbulent mixing,

estuarine circulation, and salt transport in estuaries, there is a clear need to determine the extent

to which these findings can be applied to real strongly stratified, wind-driven estuaries. This study used field measurements to investigate the effects of time-varying, unsteady winds on circulation and salt transport in a wind-driven estuary. We investigate whether the findings of the modeling studies (Chen and Sanford, 2009; Jia and Li, 2012) that wind can both strain and mix the water column are important in a real estuary. Secondly, we investigate whether the frameworks (one and two-layer momentum budgets, salt budgets, and the Fr_f–M parameter space) that have been used to understand and classify tidally mixed estuaries can also be used to understand a system where wind is the primary agent driving mixing and short time-scale advection.

Methods

Field Site

The Neuse River Estuary (NRE), in eastern North Carolina, is a shallow, microtidal estuary, driven largely by wind and freshwater discharge. The estuary is approximately 70 km long, with a mean width of about 6.5 km, a mean depth of about 3.5 m, and a prominent bend approximately mid-estuary (Fig. 1.1). The NRE connects to Pamlico Sound, a large, lagoonal estuary, which is isolated from the Atlantic Ocean by the Outer Banks barrier islands, except for limited tidal exchange through three small inlets. While the NRE has weak tidal influence and low freshwater discharge, its large fetch allows wind to be the main driver of flow patterns and turbulent mixing. The prevailing wind direction is northeast – southwest, aligned with main axis of the lower Neuse. During the summer, the NRE becomes episodically strongly salinity stratified, with salinity differences of as much as 15 PSU between the top and bottom, and experiences bottom water hypoxia due to eutrophication and lack of mixing (Paerl et al., 1998). Despite this lack of tides, the NRE-Pamlico Sound system has episodic oscillatory flow arising

from wind-driven barotropic seiches with a period of about 13 hours (Luettich et al., 2002). Typical depth-averaged oscillatory velocities are about 10 cm/s.

Field Measurements

The study was conducted over a one-month period from June 9 to July 4, 2016 in the lower part of the NRE. We deployed an array of sensors at three sites along the main channel from the bend in the estuary to the mouth of Pamlico Sound (Fig. 1.1). The instruments at the bend and central sites were deployed in the deepest part of the channel, while those at the mouth were deployed on a shoal for logistical reasons.

At each of those sites, we made continuous measurements of currents and salinity with a bottom-mounted ADCP (Teledyne-RD Instruments 1.2-MHz Workhorse Monitor) and a vertical mooring of three CTDs (SeaBird SBE-37SMP). The ADCPs sampled every 1 second, and were deployed in fast-pinging rate mode, with 6 subpings per profile (mode 12; Nidzieko et al., 2006). Velocities were recorded in beam coordinates for the entire water column (6-7 m) in 25-cm vertical bins, the first of which was centered 1.5 m above bottom. At each mooring the lower CTD was located at 1 m above bottom, the middle CTD at half of the water depth, and the top CTD at 1.5 to 2-m below the water surface. The CTDs sampled at 5-minute intervals.

Additionally, at the central site, we deployed an Autonomous Vertical Profiler (AVP). The AVP is a floating platform that lowers a CTD (EXO2 Sonde, YSI) at a constant rate of 0.01 m/s from the surface to the bottom to measure vertical profiles of water quality data at high temporal resolution for extended periods (Reynolds-Fleming et al, 2002, Whipple et al. 2006). AVP profiles of temperature and salinity were measured at 30-min intervals and binned at 10-cm resolution. The AVP was also equipped with an anemometer 5 m above the water surface that

recorded wind speed and direction at 30-minute intervals. Additionally, hourly atmospheric pressure data were obtained from the Marine Corps Air Station at Cherry Point.

To quantify the cross-sectional spatial structure of salinity and currents, we made measurements along transects at 10-12 equally-spaced stations (0.5 km apart) across the estuary at each of the three main sites in the Lower Neuse (Fig. 1.1). These shipboard measurements were collected on 5 days (6/20, 7/5, 7/18, 8/16, and 9/19), many of which extended beyond the main study period. Velocity profiles were measured with a boom-mounted (Hench et al., 2000) shipboard ADCP (1.2 MHz Workhorse, RD Instruments), and CTD profiles were made at the same stations (SBE19plus V2, Seabird Electronics). At each station ADCP data were collected for six minutes in mode 1, with 0.25 m bins and a ping rate of 1Hz, yielding an uncertainty of 0.0072 m/s. Although the vessel was nominally stopped at each station, the remaining vessel motion was removed using ADCP bottom tracking. At the same time, a single CTD cast was conducted with a sampling rate of 4 Hz.

Data Processing

The ADCP and CTD data were 30-minute ensemble averaged such that the middle of each interval coincided with the AVP profiles. Wind speeds at the AVP site collected at 5 m above the surface were transformed to 10-m wind speeds (for wind stress calculations) assuming an atmospheric log profile (Blanton et al, 1989). Both the ADCP velocity data and the wind velocity data were rotated into along- and across-channel directions, determined from the principal components of the depth-averaged ADCP velocities. To compute velocities averaged over the entire water column, velocities were extrapolated to the surface (0.5 m) assuming zero velocity gradient at the surface and a log-layer at the bottom of the water column. The assumption of a zero velocity gradient is only valid when there is no surface wind stress.

11

Depth-averaged values of salinity, temperature, and density were computed from the AVP profiles at the central site and from the CTD moorings at the bend and mouth sites. All three CTDs at the mouth site were in the top layer during periods of stratification, so values were extrapolated to the bottom of the channel by assuming that along-estuary gradients were constant throughout the entire water column. Thus, the magnitude of the vertical density gradient at the mouth was equal to the vertical density gradient at the central site.

Shipboard CTD measurements were averaged in 0.1 m bins, resulting in profiles with the same resolution as those collected by the AVP. These shipboard measurements were then used to estimate cross-sectionally averaged values of depth, velocity, salinity, and density based on the continuous measurements from the moored ADCP and AVP. First, depth-averaged values were computed for each station (both channel and non-channel stations in Fig. 1.2). An offset was assigned to each station by computing the difference between the value at that station and the value at the station closest to the moored instruments. For depth-averaged velocity, that is $\bar{u}_{Si} = \bar{u}_{CL} + \sigma_{ui}$, where $\bar{u}_{Si}$ is the depth averaged velocity at station i (i=1:10 for the bend and central transects and i=1:12 for the mouth transect), $\bar{u}_{CL}$ is the depth-averaged velocity at the station closest to the moored centerline instruments, and σ_{ui} the velocity offset for station i. Likewise, an offset for the depth at each station was computed from the difference between the station depth and the depth of the station closest to the moored instruments. This process of calculating offsets was repeated for each of the five days on which shipboard measurements were collected to get an average offset for all parameters at every station. These offsets were then added to the measurements from the moored instruments to get estimated values at each station. Isopycnals and isohalines were assumed to be level across the cross section and thus determined by the AVP

profiles. Finally, cross-sectional averages of velocity, salinity, and density were computed from the station-estimated values. For the cross-sectionally averaged velocity, $\langle \bar{u} \rangle$

$$\langle \bar{u} \rangle = \frac{\sum_{i=1}^{N} \bar{u}_{Si} H_i d_i}{A} \tag{1.5}$$

where N is the number of stations, H_i is the estimated depth at each station, computed by applying an offset to the depth at the location of the moored instruments, d_i is the distance between stations, and A is the cross-sectional area. Cross-sectionally averaged values of salinity and density were computed from equations of the same form as equation 1.5. Using centerline values and assuming horizontal isotachs resulted in estimates of cross-sectionally averaged velocities that were an average of about 1 cm/s (20 %) slower than those computed using offsets derived from the shipboard measurements, in which the isotachs were not horizontal.

Uncertainties were estimated for velocity, density, wind speed, and water depth measurements for each 30-minute interval. These uncertainties were used to calculate the uncertainties in the terms of the momentum budgets via a propagation of uncertainty formula (Taylor, 1996). The standard deviation the mode-12 ADCP velocities was 1.44 cm/s (Teledyne RD Instruments, 2006). Ensemble averaging over 30-minute intervals resulted in a standard error of 8 x 10^{-4} m/s. The instrument error in a salinity measurement was 1% (YSI Incorporated, 2017), which corresponded to a density error of 0.2 kg/m^3. Assuming an average of 10 salinity measurements per 10-cm bin, the density error for each bin was 0.06 kg/m^3. The uncertainties in the water depth were computed as the standard deviation of the water depth over the 30-minute interval, resulting in an uncertainty of 7 mm. The uncertainty in wind speed was computed assuming an instrument error of 2 % for the wind velocity measurements. These computed instrument errors serve as a lower bound for the uncertainty, as there was additional uncertainty associated with computing cross-channel averages from point measurements.

Results

Experimental conditions

During the study period, winds were typically oriented along the axis of the estuary (NE-SW direction) (Fig. 1.3a). The lower Neuse was strongly stratified by salinity for the majority of the field experiment (Fig. 1.3b), except during periods of strong winds. During periods when the water column was stratified, profiles of along-channel velocity were strongly vertically sheared. The current at the surface was generally aligned with the wind direction (Fig. 1.3c).

The average shipboard measurements for the central site are shown in Fig. 1.4. The channel was typically strongly stratified by salinity (Fig. 1.4c), although stations on the shoals were often so shallow that they only contained the top layer. As a result only the six stations in the middle of the channel were used when computing the two-layer model (Fig. 1.2). The largest vertical shears in the along-channel (Fig. 4 a) and cross-channel (Fig. 1.4b) directions were typically co-located with the pycnocline.

During periods of strong stratification, the gradient Richardson numbers which were typically greater than 0.25 near the pycnocline (Fig. 1.3d), indicating that the flow was stable. However, near the surface and bottom, $Ri_g < 0.25$. Periods of weak stratification, which were associated with strong winds, resulted in more uniform velocity profiles, and $Ri_g < 0.25$ throughout the water column. On semidiurnal time scales, a wind-driven barotropic seiche drove flow reversals in the along-channel direction. Freshwater discharge, as measured at a USGS station (Fort Barnwell) approximately 110 km upstream of the mouth, was low throughout the field experiment. Freshwater flow rates ranged from 20 to 150 m^3/s, which corresponds to velocities of 0.1 to 0.7 cm/s at the central site, after correcting for the assumption that 69 % of the freshwater discharge was gaged (Peierls et al., 2012).

Time series of the Wedderburn number (Fig. 1.3e) show that the wind stress was large

relative to the maximum achievable baroclinic pressure gradient force (W<<1), indicating that

wind stress was an important forcing mechanism. Weak down-estuary winds enhanced the

stability by straining the water column and increasing exchange flow (Fig. 1.3 a-c). However,

when the down-estuary wind was sufficiently strong (June 21-23), Richardson numbers were less

than 1/4 throughout the water column indicating that shear was sufficient to overcome the

stratification and mix the water column. Up-estuary wind events acted against the estuarine

exchange flow, causing the exchange flow to reverse, before disappearing altogether as the water

column mixed and the velocity uniform throughout the water column (June 17-20, 26-28).

Cross-Sectionally Averaged Momentum Budget

To understand the underlying mechanisms driving the kinematical characteristics of an estuary,

the dynamics were explored through the analysis of the momentum budget in the along-channel

direction, which is given by:

$$\frac{\partial u}{\partial t} + u\frac{\partial u}{\partial x} + v\frac{\partial u}{\partial y} + w\frac{\partial u}{\partial z} - fv + \frac{1}{\rho_0}\frac{\partial p}{\partial x} - \frac{1}{\rho_0}\left(\frac{\partial \tau_{xx}}{\partial x} + \frac{\partial \tau_{xy}}{\partial y} + \frac{\tau_{xz}}{\partial z}\right) = 0 \qquad (1.6)$$

where x is the along-channel direction with positive values in the upstream direction, u is the

along-channel velocity, v is the cross-channel velocity, $f = 8.34$ x 10^{-5} s^{-1} is the local Coriolis

parameter, and τ_{xx}, τ_{xy}, and τ_{xz} are the Reynolds stresses, $\rho(\overline{u'u'})$, $\rho(\overline{u'v'})$, $\rho(\overline{u'w'})$. The

pressure gradient, $\partial p/\partial x$ can be decomposed to express the influence of the surface slope and the

horizontal density gradient:

$$\frac{1}{\rho_0}\frac{\partial p}{\partial x} = g\frac{\partial \eta}{\partial x} + \frac{g}{\rho_0}\int\frac{\partial \rho}{\partial x}dz \qquad (1.7)$$

where η is the free surface displacement, and ρ is the density. The cross-sectionally averaged

momentum equation is derived by combining equations 1.6 and 1.7, integrating over the cross-

section, and dividing by the cross-sectional area. Following Speer (1985), the cross-sectionally averaged momentum equation is:

$$\frac{\partial \langle \bar{u} \rangle}{\partial t} + \langle \bar{u} \rangle \frac{\partial \langle \bar{u} \rangle}{\partial x} + g \frac{\partial \eta}{\partial x} + \frac{g}{A\rho_0} \int_{-b_1}^{b_2} \int_{-h}^{\eta} \frac{\partial \rho}{\partial x} z \, dz \, dy - f\langle \bar{v} \rangle + \frac{\tau_{bx} P}{\langle \bar{\rho} \rangle A} - \frac{\tau_{wx}}{\langle \bar{\rho} \rangle H} = 0 \qquad (1.8)$$

where the overbar and brackets represents a cross-sectional average, h is the local water depth, and H is the cross-sectionally averaged water depth, A is the cross-sectional area, P is the wetted perimeter, τ_{bx} is the along-channel bottom stress, and τ_{wx} is the along-channel surface wind stress. The limits of integration, b_1 and b_2, are the y-coordinates at the two shores, such that the width of the estuary, $B = b_1 + b_2$.

In deriving the terms in equation 1.8, Speer (1985) assumed that the horizontal density gradient was negligible and thus ignored the fourth term in the equation. However, this term may be important in the present study site., Here we derive the full cross-sectionally averaged baroclinic pressure gradient term. Applying Leibniz's rule,

$$\frac{g}{A\rho_0} \int_{-b_1}^{b_2} \int_{-h}^{\eta} \frac{\partial \rho}{\partial x} z \, dz \, dy = \frac{g}{A\rho_0} \left[\begin{array}{c} \dfrac{d}{dx} \displaystyle\int_{-b_1}^{b_2} \int_{-h}^{\eta} \rho z \, dz \, dy - \dfrac{\partial b_2}{\partial x} \displaystyle\int_{-h}^{\eta} \rho_{b_2} z_{b_2} \, dz \\[2mm] + \dfrac{\partial(-b_1)}{\partial x} \displaystyle\int_{-h}^{\eta} \rho_{b_1} z_{b_1} \, dz \\[2mm] + \displaystyle\int_{-b_1}^{b_2} \rho(\eta) \eta \dfrac{\partial \eta}{\partial x} \, dy + \dfrac{d}{dx} \displaystyle\int_{-b_1}^{b_2} \rho(-h) h^2 dy \\[2mm] + \dfrac{\partial b_2}{\partial x} \rho(-h_{b_2}) h_{b_2}{}^2 - \dfrac{\partial b_1}{\partial x} \rho(-h_{b_1}) h_{b_1}{}^2 \end{array} \right] \qquad (1.9)$$

Here, b_1 and b_2 appear as subscripts to indicate quantities at $y = b_1$ or $y = b_2$. The fourth term is approximately zero, assuming $\eta \ll h$. If there is a gradual slope in the cross-channel direction, the depth at the boundaries is approximately zero, so terms 2, 3, 6, and 7 are zero. The baroclinic pressure gradient term reduces to:

$$\frac{g}{A\rho_0} \int_{-b_1}^{b_2} \int_{-h}^{\eta} \frac{\partial \rho}{\partial x} z \, dz \, dy = \frac{g}{A\rho_0} \left[\frac{d}{dx} \int_{-b_1}^{b_2} \int_{-h}^{\eta} \rho z \, dz \, dy + \frac{d}{dx} \int_{-b_1}^{b_2} \rho(-h) h^2 dy \right] \qquad (1.10)$$

Both terms on the RHS were estimated using the shipboard measurements from 5 transects (June to September, 2016), The last term was 2 orders of magnitude smaller than the first, so the baroclinic term can be reduced to:

$$\frac{g}{A\rho_0}\int_{-b_1}^{b_2}\int_{-h}^{\eta}\frac{\partial\rho}{\partial x}z\,dz\,dy = \frac{g}{A\rho_0}\frac{d}{dx}\int_{-b_1}^{b_2}\int_{-h}^{\eta}\rho z\,dz\,dy \qquad (1.11)$$

Next, let $\rho = \langle\bar\rho\rangle + \bar\rho + \dot\rho$, where $\langle\bar\rho\rangle$ is the cross-channel averaged density, $\bar\rho$ is the depth averaged and width varying density, and $\dot\rho$ is the depth and width varying density:

$$\frac{gd}{A\rho_0 dx}\int_{-b_1}^{b_2}\int_{-h}^{\eta}\rho z\,dz\,dy$$

$$= \frac{g}{A\rho_0}\left[\frac{d}{dx}\int_{-b_1}^{b_2}\int_{-h}^{\eta}\langle\bar\rho\rangle z\,dz\,dy + \frac{d}{dx}\int_{-b_1}^{b_2}\int_{-h}^{\eta}\bar\rho z\,dz\,dy + \frac{d}{dx}\int_{-b_1}^{b_2}\int_{-h}^{\eta}\dot\rho z\,dz\,dy\right]$$

$$= \frac{g}{2A\rho_0}\left[BH^2\frac{d\langle\bar\rho\rangle}{dx} + \frac{d}{dx}\int_{-b_1}^{b_2}\bar\rho h^2\,dy + 2\frac{d}{dx}\int_{-b_1}^{b_2}\int_{-h}^{\eta}\dot\rho z\,dz\,dy\right] \qquad (1.12)$$

Estimating the cross-sectionally averaged term (first term on the RHS of equation 1.12) and the full depth integrated term (LHS of equation 1.12) from the shipboard data indicated that the cross-sectionally averaged term accounted for approximately 1/3 of the baroclinic pressure gradient. This difference in baroclinic pressure gradient estimates may be due to large uncertainty introduced by averaging values measured two-weeks apart, as well as estimating the cross-channel gradients from stations that were 0.5 km apart. To account for the difference, a Boussinesq coefficient, $\beta = 3$, was applied to the cross-sectionally averaged baroclinic pressure gradient term to get a better estimate of the total contribution of the baroclinic pressure gradient. That is:

$$\frac{g}{A\rho_0}\frac{d}{dx}\int_{-b_1}^{b_2}\int_{-h}^{\eta}\rho z\,dz\,dy \approx \frac{\beta g}{2A\rho_0}BH^2\frac{d\langle\bar\rho\rangle}{dx} \qquad (1.13)$$

A similar empirical coefficient could be applied to each of the terms in equation 1.8, however, the shipboard measurements indicated that the differences between the terms computed using measurements at the centerline, multiplied by the cross-sectional area, and the true cross-sectionally averaged terms were negligible.

Assuming that $A \approx BH$, the cross-sectionally averaged momentum equation becomes:

$$\frac{\partial \langle \bar{u} \rangle}{\partial t} + \langle \bar{u} \rangle \frac{\partial \langle \bar{u} \rangle}{\partial x} + g \frac{\partial \eta}{\partial x} + \frac{\beta g}{2 \rho_0} \frac{\partial \langle \bar{\rho} \rangle}{\partial x} H - f \langle \bar{v} \rangle + \frac{\tau_{bx} P}{\langle \bar{\rho} \rangle A} - \frac{\tau_{wx}}{\langle \bar{\rho} \rangle H} = 0 \qquad (1.14)$$

The terms on the left-hand side are the local acceleration, the nonlinear advective acceleration, the barotropic pressure gradient force, the baroclinic pressure gradient force, the Coriolis acceleration, the bottom stress, and the wind stress.

To compute the barotropic pressure gradient term, the baroclinic contribution to the pressure measurements recorded by the ADCPs was first removed using a method similar to Geyer et al. (2000). First, the depth-integrated density, derived from AVP profiles, was used to compute the total pressure, and subsequently the height of the water column. η was computed at each site by subtracting off the time-averaged water column height (averaged over the course of the entire field study). Finally, the free surface gradient was computed at the central site from the pressure measurement recorded by all three ADCPs, using second-order central differencing

$$\frac{d\eta}{dx} = \frac{\left((x_{cent} - x_{bend}) \frac{\eta_{mouth} - \eta_{cent}}{x_{mouth} - x_{cent}} + (x_{mouth} - x_{cent}) \frac{\eta_{cent} - \eta_{bend}}{x_{cent} - x_{bend}} \right)}{(x_{mouth} - x_{bend})} \qquad (1.15)$$

Likewise, this differencing method was used to calculate the depth-averaged velocity gradient from the ADCP data and the depth-averaged horizontal density gradient from the CTD arrays at the bend and mouth sites and the YSI profiles at the central site.

The surface wind stress in the along-estuary direction was estimated using wind data from the AVP's anemometer and assuming a parabolic model of the drag coefficient of the form $C_{Dw} = -A(U_{10} - 33)^2 - c$ (Peng and Li, 2015). Here, C_{Dw} is the drag coefficient associated with the surface wind stress, U_{10}, is the wind speed 10 m above the surface, and $A = 7$ x 10^{-7} and $c = 2.34$ x 10^{-3} are empirical coefficients. Over the course of the study C_{Dw} ranged from 1.6 x 10^{-3} to 2.1 x 10^{-3}. The bottom stress in the along-channel direction was estimated using a quadratic drag law: $\tau_{bx} = \rho C_D |u_{bx}| u_{bx}$, where C_D is the bottom drag coefficient and u_{bx} is the near bottom along-channel velocity. Here, C_D is assumed to be 2.5 x 10^{-3}, which is typical of sand-bottomed estuaries, (Proudman, 1953; Prandle, 2003) and u_{bx} is the along-channel velocity in the first bin recorded by the ADCP (about 1.5 m above bottom).

Time series of each term in the cross sectionally-averaged momentum budget are shown in Fig. 1.5a. At low frequencies (periods > 30 hours), the primary balance is between the surface wind stress and barotropic pressure gradient (Fig. 1.5b,d). Although the residual term is also quite large throughout the time series, its large uncertainties indicate that it rarely differs significantly from zero. As the wind blows steadily over the surface of the estuary, the water moves in the direction of the wind until the slope of the water surface balances the wind stress. The adjustment time needed for the water surface to come into balance with the wind stress, T_s, can be estimated as $T_s = 1/2L(gH)^{-1/2}$, where L is the length of the estuary (Spigel and Imberger, 1980). Both the length of the lower Neuse and the length of Pamlico Sound are included in the estuarine length ($L \approx 140$ km), resulting in an adjustment time of approximately 2.5 hours. A cross-correlation analysis of the time series of the wind stress and barotropic pressure gradient terms did indeed show this 2.5 hour lag. At intermediate frequencies (6-18 hours), a barotropic

seiche signal dominates the momentum budget, and appears as a balance between the local

acceleration term and the barotropic pressure gradient term (Fig. 1.5 c,e).

Multi-taper spectra of each term were computed to further understand these balances

(Fig. 1.6). Low frequencies are dominated by the barotropic pressure gradient (green) and wind

stress (pink) terms. At intermediate frequencies there is a balance between the barotropic

pressure gradient and local acceleration. The highest frequencies (periods < 6 hours) are

dominated by the wind stress, barotropic pressure gradient, local acceleration, and residual terms

terms (Fig. 1.6), as unsteady winds accelerate the water for brief periods of time and generate

transient gradients in the water surface.

Two-layer momentum budget

Throughout most of the measurement period, the water column consisted of two layers

with distinctly different salinities, separated by an interface of varying thickness. We therefore

decided to apply a two-layer model to better understand the dynamics. A two-layer model is

most appropriate if the widths of both layers are approximately equal. Due to the shape of the

central cross-section, the two-layer model was therefore only applied to the channel, which was

defined as the area between the middle six shipboard stations (Fig. 1.2).

To further determine the validity of a two-layer model, it is important to consider the

hydraulics of the system. The hydraulics of the two-layer system are described by the composite

Froude number:

$$G^2 = F_1^2 + F_2^2 = \frac{u_1^2}{g'h_1} + \frac{u_2^2}{g'h_2} \tag{1.16}$$

where F_1 and F_2 are the layer Froude numbers (Armi and Farmer, 1986). When $G^2 < 1$, the flow

is subcritical and therefore a two-layer model is appropriate. If $G^2 > 1$, the flow is supercritical

and the two-layer model is not appropriate. Together, G^2 and g' were used to determine when the two-layer model was applicable. Time series of the Froude numbers (Fig. 1.8a) and g' (Fig. 1.14c) indicated that a two-layer model was not appropriate for a 5-day period between 6/18 and 6/23, where the flow was either supercritical or the water column was well-mixed. The two-layer momentum budget was therefore not applied during this period (Fig. 1.8 b-c).

The water column was divided into two layers by defining the interface as the height above bottom at which the maximum vertical salinity gradient was observed. (Fig. 1.7a). Velocities and densities were then averaged over each layer. Surface and bottom layer velocities often exhibited typical estuarine circulation, although during periods of strong winds, both layers had the same velocity (Fig. 1.7b). Layer-averaged densities indicate that stratification was strong for much of the field study, except for a 5-day period from 6/18 to 6/23 when strong winds mixed the water column (Fig. 1.7c).

Following Geyer and Ralston (2011), the along-channel momentum budget for each layer can be written as:

$$\frac{\partial u_1}{\partial t} + u_1 \frac{\partial u_1}{\partial x} + g \frac{\partial \eta}{\partial x} + \frac{C_i |u_1 - u_2|(u_1 - u_2)}{h_1} = 0 \qquad (1.17)$$

$$\frac{\partial u_2}{\partial t} + u_2 \frac{\partial u_2}{\partial x} + g \frac{\partial \eta}{\partial x} + g' \frac{\partial h_i}{\partial x} + \frac{C_i |u_1 - u_2|(u_1 - u_2)}{h_2} + \frac{C_D |u_2| u_2}{h_2} = 0 \qquad (1.18)$$

where h_1 and h_2 are the heights of the upper and lower layers, u_1 and u_2 are the upper and lower layer velocities, ρ_1 and ρ_2 are the upper and lower layer densities, $g' = \frac{g(\rho_2 - \rho_1)}{\rho_0}$ is the reduced gravity, $\frac{\partial h_i}{\partial x}$ is the slope of the interface between the two layers, and C_i is an interfacial drag coefficient. However, these layer equations are incomplete when applied to a wind-driven estuary with a strong horizontal density gradient. In order to account for the wind, a wind stress

21

term, $\frac{u_{*w}^2}{h_1}$ was added to the layer 1 equation. By restricting the two-layer model to stations in

which there were always two layers, the wind stress should not directly affect layer 2, nor should

the bottom stress directly affect layer 1. Shipboard measurements indicated that the horizontal

density gradient was approximately equal for both layers, so a baroclinic pressure gradient term,

$\int \frac{\partial \rho}{\partial x} z dz$, was included in each layer. The baroclinic pressure gradient in the top layer was

integrated from the surface to h_1 and in the bottom layer from h_1 to H. Finally, a momentum sink

term was added to each layer to account for any momentum lost due to lateral exchange between

the channel and the shoals. This momentum sink term is the Reynolds stress at the edge of the

channel (y = B) and can be parameterized using an eddy viscosity, A_H:

$$\overline{u'v'} = A_H \frac{\partial u_i}{\partial y} \approx A_H \frac{\Delta u_i}{\Delta y} \tag{1.19}$$

where Δu_i is the difference in layer velocities between the channel and the shoal for each of the

two layers (i=1,2). Alternatively, the Reynolds stress can be parameterized with a drag

coefficient, C_{S1}, such that $\overline{u'v'} = C_{S1} \Delta u_1{}^2$. By equating the two parameterizations of the

Reynolds stress, we get:

$$C_{S1} = \frac{A_H}{\Delta u_1 \Delta y} \tag{1.20}$$

A mixing length model can be used as a scaling estimate for the horizontal eddy viscosity (Pope,

2000):

$$A_H = l_m^2 \frac{\Delta u_1}{\Delta y} \tag{1.21}$$

where l_m is the mixing length. Replacing A_H with the mixing length model,

$$C_{S1} = \frac{l_m^2}{\Delta y^2} \tag{1.22}$$

Both l_m and Δy scale as the width of the shear layer between the channel and the shoal, so $C_{S1} \approx$ 1. Replacing ∂y with B in the top layer momentum equation, and using the drag coefficient parameterization, we have get the following layer-averaged equations:

$$\frac{\partial u_1}{\partial t} + u_1 \frac{\partial u_1}{\partial x} + g \frac{\partial \eta}{\partial x} + \frac{C_i |u_1 - u_2|(u_1 - u_2)}{h_1} - \frac{u_{*w}^2}{h_1} + \frac{g h_1}{2\rho_0} \frac{\partial \rho}{\partial x} + \frac{2 C_{S1} |\Delta u_1| \Delta u_1}{B} = 0 \quad (1.23)$$

$$\frac{\partial u_2}{\partial t} + u_2 \frac{\partial u_2}{\partial x} + g \frac{\partial \eta}{\partial x} + g' \frac{\partial h_i}{\partial x} - \frac{C_i |u_1 - u_2|(u_1 - u_2)}{h_2} + \frac{C_D |u_2| u_2}{h_2} + \frac{g(H + h_1)}{2\rho_0} \frac{\partial \rho}{\partial x}$$
$$+ \frac{2 C_{S2} |\Delta u_2| \Delta u_2}{B} = 0 \quad (1.24)$$

Δu_i was estimated from the shipboard measurements by computing the difference between the last station in the channel and the first station outside of the channel at each end of the estuary (stations 2-3 and 8-9). The average values of $|\Delta u_1|$ and $|\Delta u_2|$ were 0.02 and 0.09 m/s respectively, which are comparable to the magnitudes of the other velocities in the equation. Since $\frac{C_{S1}}{C_D} \sim \frac{B}{H}$, the momentum sink term should be about the same order of magnitude as the other terms in the equation.

Taking the difference between the two layer-averaged equations eliminates the barotropic pressure gradient term, resulting in the final two-layer expression of the baroclinic dynamics:

$$\frac{\partial}{\partial t}(u_2 - u_1) + u_2 \frac{\partial u_2}{\partial x} - u_1 \frac{\partial u_1}{\partial x} + g' \frac{\partial h_i}{\partial x} - C_i |u_1 - u_2|(u_1 - u_2) \left(\frac{1}{h_1} + \frac{1}{h_2} \right) + \frac{C_D |u_2| u_2}{h_2}$$
$$+ \frac{|u_{*w}| u_{*w}}{h_1} + \frac{gH}{2\rho_0} \frac{\partial \bar{\rho}}{\partial x} - \frac{2 C_{S1} |\Delta u_1| \Delta u_1}{B} + \frac{2 C_{S2} |\Delta u_2| \Delta u_2}{B} = 0 \quad (1.25)$$

The terms on the left-hand side are the local differential acceleration between layers, the nonlinear advection of the bottom layer, the nonlinear advection of the top layer, the pressure gradient caused by the tilting interface, the interfacial stress, the bottom stress, the surface wind stress, the baroclinic pressure gradient associated with the along-channel density gradient, and the lateral momentum sinks in the upper and lower layers.

23

To compute each of these terms, velocities and densities were estimated at each of the shipboard stations using the same offset method explained previously. However, instead of computing offsets for depth-averaged values, offsets were calculated for layer-averaged values. Density measurements from the AVP were used to divide the water column in two, at the depth of the maximum vertical salinity gradient, and it was assumed that the isopycnals were horizontal across the channel. At the central site, this resulted in 20 different regions (2 for each of the 10 stations) over which velocities and densities could be estimated. However, the two-layer model requires that the widths of both layers be the same, so only the 6 stations in the channel (Fig. 1.2) were used to compute the layer-averaged velocities and densities. By restricting estimates of layer-averaged velocities to the channel, cross-sectional averaged estimates only differed from the centerline velocity estimates by 0.003 m/s (4 %).

The shear stress between two layers is defined as:

$$\frac{\partial}{\partial z}\overline{u'w} \tag{1.26}$$

Assuming that the momentum flux is determined by the velocity gradient between the top and bottom layers, the Reynolds stress can be parameterized with a vertical eddy viscosity:

$$\overline{u'w'} = A_z \frac{\partial u}{\partial z} \approx A_z \frac{u_1 - u_2}{\Delta z} \tag{1.27}$$

The Reynolds stress can also be considered in the context of friction between the two layers and therefore parameterized with an interfacial drag coefficient, $C_i : \overline{u'w'} = C_i|u_1 - u_2|(u_1 - u_2)$ With both parameterizations of the Reynolds stress, we find that

$$C_i = \frac{A_z}{(u_1 - u_2)\Delta z} \tag{1.28}$$

The vertical eddy viscosity can be modeled with a mixing length (Pope, 2000), such that

$$A_z = l_m^2 \frac{(u_1 - u_2)}{\Delta z} \qquad (1.29)$$

Therefore,

$$C_i = \frac{l_m^2}{\Delta z^2} \qquad (1.30)$$

Here Δz corresponds to the interface thickness. The mixing length is unknown, but in a stratified

fluid, it can be much smaller than the interface thickness. Without good turbulence

measurements, it is difficult to accurately measure the value of C_i. Krvavica et al. (2016) were

able to estimate C_i empirically from bulk Reynolds and Richardson numbers in the Rječina River

estuary, but noted that their parameterizations were not applicable to other estuaries. Without an

accurate parameterization of the interfacial drag coefficient, a constant value of $C_i = 5.0$ x 10^{-4}

was chosen, which is in line with values reported in estuaries and river plumes (Geyer et. al,

2017; Krvavica et al., 2016; MacDonald and Geyer, 2004). However, this value should increase

as mixing between the two layers increases the interface thickness. The lateral momentum sink

terms, likewise cannot be estimated from the data, and may be important considering that scaling

estimates put these terms on the same order of magnitude as the others.

The tilt in the interface is typically computed as the residual of all of the other terms.

However, due to the large uncertainties involved, the residual is not a reliable estimate of the

interface tilt term. Each of the terms in the two-layer model were estimated as described above,

while the interface tilt, lateral friction, and uncertainty were included in the residual term.

At low frequencies (periods > 30 hours), the primary balance is between the surface wind

stress and the combined interfacial stress, bottom stress, and residual (Fig. 1.8c). Over the course

of a given down-estuary wind event, the wind stress seems to balance the other three terms in a

sequential pattern from the top of the water column to the bottom. First, the wind stress is

balanced by the interfacial stress, then the bottom stress, and finally the residual. This progression indicates that at first only the top layer is accelerated by the wind, which strains the density field and enhances exchange flow. At this point the increased flow at the bottom is counteracted by friction. On the other hand, during the only moderate up-estuary wind event, the wind stress is balanced first by the bottom stress and then by the residual, but not by the interfacial stress. In this case, the bottom stress reduces the exchange flow immediately. This suggests enhancement of the exchange flow during down estuary winds, but not during up-estuary winds is important in generating interfacial stress. During weak to moderate winds, scaling arguments indicate that $\partial h_i/\partial x \approx H/(x_{mouth} - x_{bend})$ or $\partial h_i/\partial x \sim 10^{-4}$ and the interface tilt could account for most of the residual. During strong wind events, the residual term was an order of magnitude greater than the interfacial tilt term, indicating large error in the estimates of one or more terms. Spectra of the terms in the two-layer model further show a balance between the wind stress and the combined effect of the interfacial stress, bottom stress, and residual (Fig. 1.9). At higher frequencies, the acceleration between layers comes into balance with the residual term. Assuming that a large part of the residual could be explained by interface tilt, it is possible that the acceleration of the exchange flow is balanced by the interfacial tilt. Overall, this suggests that the baroclinic term associated with the along-channel density gradient is not significant in driving the exchange flow, at any of these time-scales. Instead, it appears that the exchange flow was driven primarily by the asymmetric response to the along-estuary wind.

It should be noted that there is a fair amount of uncertainty associated with the computation of the terms of in the momentum budgets from field measurements (Fig. 1.5, 1.8). Long distances between the three sites (bend, central, mouth) and complex bathymetry complicate estimates of along-channel gradients in velocities and densities. Additionally, a lack

of continuous measurements across the channel introduces uncertainty to any cross-sectional estimates. Computations of wind stresses, requires the selection of a surface drag coefficient from one of dozens of parameterizations available in the literature. Finally, two-layer models require the reduction of a continuously stratified salinity field, which is continuously modified by mixing and entrainment, to two homogeneous layers. Thus, the difference between the real system and the modeled system contributes to the uncertainty of the estimates.

Salt Flux

In a wind-driven estuary, the magnitude and direction of the wind are important drivers for the transport of salt, and therefore likely have important effects on the salinity distribution in the estuary. The total salt flux is typically averaged over a 30-hr period to remove the short term fluctuations associated with tides. This 30-hr averaging period was also appropriate for the NRE, despite the lack of tides, because it averages over the oscillations due to barotropic seiches, while still resolving most of the wind events. The total time-averaged salt flux is given by $F_S = \langle \int \int uSdA \rangle$, where the angle brackets represent a low-pass filter, S is the salinity and A is the cross-sectional area. Following Lerzcak (2006), the total salt flux can be decomposed into three components: salt flux associated with 1) the low-pass filtered and cross-sectionally averaged velocity and salinity, 2) the low-pass filtered and cross-sectionally varying velocity and salinity, and 3) the time-varying (high-frequency) and cross-sectionally varying velocity and salinity (Lerczak, 2006; Devkota and Fang, 2015).

The low-pass filtered and cross-sectionally averaged velocity (u_0) and salinity (S_0) are defined as:

$$u_0 = \frac{\langle \int udA \rangle}{A_0} = \frac{-Q_f}{A_0}, \qquad S_0 = \frac{\langle \int SdA \rangle}{A_0} \qquad (1.31)$$

where $A_0 = \langle \int dA \rangle$ is the low-pass filtered cross-sectional area, and $-Q_f = \langle \int u dA \rangle$ is the low-frequency volumetric flow rate through the cross-sectional area. The low-pass filtered and cross-sectionally varying velocity (u_E) and salinity (S_E) are defined as:

$$u_E = \frac{\langle u dA \rangle}{\langle dA \rangle} - u_0, \quad S_E = \frac{\langle S dA \rangle}{\langle dA \rangle} - S_0 \tag{1.32}$$

Finally, the time-varying and cross-sectionally varying velocity (u_T) and salinity (S_T) are:

$$u_T = u - u_0 - u_E, \quad S_T = S - S_0 - S_E \tag{1.33}$$

The total low-frequency salt flux can be expressed using these three components:

$$F_S = \langle \int \int (u_0 + u_E + u_T)(S_0 + S_E + S_T) dA \rangle \tag{1.34}$$

By definition, $\int u_E \langle dA \rangle = 0$, $\int S_E \langle dA \rangle = 0$, $\langle u_T dA \rangle = 0$, and $\langle S_T dA \rangle = 0$, this simplifies to:

$$F_S = \langle \int \int (u_0 S_0 + u_E S_E + u_T S_T) dA \rangle \tag{1.35}$$

$$F_S = F_0 + F_E + F_T \tag{1.36}$$

where $F_0 = -Q_f S_0$ is the salt flux associated with the low frequency, cross-sectionally averaged velocity, which includes salt lost to river transport. The salt flux due to estuarine circulation is represented by F_E. The final term is the salt flux due to correlations between high frequency velocity and salinity variations (F_T).

Terms were computed using the shipboard measurements for the central transect and dividing each of the 6 channel stations (Fig. 1.2) into two layers, which allowed for the computation of F_E and its components at the surface and bottom. Thus, u_{E1} and S_{E1} and the exchange velocities and salinities in the top layer integrated over all 6 stations. Similarly, u_{E2} and S_{E2} correspond to the values in the bottom layer integrated across the channel.

In the NRE, the wind stress (Fig. 1.10a) appears to be the primary driver of the components of the cross-sectionally averaged salt flux, F_0, as it was strongly correlated with the volumetric flow

rate, Q_f (Fig. 1.10c). However, there was a 4.5 hour lag in the correlation, which can be interpreted as the time need for the wind stress to accelerate the entire water column. Initially, only the top layer is accelerated by the wind, but over time this strains the salinity field and modifies the exchange flow. The lag between the wind stress and the volumetric flow rate reflects the time for this process to occur.

The freshwater discharge, Q_R (Fig. 1.10b), was also important, as higher freshwater flow rates at the beginning of the field experiment increased the strength of Q_f. On the other hand, freshwater flow appears to have been of primary importance to the cross-sectionally averaged salinity, S_0, as a decrease in Q_R coincided with an increase in S_0. The wind stress also appears to affect S_0 over short periods of time. Importantly, unlike most estuaries (e.g., Lerczak, 2006), the freshwater flow rate was not the dominant driver of F_0 during this particular time period.

The components of the salt flux due to exchange flow are shown in Fig. 1.11. The effects of wind direction on exchange flow are evident in the time series of u_E (Fig. 1.11a). Down-estuary winds sharply increased the difference between u_E at the surface and bottom, while up-estuary winds caused u_{E1} and u_{E2} to converge to zero. The strongest up-estuary wind reversed the exchange flow (6/18 – 6/20). The values of S_E were less sensitive to changes in wind direction, as stratification persisted, except when the wind was strong enough to completely mix the water column.

Time series of the terms in the salt flux equation show that the total salt flux was dominated by F_0 (Fig. 1.12a). As was the case with u_E, peaks in F_E largely occurred during down-estuary wind events, which are known to enhance estuarine circulation (Fig. 1.12b). The salt flux due to correlations between high frequency variations in u and S, which are mainly associated with the seiche, remained near zero throughout the field experiment.

The effects of wind speed and direction along the axis of the estuary can be further understood by examining the evolution of the stratification and velocity during strong up-estuary and down-estuary wind events (Fig. 1.13). As the wind ramped up in the up-estuary direction (Fig. 1.13a), the surface set up (Fig. 1.13g). The exchange flow became increasingly negative (Fig. 1.13c), with the top layer moving upstream relative to the bottom layer, resulting in a depth-averaged up-estuary flow. This pushed more salt upstream in the top layer (Fig. 1.13e), which decreased the density difference between layers until they became well mixed on June 18 (Fig. 1.13b). As the wind began to die down, the barotropic pressure gradient drove a down-stream depth-averaged current, and the baroclinic pressure gradient returned the exchange flow to a normal, positive direction. Subsequently, fresher water was transported downstream and saltier water was transported upstream, increasing stratification and advecting salt back downstream (Fig. 1.13i).

At the onset of a down-estuary wind event (Fig. 1.13b), the water surface set down (Fig. 1.13h) and positive exchange flow was enhanced (Fig. 1.13f), increasing stratification (Fig. 1.13d), and resulting in an down-estuary depth-averaged current. As the down-estuary wind reaches peak wind stress (6/22), it becomes strong enough to directly mix the water column, decreasing stratification and exchange flow. Eventually the wind speed decreases to the point that it again enhances the stratification, resulting in a positive exchange flow, pushing salt into the estuary (Fig. 1.13j). These results are consistent with the modeling and mechanisms identified by Chen and Sanford (2009) and Xie and Li (2018).

Over the entire measurement period, there was a net influx of salt (Fig. 1.12b), which was driven partially by F_0 due to net upstream flow and partially by F_E, representing the estuarine exchange flow. It is likely that this net inflow was the result of the particular conditions observed

during this time period. In the long term, there should be zero net influx of salt to maintain a steady state. F_E resulted in a consistent net up-estuary salt flux, driven by down estuary winds, which generally enhance exchange flow, while any reverse exchange driven by up-estuary winds get shut down quickly. F_T was approximately zero over the course of the experiment.

Discussion

In the Results section, we demonstrated that the wind is the dominant forcing in the lower NRE, especially at low frequencies (periods > 30 hours). Importantly, during large wind events, the baroclinic term was negligible in the two-layer momentum budget, which suggests that it is not significant in driving the exchange flow. Instead, the exchange flow appeared to be driven primarily by the asymmetric response to the along estuary wind. We found that wind stress enhanced the exchange flow and increased stratification during down-estuary winds, but reduced or even reversed exchange flow with up-estuary winds, thus decreasing stratification. The wind, in effect, strained or mixed the water column, much like tides do in SIPS estuaries. The standard Ri_x, quantifies tidal straining, and therefore cannot be applied directly to wind straining in the NRE. We instead define a new wind horizontal Richardson number by replacing the bottom stress with the wind stress:

$$Ri_{xw} = \frac{H^2 N_x^2}{u_{*w}^2} \tag{1.37}$$

This new ratio represents the competition between wind straining of the horizontal density gradient and wind mixing, where small values of Ri_{xw} indicate that wind mixing is larger than wind straining for down estuary winds. The time series of Ri_{xw} (Fig. 1.14a) shows that destruction of stratification by mixing exceeded stratification generation by straining during the down estuary wind events with the strongest wind stresses (low Ri_{xw}). Weak down-estuary

31

events resulted in $Ri_{xw} > 1$, indicating that stratification generation by wind straining exceeded stratification destruction by wind mixing.

Like its tidal counterpart, Ri_{xw} does not provide information about the effectiveness of mixing, as it does not take into account the time over which mixing occurs and hence the growth of the wind-mixed layer. The mixing number M was defined by Geyer and MacCready (2014) to quantify the degree of mixing generated in the bottom boundary layer in tidal estuaries. However, it does not account for the wind and interfacial mixing that our two-layer model indicated are important in the NRE. To account for these mechanisms, we define two new mixing numbers:

$$M_w{}^2 = \frac{u_{*w}{}^2}{\omega_w N_0 H^2} \tag{1.38}$$

$$M_i{}^2 = \frac{C_i(u_2 - u_1)^2}{\omega_i N_0 H^2} \tag{1.39}$$

where M_w and M_i are the wind and interfacial mixing numbers. The definition of M can also be modified such that ω doesn't correspond to the tidal frequency, but simply to the period of time since the bottom friction velocity changed direction. Likewise, ω_w and ω_i each correspond to the period of time since the surface friction velocity and exchange flow changed directions. Time series of the three mixing numbers, M, M_w, and M_i indicate that mixing was generated mostly by wind (Fig. 1.14d), though significant mixing was also produced in the bottom boundary and interfacial layers.

A fourth mixing number, M_{tot}, can be defined as the maximum of the wind, bottom, and interfacial mixing numbers. This total mixing number can be interpreted as the ratio of the timescale of the dominant mixing mechanism (wind stress, bottom stress, or interfacial stress) to the time scale for vertical mixing to occur over the entire water column height. In other words, it

quantifies the effect of the dominant mixing mechanism on a stratified estuary. However, M_{tot} is not perfectly analogous to M, as defined by Geyer and MacCready (2014), due to the fact that ω does not represent the frequency of an oscillatory velocity. Instead, oscillations are defined by changes in the direction of the velocities. In a wind-driven system, like the NRE, this means that M_{tot} resets to zero every time the wind changes direction. Since the wind is irregular and episodic, there were inevitably times in which the estuary was well-mixed, despite low values of M_{tot}, because the estuary had not yet restratified after the previous wind mixing event. While this memory effect is unavoidable, its effects can be reduced by computing the average stratification over an entire mixing event, rather than using every observation.

Neither M nor Ri_{xw} alone provide complete information about mixing, because M does not capture whether straining or mixing is the dominant mechanism, and Ri_{xw} does not consider the time over which mixing occurs. Thus, both parameters are necessary to provide a complete picture of mixing. To explore how stratification varies with Ri_{xw} and M, we plotted g' (Fig. 1.15a,b) and the change in g' since the beginning of the wind event, $\Delta g'$, (Fig. 1.15c,d) for up-estuary and down-estuary wind events. Here, a wind event starts each time the along-channel wind stress reverses direction. The parameter space can be divided into four quadrants. In Quadrant I, straining dominates, but occurs over a short period of time. In Quadrant II, straining dominates, and occurs over a long period of time. In Quadrant III, mixing dominates and penetrates the entire water column, while in Quadrant IV mixing dominates, but only penetrates part of the water column. For up estuary winds, straining reduces stratification, while for down-estuary winds, straining strengthens stratification. Up-estuary winds resulted in less stratification (Fig. 1.15a,b) and a greater decrease in stratification (Fig. 1.15c,d) than down-estuary winds. For down-estuary winds, low mixing numbers generally resulted in increases in stratification in both

quadrants I and IV (Fig. 1.15b,d), regardless of whether mixing or straining dominated in the surface boundary layer (Ri_x). For events in quadrant III, corresponding to boundary layer growth over the whole water depth and mixing dominating over straining, stratification generally decreased. The most interesting observations fall into quadrant II in (Fig. 1.15b,d), where although mixing numbers are high, wind straining dominates over mixing, increasing the stratification.

A computation of the average value of M_{tot} over the course of a single wind event also allows a wind-driven estuary, such as the Neuse, to be placed in the $Fr_f - M$ parameter space first proposed by Geyer and MacCready (2014). While M_{tot} is not a perfect analogue to M, as discussed above, the NRE still fits reasonably well into the parameter space. Unlike tidally driven estuaries, which fit in a small area of the parameter space, the Neuse varies from strongly stratified to well mixed, depending on the strength and direction of the wind during a particular wind event (Fig. 1.16a). Consistent with the findings from the momentum budget, down estuary wind events tended to increase stratification, even for high values of M_{tot} (Fig. 1.16b). On the other hand, up-estuary winds decreased the stratification. With low freshwater discharge rates, the classification scheme suggests that the Neuse should behave like a strongly stratified estuary during weak winds. Given that some straining occurs at high mixing numbers, it is also likely that the observations during strong wind events that occur in the well-mixed region, would more appropriately fall into the SIPS regime. This would indicate that M_{tot} tends to overestimate M during strong wind events.

Given the results of the momentum and salt flux budgets, it is encouraging to find that this estuarine classification scheme predicts that the NRE will behave like a number of different classes of estuaries, depending on the strength and duration of a wind event. The one-layer

model was effective at examining the barotropic dynamics over the course of the entire experiment. During strong wind events, the wind stress was balanced by the barotropic pressure gradient. This aligns with the classical balance in tidal estuaries between the barotropic pressure gradient and the bottom stress in well-mixed and partially mixed estuaries. When the wind died down, the one-layer balance was predominantly between the barotropic pressure gradient and the acceleration, mirroring the conditions in a stratified lake. The two-layer model was useful for understanding the dynamics of the exchange flow, when there were two distinct layers. The along-channel salinity gradient was not significant in driving the exchange flow during moderate and large wind events. Instead, it seems to be driven by a wind-induced SIPS mechanism.

Conclusions

A field experiment was conducted to investigate the processes driving circulation and salt transport in a wind-driven estuary. Analysis of the depth-averaged momentum equation showed that the primary balance was between the wind stress and barotropic pressure gradient. Applying a band-pass filter to this equation confirmed the presence of a barotropic seiche with a period of about 13 hours, where the barotropic pressure gradient balanced the local acceleration. During periods of strong stratification, there was a two-layer circulation pattern, in which the wind stress was balanced by a combination of the interfacial stress, bottom stresses, and interfacial tilt. Interestingly, the baroclinic pressure gradient term was often insignificant compared with the wind in driving the exchange flow. Up-estuary winds reduced the stratification and reduced or reversed the exchange flow, briefly causing a net transport of salt into the estuary until the water column became vertically mixed. Down-estuary winds enhanced the exchange flow and increased stratification, except when the wind stress was strong enough to overcome stratification and directly mix the water column. Over the course of the entire field experiment,

the asymmetric response to the predominantly down-estuary winds enhanced exchange flow, which when combined with a decrease in freshwater discharge, resulted in a net salt influx.

A new set of parameters were defined in order to compare the physics of a wind driven estuary to classical tidal estuaries. Both Ri_{xw} and M were important in determining the response of the stratification to down-estuary winds, as Ri_{xw} quantified the relative strength of straining and mixing while M quantified the degree to which boundary layer mixing penetrated the water column during a wind event. For up-estuary wind events, straining always enhances mixing, and decreases stratification. Due to a wide range of wind speeds and durations, a wind-driven estuary such as the Neuse experiences varying amounts of mixing, which makes it difficult place in an estuarine classification scheme. Instead, it can fall in a number of different regions of the estuarine parameter space, suggesting that it behaves like a number of different types of estuaries, depending on the wind conditions. Strong winds resulted in well-mixed conditions, while weak winds generally resulted in strongly stratified conditions. Straining by moderate down-estuary winds caused the NRE to behave like a wind-induced SIPS estuary on occasion.
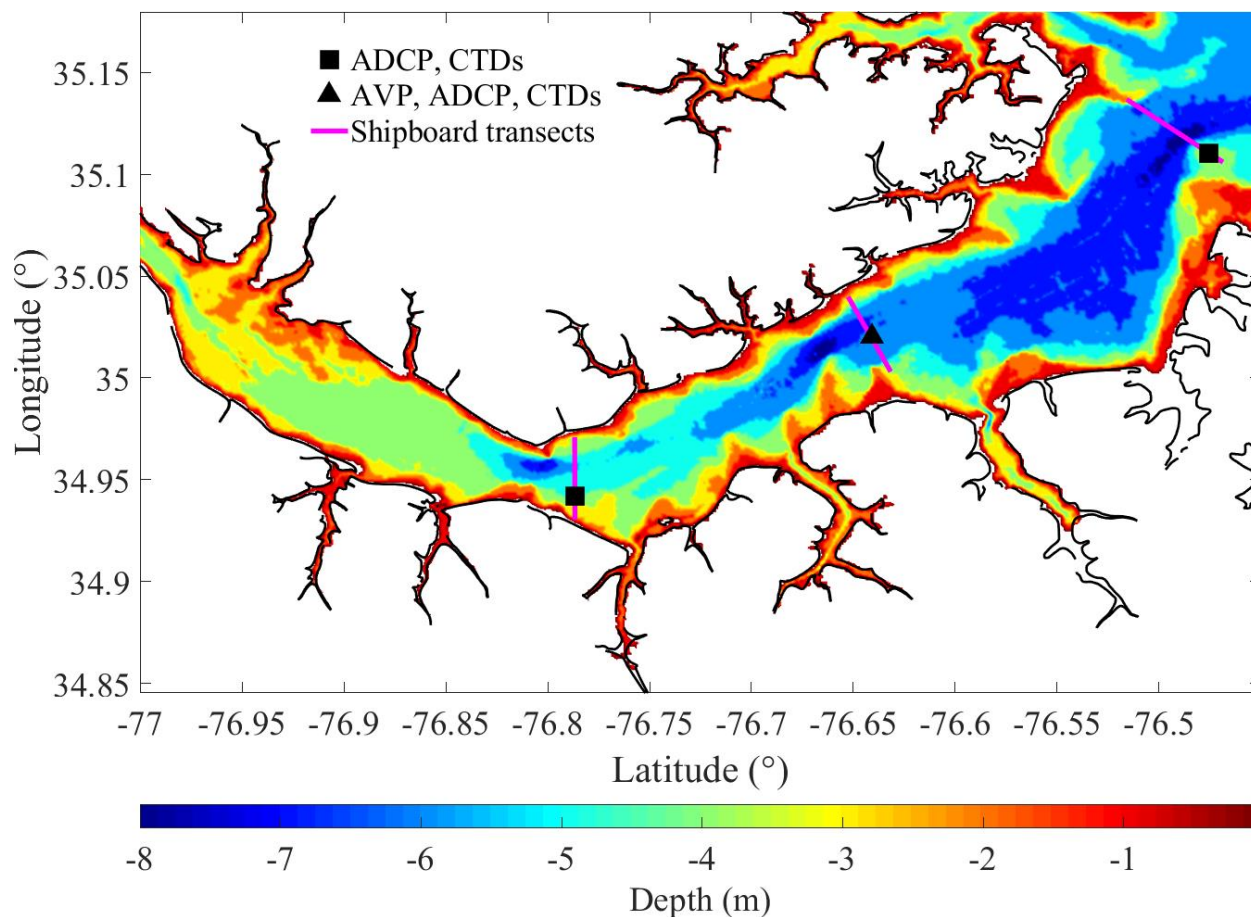
Figure 1.1: Bathymetric map of the Neuse River Estuary with color contours of depth in meters. The two black squares (near bend, mouth of estuary) mark sites with a bottom-mounted ADCP and a mooring of 3 CTDs. At the central site (black triangle), there was also an AVP. Pink lines represent the tracks of biweekly shipboard measurements.
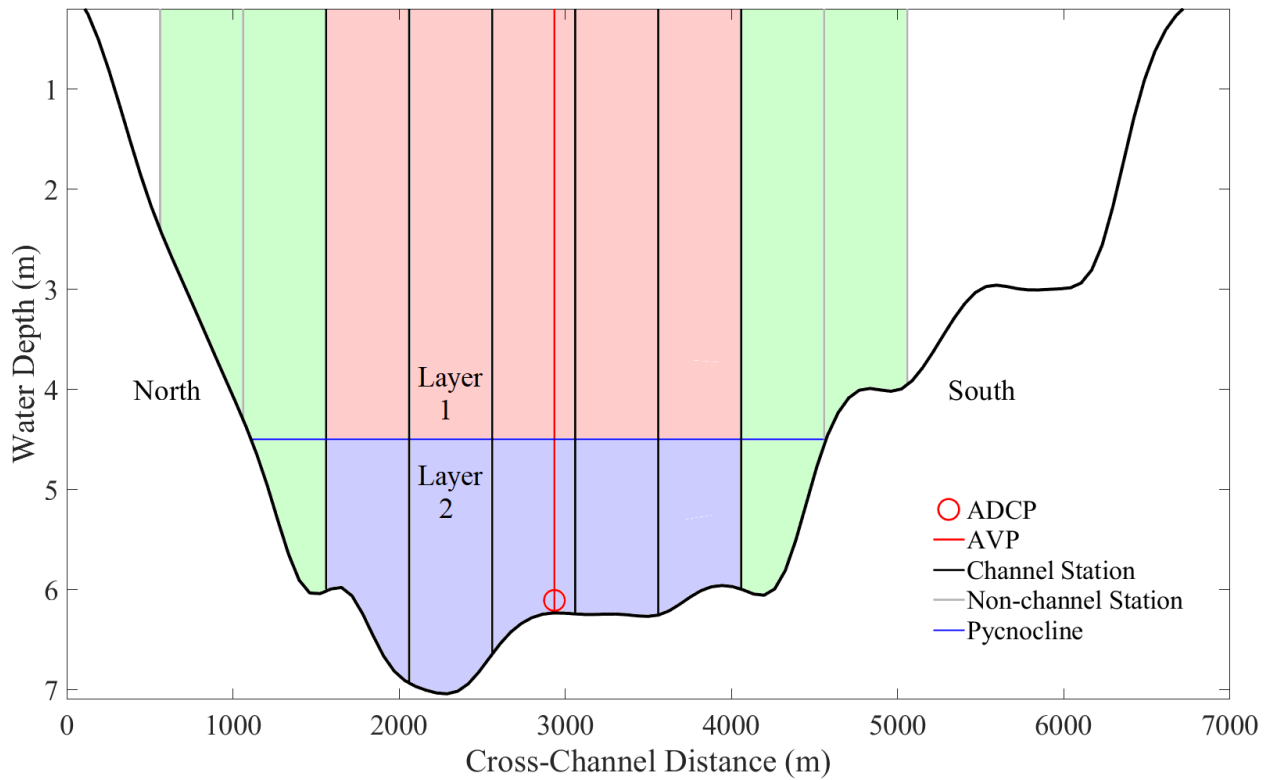
Figure 1.2. Cross- section of the Neuse River Estuary at the location of the central study site. The location of the moored ADCP and AVP are marked in red. Vertical black and gray lines mark the sites of the shipboard ADCP/CTD stations, where biweekly measurements were made from June to September, 2016. The average height of the pycnocline is shown in blue. Shipboard stations marked with black lines are "channel" stations, which always had two layers when the water column was stratified. Gray lines mark "non-channel" stations, where only the top layer was frequently observed during periods of stratification. The shaded red and blue regions represent the two layers used in the two-layer model. The one-layer model includes the red, blue and green regions.
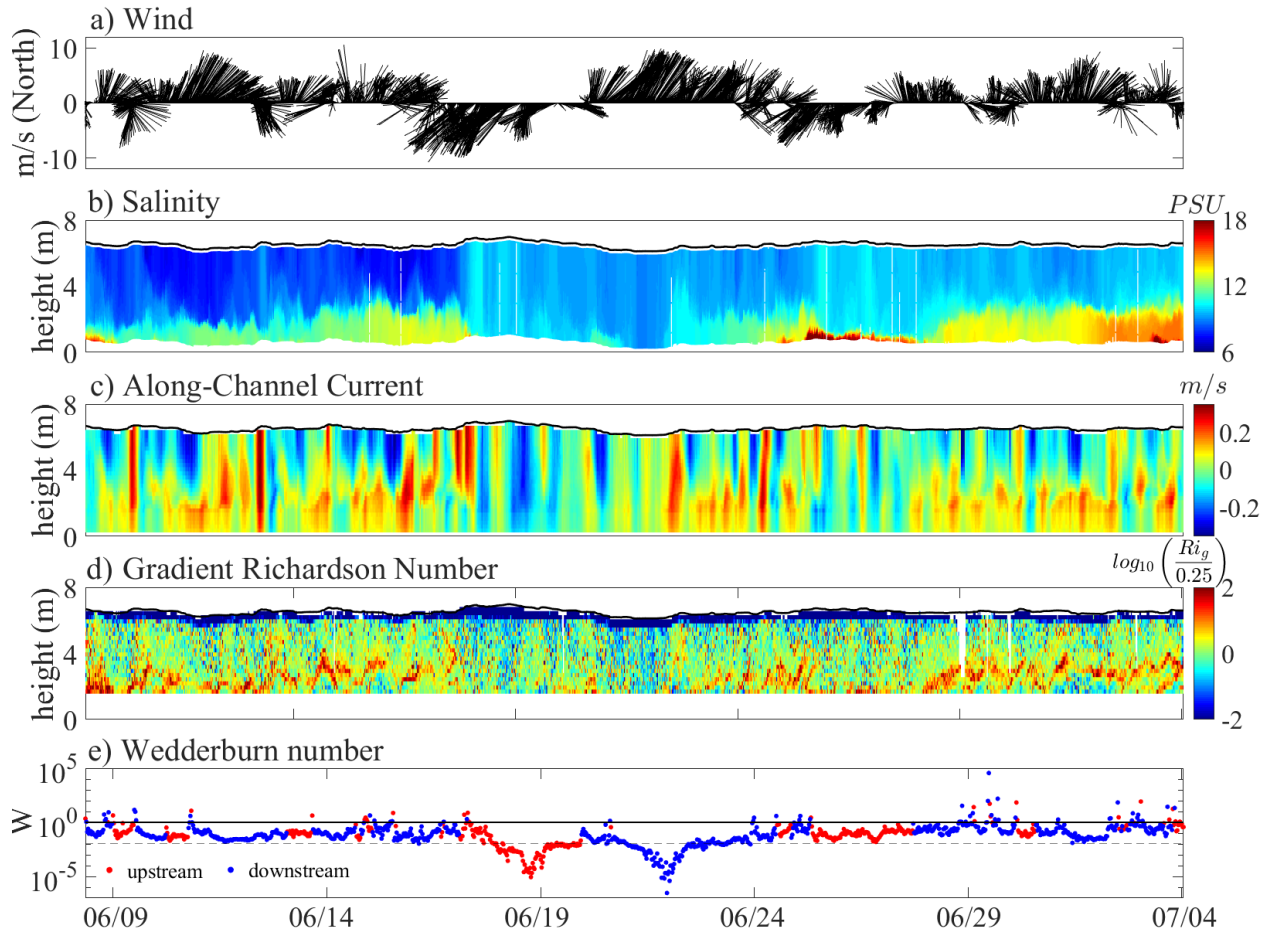
Figure 1.3: Conditions during the 1-month deployment period in June and July 2016. Panels are time series of a) wind speed and direction (sticks indicate direction the wind is blowing toward), b) salinity profiles measured with the AVP, c) along-estuary currents (positive is up-estuary), and d) gradient Richardson numbers normalized by ¼. Ri_g>¼ (warm colors) indicate that stratification is too strong for mixing to occur, and Ri_g<¼ (cool colors) indicate that there is sufficient velocity shear to overcome the stratification and mixing to be possible. Wedderburn numbers are shown in panel e). Values below the gray dashed line are considered strong winds (Chen and Sanford, 2009).
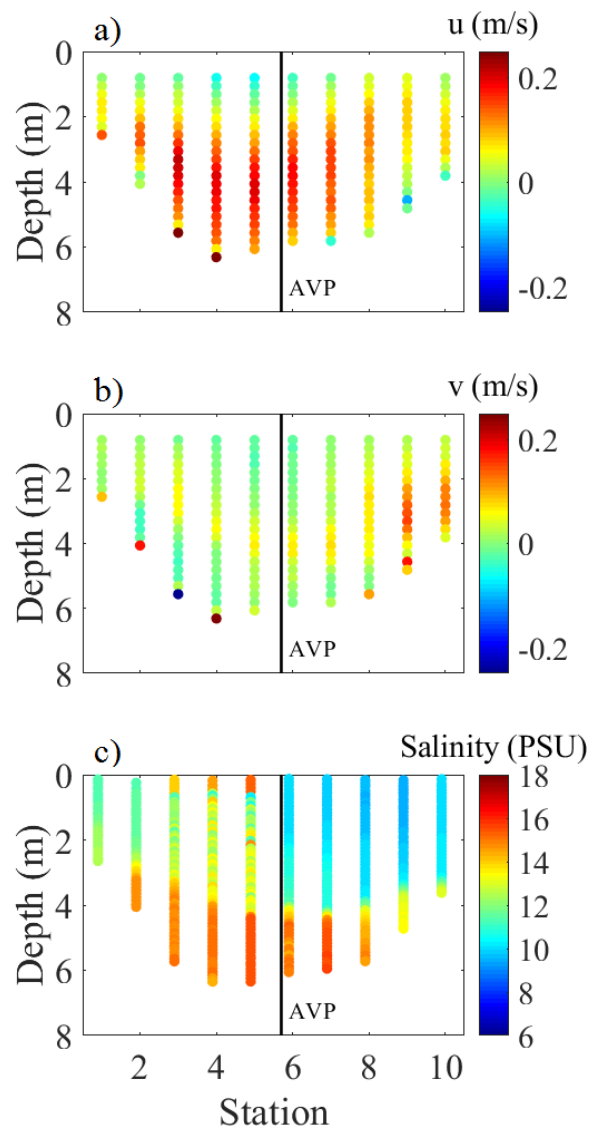
Figure 1.4. Average shipboard ADCP/CTD profiles of (a) along-channel velocity, (b) across-channel velocity, and (c) salinity, collected on the central across the lower Neuse River estuary.
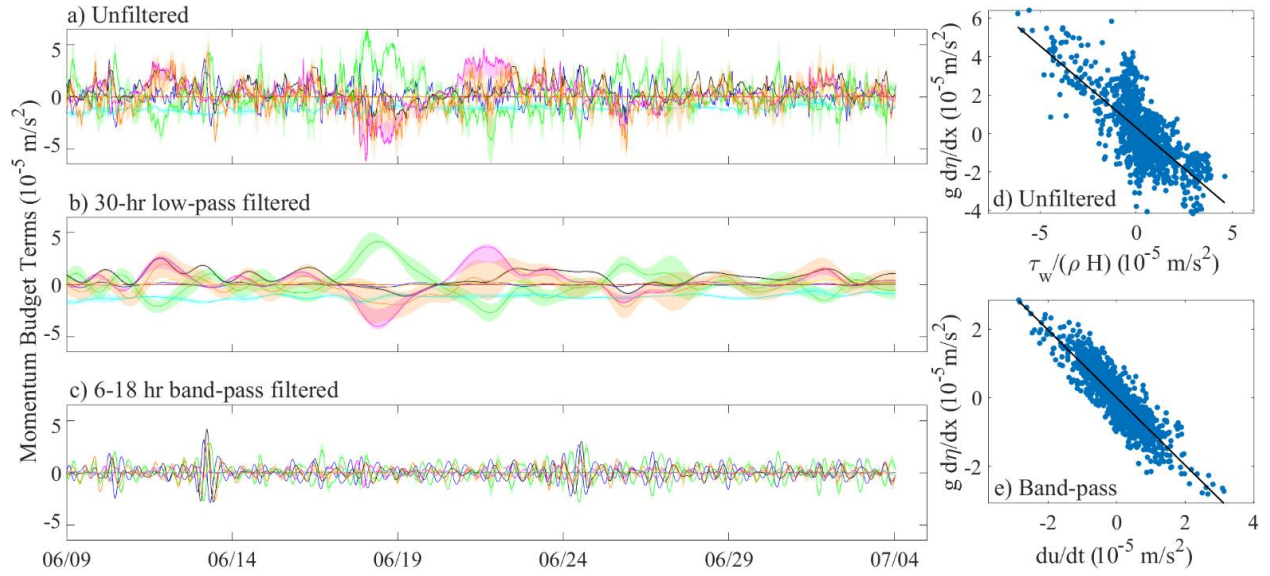
Figure 1.5. Terms of the cross-sectionally averaged momentum budget, computed from the field measurements. Lines represent local acceleration (blue), barotropic pressure gradient force (green), baroclinic pressure gradient force (cyan), wind stress (pink), bottom stress (black), Coriolis (yellow), and residual (orange) terms. Positive force terms correspond to forces directed down-estuary; positive acceleration corresponds to up-estuary acceleration. Time series are a) unfiltered, b) 30 hr low-pass filtered, and c) 6 - 18 hr band-pass filtered momentum budget terms. Scatter plots are d) barotropic pressure gradient term against wind stress and e) band-pass filtered barotropic pressure gradient against acceleration.
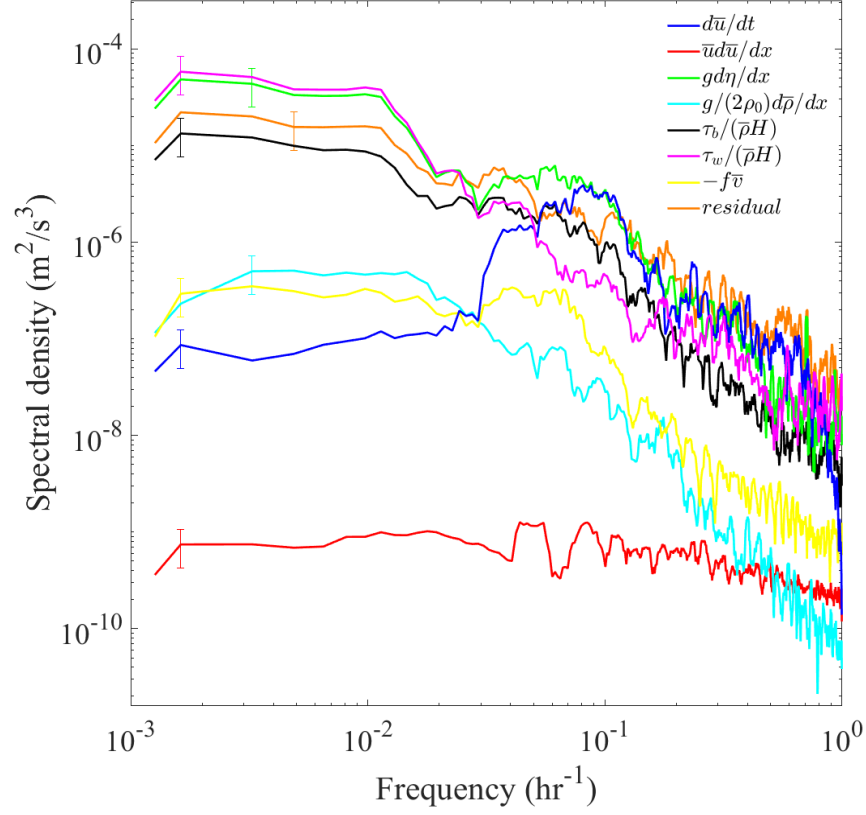
Figure 1.6: Multi-taper spectra of the terms in the cross-sectionally averaged momentum budget. Error bars represent 95% confidence intervals for the spectra.
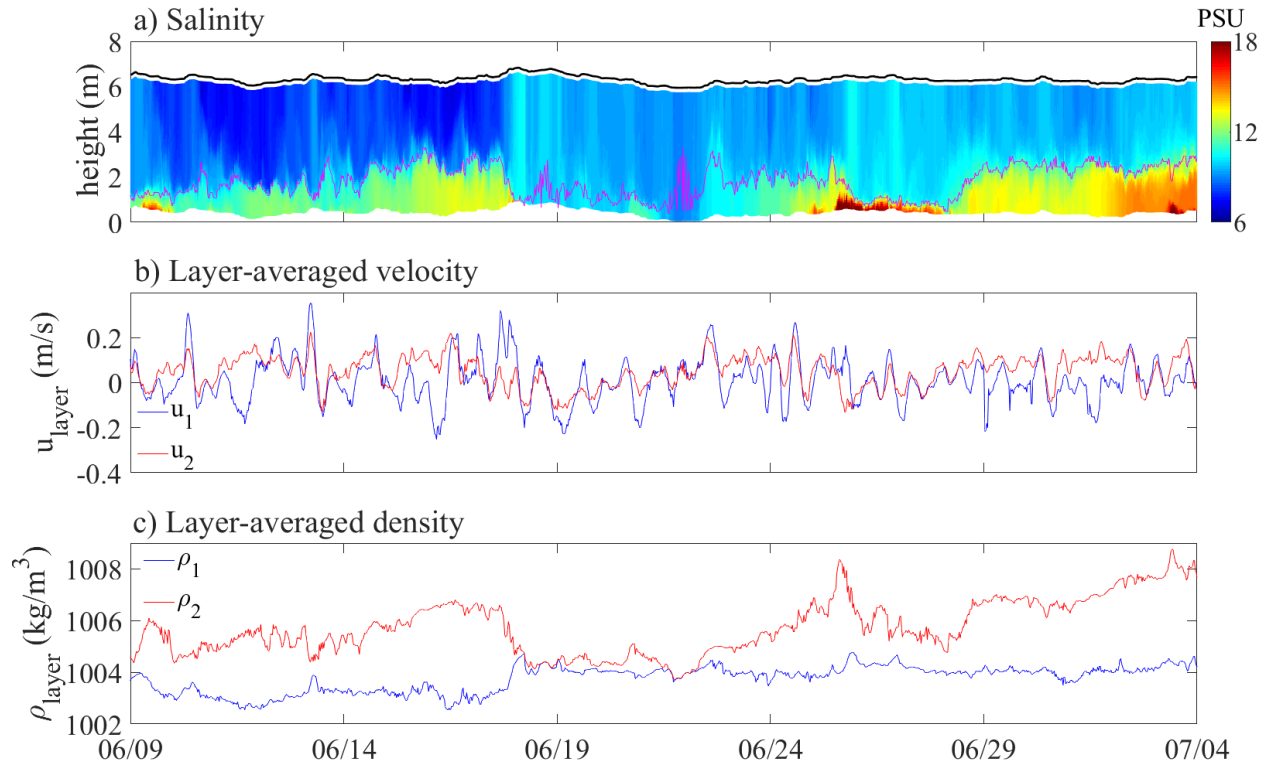
Figure 1.7: a) The water column was divided into two layers using the AVP salinity profiles, with the pink line representing the division between layers. The bottom two panels show layer averaged velocities (b) and densities (c), where the top layer (layer 1) is shown in blue and the bottom layer (layer 2) is shown in red.
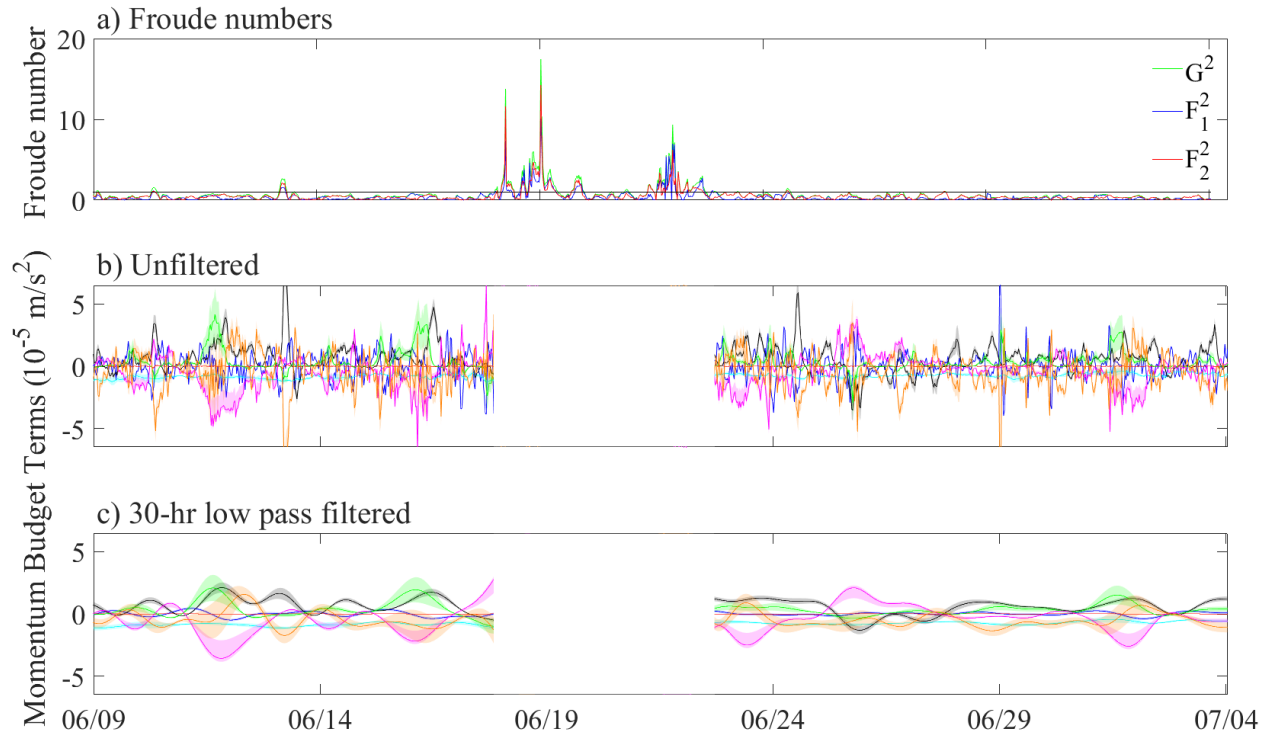
Figure 1.8: a) Time series of internal and layer Froude numbers, where values below the horizontal black line indicate that a two-layer model is applicable. Time series of b) unfiltered, and c) 30 hr low-pass filtered momentum budget terms. Terms of the two-layer momentum balance, computed from the field measurements. Lines represent differential acceleration between two layers (blue), bottom stress (black), wind stress (pink), interfacial stress (green), baroclinic pressure gradient (cyan), advection (red), and residual (orange) terms. The gaps in the time series in b and c were times in which the water column was not strongly stratified by density (see Fig. 1.7c), and therefore the two-layer model is not appropriate.
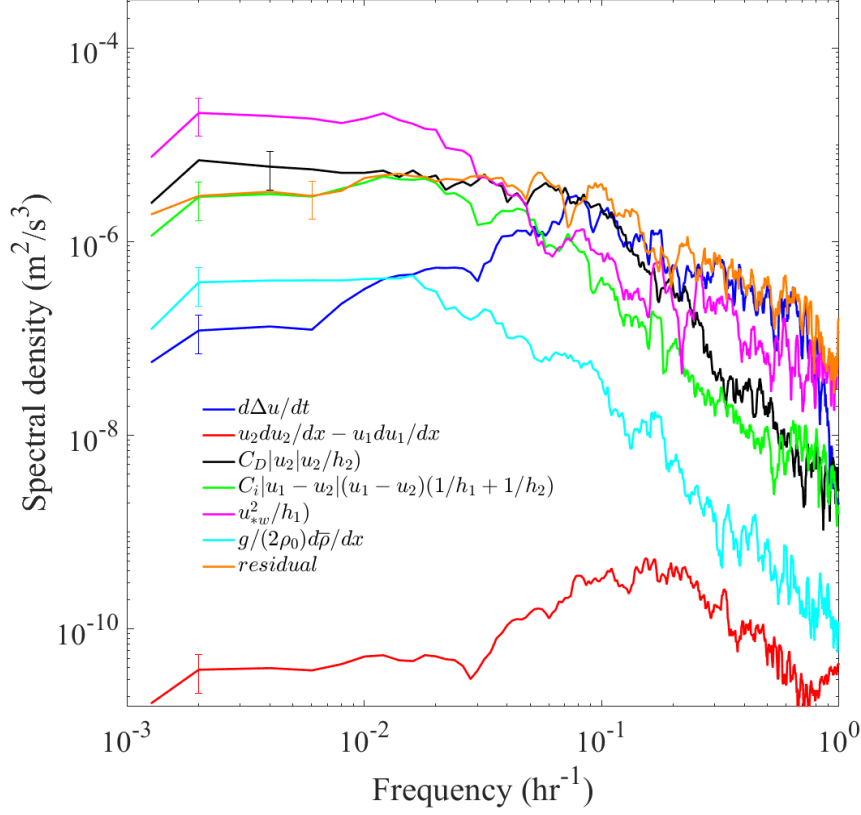
Figure 1.9: Multi-taper spectra of the terms in the two-layer momentum budget. At low frequencies (< 0.013 Hz), the momentum budget is dominated by wind stress (pink), bottom stress (black) and interfacial stress (green) terms. At higher frequencies ($10^{-1.4}$ -$10^{-0.9}$ Hz), the dominant terms are the bottom stress (black) and acceleration in exchange flow (blue).
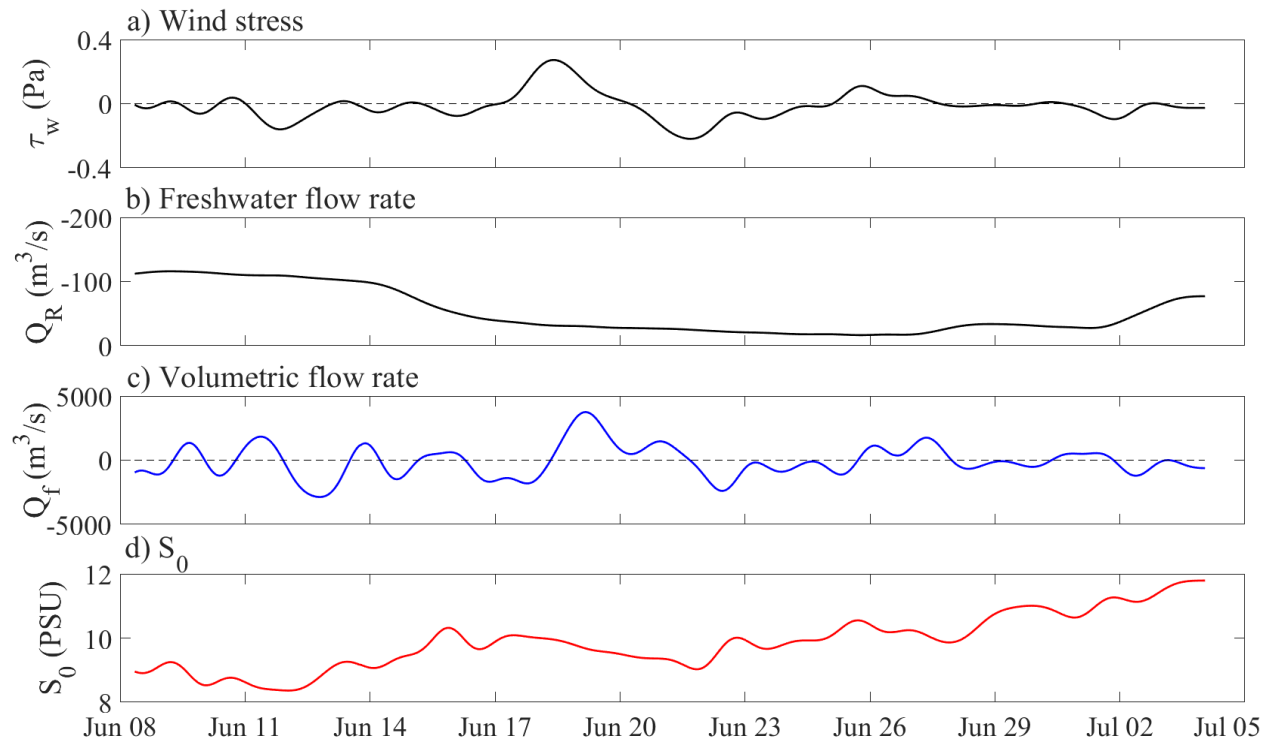
Figure 1.10: Times series of 30-hr filtered wind stress, b) freshwater flow rate, Q_R, c) volumetric flow rate, Q_f, and d) S_0.
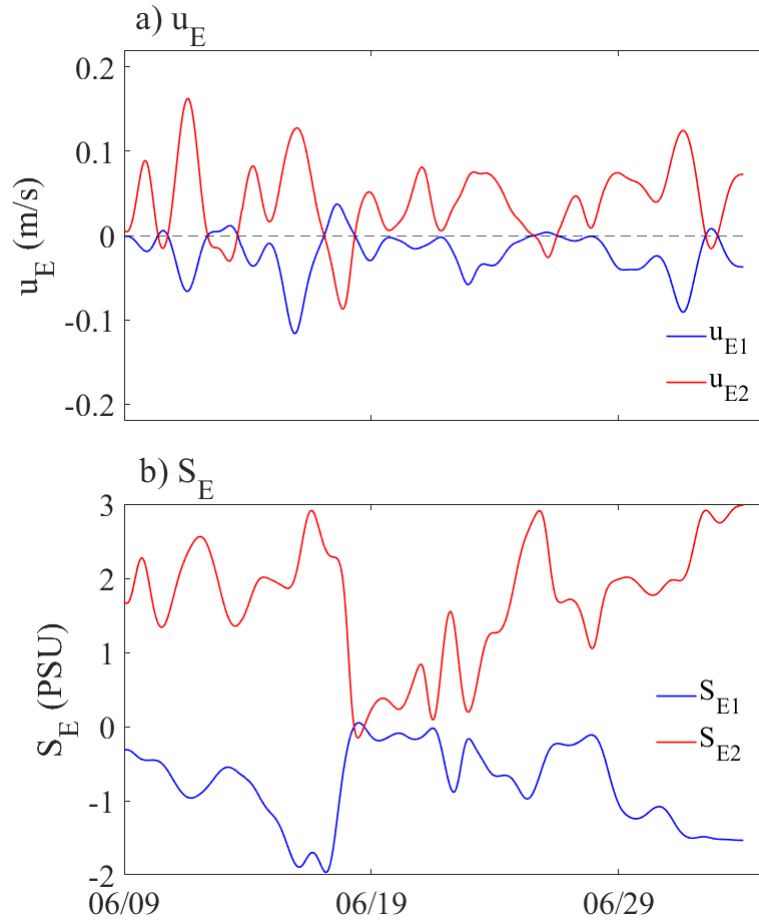
Figure 1.11: Times series of cross-sectional estimates of a) u_E and b) S_E in the top (blue) and bottom (red) layers.
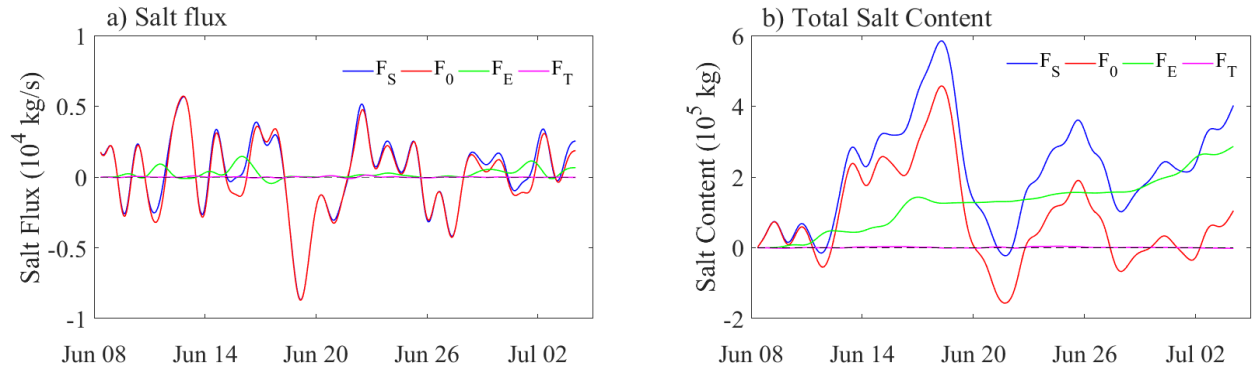
Figure 1.12: Time series of a) salt flux terms and b) total salt content.
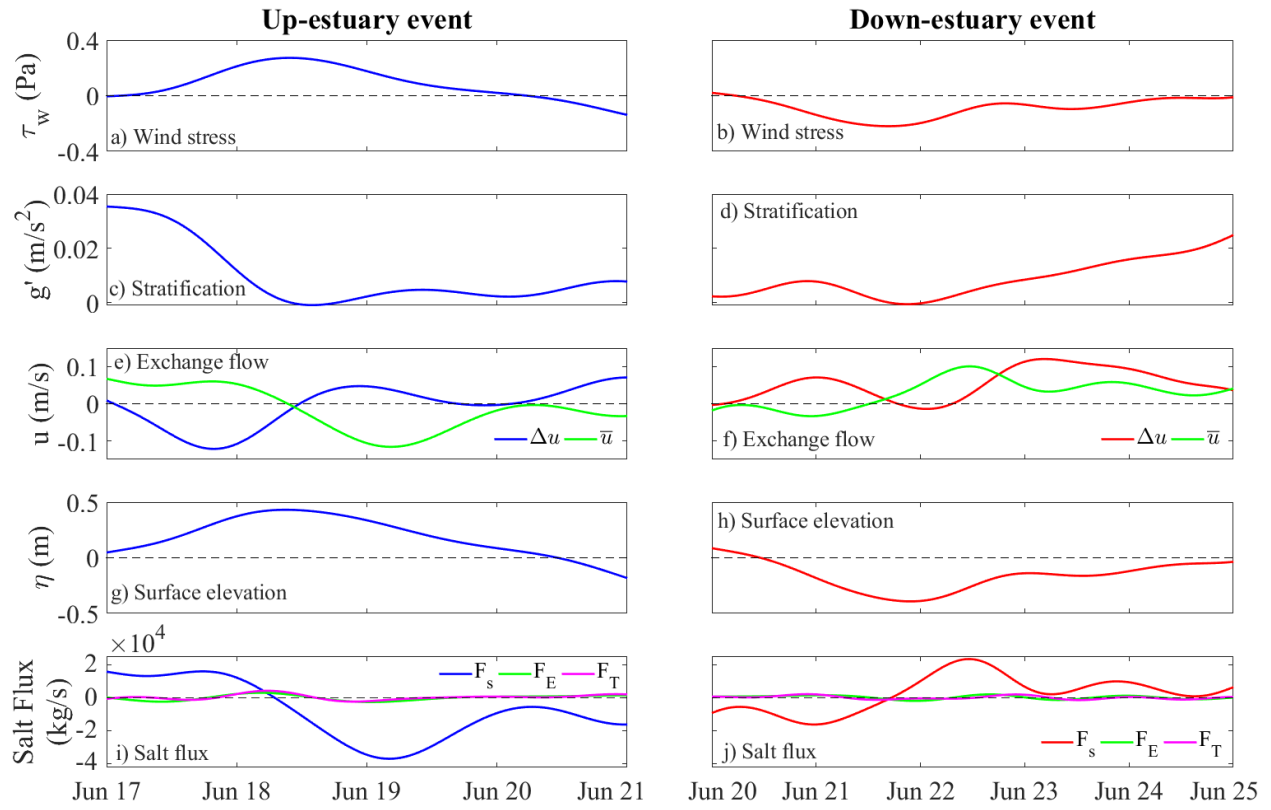
Figure 1.13: Response of the estuary to a typical up-estuary (left) and down-estuary (right) wind event. Rows are: a,b) wind stress (positive upstream), c,d) density difference between upper and lower layers, plotted as *g'*, e,f) difference between the velocities in the upper and lower layers plotted as $\Delta u = u_{lower} - u_{upper}$ (positive upper layer moving downstream with respect to lower layer) and depth-averaged current (positive upstream), g,h) surface elevation at the central site, and i,j) total salt transport (positive upstream).
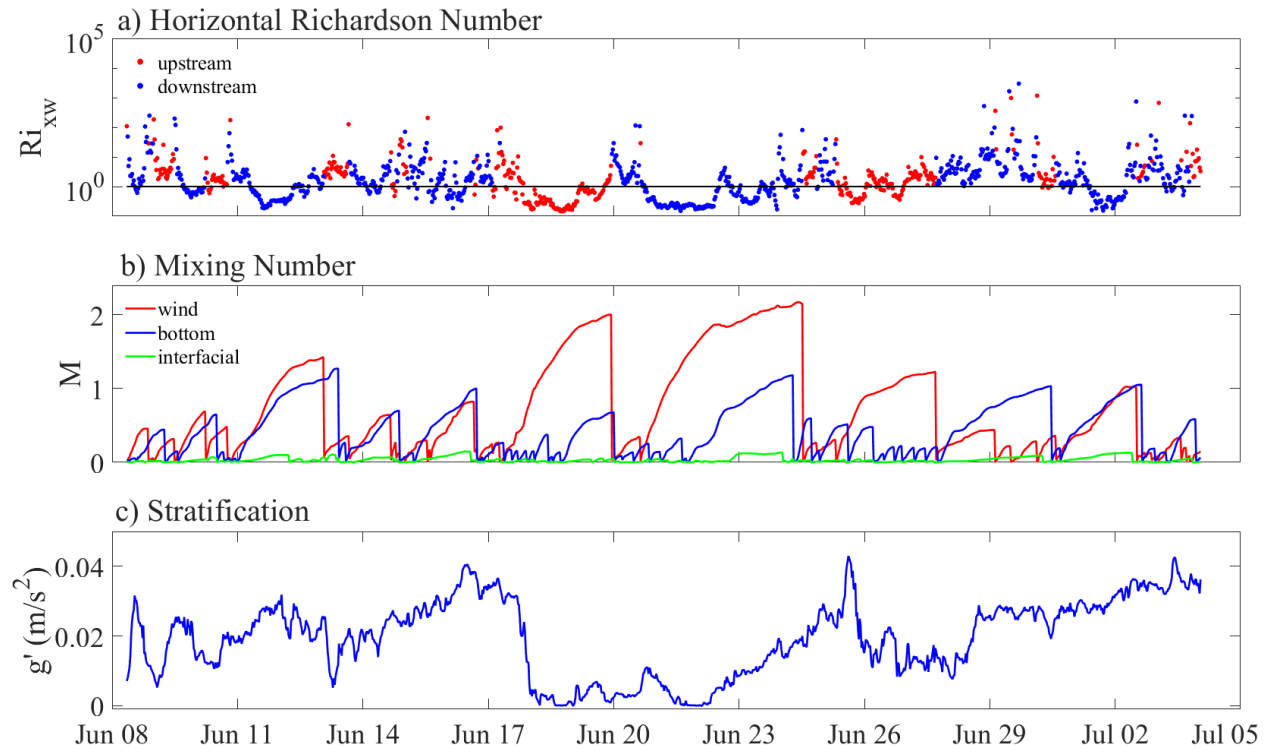
Figure 1.14: Times series of a) horizontal Richardson number, b) g', and c) mixing number.
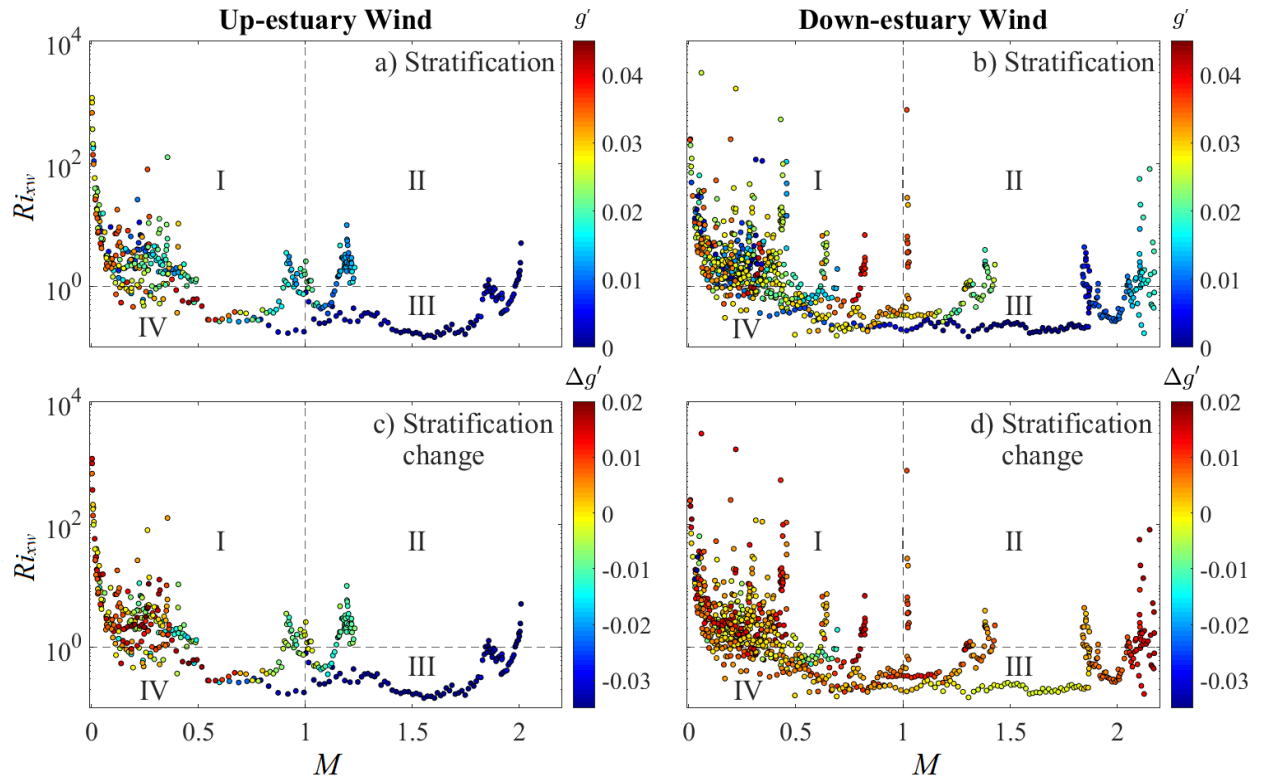
Figure 1.15: Variation of *g'* and *Δg'* in Ri_{xw}-M_{tot} parameter space for (a,c) upstream and (b,d) downstream wind events. In Quadrant I, straining dominates, but occurs over a short period of time. In Quadrant II, straining dominates, and occurs over a long period of time. In Quadrant III, mixing dominates and penetrates the entire water column, while in Quadrant IV mixing dominates, but only penetrates part of the water column.
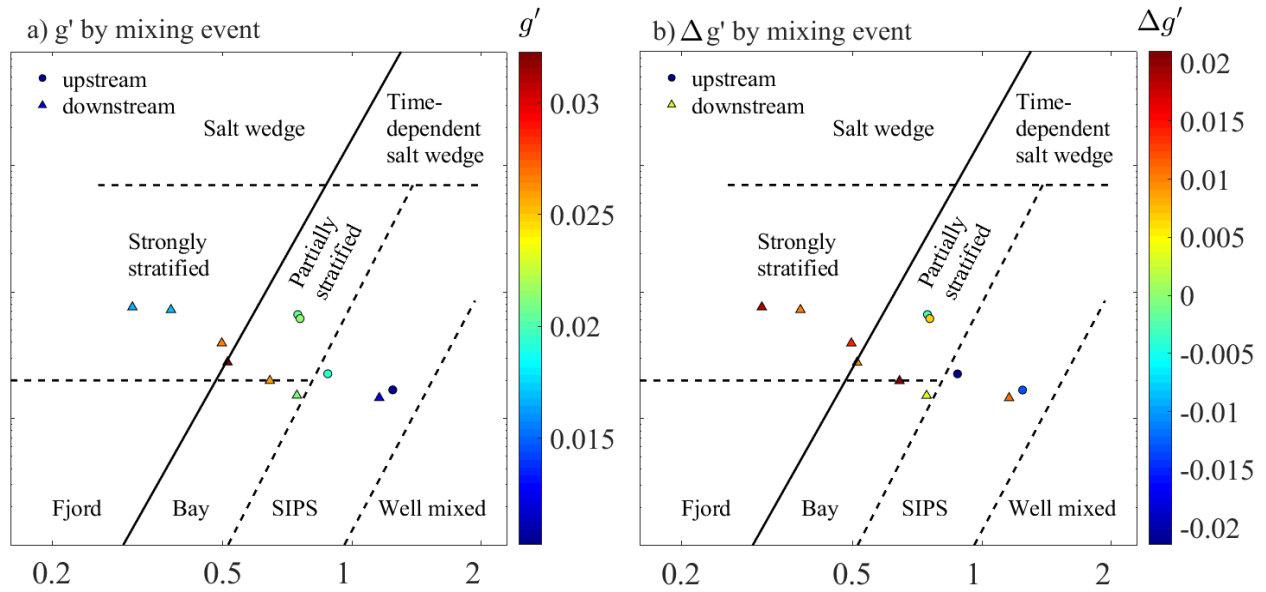
Figure 1.16: Estuarine parameter space based on the freshwater Froude and total mixing number. Black lines divide the parameter space from classification scheme of Geyer and MacCready (2014). Points represent the a) average stratification during each mixing event and b) the change in stratification over the course of the wind event.

REFERENCES

Armi, L., & Farmer, D. M. (1986). Maximal two-layer exchange through a contraction with barotropic net flow. *Journal of Fluid Mechanics*, 164, 27-51.

Bouffard, D., Boegman, L., & Rao, Y. R. (2012). Poincaré wave-induced mixing in a large lake. *Limnology and Oceanography*, *57*(4), 1201.

Blanton, J. O., Amft, J. A., Lee, D. K., & Riordan, A. (1989). Wind stress and heat fluxes observed during winter and spring 1986. *Journal of Geophysical Research: Oceans*, *94*(C8), 10686-10698.

Chen, S. N., & Sanford, L. P. (2009). Axial wind effects on stratification and longitudinal salt transport in an idealzed, partially mixed estuary. *Journal of Physical Oceanography*, *39*(8), 1905-1920.

Devkota, J., & Fang, X. (2015). Quantification of water and salt exchanges in a tidal estuary. *Water*, *7*(5), 1769-1791.

Geyer, W. R., & MacCready, P. (2014). The estuarine circulation. *Annual Review of Fluid Mechanics*, *46*(1), 175–197.

Geyer, W. R., & Ralston, D. K. (2011). 2.03 The dynamics of strongly stratified estuaries. *Treatise on Estuarine and Coastal Science*. Amsterdam: Elsevier, 37-52.

Geyer, W. R., Ralston, D. K., & Holleman, R. C. (2017). Hydraulics and mixing in a laterally divergent channel of a highly stratified estuary. *Journal of Geophysical Research: Oceans,* 122, 4743–4760.

Geyer, W. R., Trowbridge, J. H., & Bowen, M. M. (2000). The dynamics of a partially mixed estuary. *Journal of Physical Oceanography*, *30*(8), 2035-2048.

Hansen, D. V., & Rattray, M. (1965). Gravitational circulation in straits and estuaries. *Journal of Marine Research*, 23, 104–22

Hench, J. L., Bircher, J. T., and Luettich, Jr. R. A. (2000). A portable retractable ADCP boom-mount for small boats. *Estuaries*, *23* (3), 392-399.

Jia, P., & Li, M. (2012). Dynamics of wind-driven circulation in a shallow lagoon with strong horizontal density gradient. *Journal of Geophysical Research: Oceans*, 117(C05013).

Kato, H., & Phillips, O. M. (1969). On the penetration of a turbulent layer into stratified fluid. *Journal of Fluid Mechanics*, *37*(4), 643-655.

Krvavica, N., Travaš, V., & Ožanić, N. (2016). A field study of interfacial friction and entrainment in a microtidal salt-wedge estuary. *Environmental Fluid Mechanics*, *16*(6), 1223-1246.

Luettich, R. A., Carr, S. D., Reynolds-Fleming, J. V., Fulcher, C. W., & McNinch, J. E. (2002). Semi-diurnal seiching in a shallow, micro-tidal lagoonal estuary. *Continental Shelf Research*, *22*(11), 1669-1681.

MacCready, P., & Geyer, W. R. (2010). Advances in estuarine physics. *Annual Review of Marine Science*, *2*, 35-58.

Nidzieko, N. J., Fong, D. A., & Hench, J. L. (2006). Comparison of Reynolds stress estimates derived from standard and fast-ping ADCPs. *Journal of Atmospheric and Oceanic Technology*, *23*(6), 854-861.

Paerl, H. W., Pinckney, J. L., Fear, J. M., & Peierls, B. L. (1998). Ecosystem responses to internal and watershed organic matter loading: consequences for hypoxia in the eutrophying Neuse River Estuary, North Carolina, USA. *Marine Ecology Progress Series*, *166*, 17-25.

Peierls, B. L., Hall, N. S., & Paerl, H. W. (2012). Non-monotonic responses of phytoplankton biomass accumulation to hydrologic variability: a comparison of two coastal plain North Carolina estuaries. *Estuaries and Coasts*, *35*(6), 1376-1392.

Peng, S., & Li, Y. (2015). A parabolic model of drag coefficient for storm surge simulation in the South China Sea. *Scientific Reports*, 5.

Prandle, D. (2003). Relationships between tidal dynamics and bathymetry in strongly convergent estuaries. *Journal of Physical Oceanography*, *33*(12), 2738-2750.

Proudman, J. (1953). *Dynamical Oceanography* (No. 551.46). Methuen.

Reynolds-Fleming, J. V., Fleming, J. G., & Luettich, R. A. (2002). Portable autonomous vertical profiler for estuarine applications. *Estuaries*, *25*(1), 142-147.

Scully, M. E., Friedrichs, C., & Brubaker, J. (2005). Control of estuarine stratification and mixing by wind-induced straining of the estuarine density field. *Estuaries*, *28*(3), 321-326.

Simpson, J. H., Brown, J., Matthews, J., & Allen, G. (1990). Tidal straining, density currents, and stirring in the control of estuarine stratification. *Estuaries*, *13*(2), 125-132.

Spigel, R. H., & Imberger, J. (1980). The classification of mixed-layer dynamics of lakes of small to medium size. *Journal of Physical Oceanography*, *10*(7), 1104-1121.

Stacey, M. T., Burau, J. R., & Monismith, S. G. (2001). Creation of residual flows in a partially stratified estuary. *Journal of Geophysical Research: Oceans*, *106*(17), 013-17.

Taylor, J. (1997). *Introduction to error analysis, the study of uncertainties in physical measurements (2nd ed.)*. University Science Books.

Teledyne RD Instruments. (2006). *Workhorse technical manual. Monitor user guide*.

Trowbridge, J. H. (1992). A simple description of the deepening and structure of a stably stratified flow driven by a surface stress. *Journal of Geophysical Research: Oceans*, *97*(C10), 15529-15543.

Wang, B., Giddings, S. N., Fringer, O. B., Gross, E. S., Fong, D. A., & Monismith, S. G. (2011). Modeling and understanding turbulent mixing in a macrotidal salt wedge estuary. *Journal of Geophysical Research: Oceans*, *116* (C02036).

Whipple, A. C., Luettich Jr, R. A., & Seim, H. E. (2006). Measurements of Reynolds stress in a wind-driven lagoonal estuary. *Ocean Dynamics*, *56*(3-4), 169-185.

Xie, X., & Li, M. (2018). Effects of wind straining on estuarine stratification: A combined observational and modeling study. *Journal of Geophysical Research: Oceans*, *123*(4), 2363-2380.

YSI Incorporated. (2017). *EXO User Manual: Advanced Water Quality Monitoring Platform*.

CHAPTER 2: TURBULENT MIXING IN A STRATIFIED, MICROTIDAL, WIND-DRIVEN ESTUARY

Introduction

Stably stratified shear flows occur in a variety of natural environments, including oceans, lakes, estuaries, and the atmosphere. Turbulent mixing in these environments is crucial to the overall circulation and dynamics of the system. Mixing in the upper ocean affects the stratification, horizontal circulation, overturning, and heat transport toward the poles (Gregg et al., 2018). In estuaries, mixing determines the strength of the exchange flow and stratification, as well as residence times and dispersion of particulate matter (Geyer, 2008). In the atmosphere, mixing is important in determining the distributions of atmospheric chemicals, which has major effects on air quality, absorption of ultraviolet radiation, and climate (Akimoto, 2003).

Stratified turbulence occurs as a result of the competition between background vertical shear, which produces turbulence, and stratification, which suppresses it. This competition is quantified by the gradient Richardson number, $Ri_g = N^2/S^2$ in which $S^2 = (\partial U_1/\partial z)^2 + (\partial U_2/\partial z)^2$ is the local shear squared and $N^2 = -(g/\rho_0)(\partial\rho/\partial z)$ is the squared buoyancy frequency. Here, U_1 and U_2 are orthogonal horizontal velocity components, g is gravitational acceleration, and ρ_0 is the average density. Above a critical value of $Ri_{g\ crit} = 1/4$, linear stability theory predicts that the flow is stable against growth of small amplitude fluctuations (Miles, 1961) and turbulent mixing is restricted (Rohr et al., 1988). Below $Ri_{g\ crit}$ a variety of turbulent instabilities can occur (e.g., Drazin and Reid, 1981), including Kelvin-Helmholtz and Holmboe instabilities. Kelvin-Helmholtz stabilities are considered to be the most common in stratified

environments, and thus have been the focus numerous direct numerical simulations (e.g., Smith and Moum, 2000; Scotti, 2015; Mashayek, et al., 2017).

Due to the relative ease of measuring shear and stratification in the field, it is common to use Ri_g as a proxy for identifying the potential for turbulent mixing in stratified shear flows. In recent studies, the strength of turbulence and turbulent mixing has been estimated more directly with microstructure measurements. In estuarine environments, researchers have made direct measurements of turbulent momentum fluxes (Stacey et al., 1999), dissipation of turbulent kinetic energy (Peters and Bokhorst, 2000), and buoyancy fluxes (Gargett, 1994). Estimates of dissipation turbulent momentum fluxes rely on several important assumptions: the turbulence is 1) fully developed, 2) stationary, and 3) isotropic. However, at high Ri_g direct numerical simulation (DNS) studies have found that all three of these assumptions can break down (Mashayek et al., 2017). The first assumption is typically satisfied by only considering turbulence with sufficiently large Reynolds numbers. The second can be determined with a nonparametric test (Bendat and Piersol, 2000). The third is more problematic, because turbulence is inherently anisotropic at the largest scales due to the influence of background shear and stratification (Mater and Venayagamoorthy, 2014). As such, field studies in estuaries often focus on quantifying isotropic turbulence and are typically limited to energetic environments (e.g., MacDonald and Geyer, 2004; Holleman et al., 2016; Geyer et al., 2017), where there is a large separation between large anisotropic scales and small dissipative scales, and hence a substantial range of scales over which the turbulence is isotropic. In less energetic systems, Bluteau et al. (2011) found that dissipation estimates computed via the standard spectral fitting method can be unreliable for anisotropic turbulence.

It is also difficult to get a complete characterization of turbulence in stratified shear flows using dimensionless parameters, as laboratory experiments have attempted to either parameterize stratified turbulence without shear (e.g., Ivey and Imberger, 1991; Brethouwer et al., 2007) or without stratification (Saddoughi and Veeravalli, 1994). These parameterizations are also dependent on length scales associated with isotropic turbulence, neglecting the larger anisotropic turbulent eddies. More recently, Mater and Venayagamoorthy (2014) proposed a new framework for parameterizing both isotropic and anisotropic turbulence in stably stratified shear flows from dimensional analysis and theoretical considerations. Although they validated it with DNS and laboratory flume data, it has not yet been applied to field measurements.

This study addressed how to directly measure and parameterize stably stratified shear flow turbulence from field measurements collected in a micro-tidal wind-driven estuary. While these estuaries are rarely studied, inconsistent, episodic wind mixing leads to strong stratification, making them ideal environments to study stably stratified shear flows. Thus this study provides an important contribution to understanding mixing processes in these systems and how they compare to tidally dominated estuaries. Methodologically, it increases our understanding of uncertainty in field observations of stratified turbulence and how they translate to interpretation of turbulence quantities. Finally, by applying a recently proposed scaling (Mater and Venayagamoorthy, 2014) our work provides a valuable field application of these dimensionless numbers.

Theoretical Framework

Turbulent Kinetic Energy Equation

The turbulent kinetic energy is defined as

$$\left(k = \frac{1}{2}\left(\overline{u_1'^2} + \overline{u_2'^2} + \overline{u_3'^2} \right) \right) \tag{2.1}$$

and evolves in time according to the following equation

$$\frac{D}{Dt}(k) = T + P - B - \varepsilon$$

$$T = -\frac{\partial}{\partial x_j}\left(\frac{1}{\rho_0}\overline{p'u_j'} + \frac{1}{2}\overline{u_i'u_i'u_j'} - 2\nu\overline{u_i'e_{ij}'} \right) \tag{2.2}$$

$$P = -\overline{u_i'u_j'}\frac{\partial U_i}{\partial x_j}$$

$$B = \frac{g}{\rho}\overline{\rho u_3'}$$

$$\varepsilon = 2\nu\overline{e_{ij}'e_{ij}'}$$

where t is time, x_j are the three-dimensional spatial coordinates, with x_3 positive upward; u_j is

the velocity vector; p is pressure, ν is kinematic viscosity; and $e_{ij} = 1/2[\partial u_i/\partial x_j + \partial u_j/\partial x_i]$.

The velocity, density, and pressure fields have been decomposed into a time-averaged value, a

periodic component, and a turbulent component. That is, $u_i = U_i + \tilde{u}_i + u_i'$, $\rho = \rho_0 + \tilde{\rho} + \rho'$,

$P = P_0 + \tilde{P} + P'$. Overbars represent Reynolds averaging. T is the transport of k due to pressure

fluctuations, turbulent advection, and diffusion by viscosity. This term is often very small, but

may be important when breaking surface waves transfer k downward in the water column (Craig

and Banner, 1994). P is the production of turbulence, as k is transferred from the mean flow via

the interaction between mean shear and Reynolds stresses. This term is typically positive, as

turbulence is "produced" when turbulent eddies are strained by the mean shear. B is the

buoyancy flux, which represents the conversion between turbulent kinetic energy and potential

energy. When the fluid is stably stratified, B will be positive, as turbulent kinetic energy is

expended when denser fluid elements are moved upward in the water column and less dense

fluid elements move downward. Finally, ε is the dissipation of turbulent kinetic energy, or the irreversible loss of k to heat due to viscosity.

In stably stratified estuarine flows, it is often assumed that turbulence is steady and homogeneous, so the turbulent kinetic energy equation would reduce to $P \approx B + \varepsilon$. However, these assumptions of homogeneity and stationarity are often violated in stratified shear flow environments. Stable stratification can cause turbulence to collapse into layered regions, thus violating the assumption of homogeneity (Thorpe, 2016). Turbulence has been shown to be non-stationary for much of the lifecycle of a shear instability, only becoming stationary when it has developed a sufficient range of turbulent length scales (Mashayek et al., 2017).

Turbulent Length Scales

In stably stratified shear flows, turbulence length scales can be derived from fundamental properties of the flow, including N, S, turbulent kinetic energy (k), dissipation (ε), and kinematic viscosity (ν). Dimensional analysis with the parameters N, S, k, ε, and ν yields several commonly used length scales. Length scales characterizing isotropic turbulent eddies are always a function of dissipation, because in the inertial subrange, turbulent kinetic energy cascades from large eddies to small eddies at a rate equal to ε. When the flow is unaffected by either shear or buoyancy, and is hence entirely isotropic, the largest eddies are assumed to have a velocity scale $k^{1/2}$, and are represented by the inertial turbulent length scale, $L_{k\varepsilon} = k^{3/2}/\varepsilon$ (Pope, 2000). When shear and stratification affect the flow, the actual turbulent eddies never reach this size. Instead, when the growth of eddies is limited by buoyancy, the largest isotropic eddies that can occur are the size of the Ozmidov length scale, $L_O = (\varepsilon/N^3)^{1/2}$ (Dougherty 1961; Ozmidov 1965). When shear dominates the largest eddy size, the size of the largest isotropic eddies scales with the Corrsin length scale, $L_C = (\varepsilon/S^3)^{1/2}$ (Corrsin, 1958). These length scales represent the

largest isotropic turbulent eddies, before they are affected by buoyancy or shear. At the high

wavenumber end of the inertial subrange are the smallest eddies where turbulent kinetic energy

is dissipated into heat and characterized by the Kolmogorov length scale ($L_K = (v^3/\varepsilon)^{1/4}$).

Under the influence of stratification or shear, there is a class of anisotropic eddies that are

larger than the biggest isotropic eddies (L_O or L_C). This anisotropic turbulence transfers energy

down-scale at a rate different than ε, as k can be added via shear or lost via buoyancy fluxes

(Mater and Venayagamoorthy, 2014). In these cases, the size of the largest anisotropic eddies is

characterized by either $L_{kN} \equiv (k/N^2)^{1/2}$ or $L_{kS} \equiv (k/S^2)^{1/2}$ (Mater and Venayagamoorthy,

2014), depending on whether the flow is dominated by stratification or shear. The gradient

Richardson number, Ri_g, gives an indication of whether stratification or shear has the dominant

effect on the size of the largest anisotropic turbulent eddies. If $Ri_g>1/4$ (buoyancy dominated),

the largest anisotropic eddies scale with L_{kN}, while if $Ri_g<1/4$ (shear dominated), the largest

anisotropic eddies scale with L_{kS}. Since L_{kN} and L_{kS} do not require an assumption about the

transfer rate of turbulent kinetic energy to smaller scales, they more generally describe the large-

scale motions than do L_O and L_C.

The most objective measure of the size of the largest overturns is the Thorpe scale, $L_T =$

$\langle {\delta_T}^2 \rangle^{1/2}$ (Thorpe, 1977), where, δ_T is the vertical distance a sample must be moved adiabatically

for the profile to become stable. The angle brackets represent vertical ensemble averaging.

Calculation of L_T, requires measurement of instantaneous, high resolution, vertical density

profiles, which are then sorted to give a vertically stable profile. Without density measurements

from a microstructure profiler, the turbulent overturns cannot be resolved to compute L_T. As an

alternative, the overturning length scale can be estimated with the Ellison scale, $L_E = \frac{\langle \rho'^2 \rangle^{1/2}}{\partial \rho / \partial z}$,

which is a statistical measure of the vertical displacement of a fluid parcel, before returning to an

equilibrium position or being irreversibly mixed with the surrounding fluid (Ellison, 1957). It has

been shown that L_E and L_T agree well with each other, except under strongly stratified

conditions, in which $Ri_g > 1$ (Itsweire et al., 1993). When the flow is strongly stratified, internal

gravity waves cause L_E to be larger than L_T, as a result of the averaging schemes used in their

calculations. Specifically, computation of ρ'^2 requires not only vertical averaging, but also time

averaging, which translates to lateral ensemble averaging via the frozen turbulence hypothesis. In

the presence of internal waves, lateral ensemble averaging increases the value of ρ'^2, and thus

L_E. On the other hand, L_T is only vertically ensemble averaged, rendering it immune to this issue

(Mater et al., 2013). As a result, when stratification is strong, L_E has a tendency to overestimate

the size of the turbulent overturns.

Dimensionless numbers

To better understand the nature of the observed turbulence, several dimensionless

parameters can be calculated from ratios of various turbulent length scales. Traditionally,

stratified turbulence is characterized in a Re_t–Fr_t parameter space (e.g., Ivey and Imberger,

1991). Here, $Re_t = (L_E/L_K)^{4/3}$ is the turbulent Reynolds number and represents the range of

energy containing scales. $Fr_t = (L_O/L_E)^{2/3}$ is the turbulent Froude number and relates how big

the isotropic turbulent eddies are to how big they could be. Alternatively, Fr_t is the ratio of

inertial to buoyancy forcing among the energy-bearing turbulent eddies. This framework,

however, has a couple of drawbacks. First, it only accounts for the effects of buoyancy, and not

shear. Second, it relies on the Ozmidov length scale, which assumes the turbulence is isotropic

and ignores largest anisotropic eddies inherent in stably stratified shear flows.

A more appropriate framework when both shear and stratification are significant is the

$NT_L - ST_L$ framework developed by Mater and Venayagamoorthy (2014). Here, NT_L and ST_L

are the buoyancy and shear parameters respectively, where $T_L \equiv k/\varepsilon$ is the inertial time scale of the turbulence and N^{-1} and S^{-1} are the time scales associated with buoyancy and shear. Thus, NT_L and ST_L are the ratios of the inertial time scale to the buoyancy and shear time scales. A large value of NT_L (or ST_L) indicates that the timescale for turnover of the largest eddies is long compared with the time-scale for buoyancy (or shear) to affect eddies. Therefore, the turbulence is affected by buoyancy (or shear). Conversely, a small value of NT_L (ST_L) indicates that time-scales of eddies are sufficiently short that they are not affected by buoyancy (shear). This framework is superior to the Re_t–Fr_t parameter space for stratified shear flows, because it accounts for both stratification and shear, and relies on length scales that are generalized to include both isotropic and anisotropic turbulence.

Another commonly used dimensionless parameter is the activity number or Gibson number: $Re_b = (L_O/L_K)^{4/3}$, which represents the range of length scales in the inertial subrange in buoyancy-controlled, stratified flows (Gibson, 1986; Ivey and Imberger, 1991; Stacey et al., 1999). Equivalently, Re_b is a measurement of the relative magnitude of dissipation to the combined damping effects of viscosity and buoyancy: $Re_b = \varepsilon/(\nu N^2)$. It is often referred to as a buoyancy Reynolds number, because it is a ratio of inertial to viscous effects (Smyth and Moum, 2000). It has also been considered to be a small-scale Froude number, because it compares an inertial scale to a buoyancy scale (Luketina and Imberger, 1989; Ivey and Imberger, 1991). Re_b is typically used to quantify the intensity of turbulence is stratified systems. Turbulence has been found to be affected by buoyancy and viscosity for $Re_b < 100$, and greatly suppressed when $Re_b < 15$ (Ivey and Imberger, 1991; Saggio and Imberger, 2001).

While widely used, Re_b makes it difficult to distinguish whether the stabilizing effects are due to viscosity or buoyancy. Large values of Re_b can occur as a result of strong turbulence or

weak stratification. Furthermore, it only represents the full range of turbulent motion when the flow is fully isotropic (Mater et al., 2013). Dissipation rates have also been found to strongly vary with time during a single mixing event, making it difficult to associate a certain value of Re_b with a particular mixing event (Mashayek et al., 2017).

Mixing efficiency

The efficiency of vertical mixing can be quantified by the flux Richardson number, $Ri_f = \frac{B}{P}$. However, this definition only applies to homogenous and stationary turbulence. Traditionally, it is assumed that $Ri_f = 0.17$, which is the value proposed by Osborn (1980) based on theoretical predictions of Ellison (1957). However, numerous lab experiments (e.g; Strang and Fernando, 2001; Rehmann and Koseff, 2004), direct numerical simulations (e.g., Smyth et al., 2001; Shih et al., 2005; Mashayek et al., 2017), and field studies (e.g., Davis and Monismith, 2011; Dunckley et al., 2012; Walter et al., 2014; Holleman et al., 2016) have shown that Ri_f can vary, depending on external conditions.

In stably stratified shear flows, a more appropriate definition, which does not require the turbulence to be stationary or homogeneous is:

$$R_f = \frac{B}{m} = \frac{1}{1 + \left(\frac{\varepsilon}{B}\right)} \tag{2.3}$$

where *m* is the net mechanical energy available to sustain turbulent motion and includes not only *P*, but also *T* (Ivey and Imberger, 1991). In stationary, homogeneous shear flows $Ri_f = R_f$. While removing the requirement that the turbulence be homogeneous and stationary, this definition includes reversible fluxes, such as those generated by internal waves, and are common in strongly stratified environments. A more rigorous version of the flux Richardson number, which only accounts for the irreversible conversions of energy locally, is defined as:

$$R_f^* = \frac{\varepsilon_{PE}}{\varepsilon + \varepsilon_{PE}} \tag{2.4}$$

where $\varepsilon_{PE} = N^2 \varepsilon_\rho (d\rho/dz)^{-2}$, in which $\varepsilon_\rho = \kappa \overline{(\nabla \rho')^2}$ is the dissipation rate of density variance

and κ is the molecular diffusivity of density (Peltier and Caufield, 2003; Venayagamoorthy and

Stretch, 2010). Without the benefit of DNS, this study relies on the Ivey and Imberger (1991)

definition of R_f (Eq. 2.3). When turbulence is intense, all three definitions are roughly the same,

but as Ri_g increases past the critical value, the first two definitions tend to diverge from R_f^*.

Specifically, R_f typically underestimates the true value of the flux Richardson number due to the

prevalence of reversible fluxes in strongly stratified flows (Venayagamoorthy and Koseff, 2016).

Methods

Field Measurements

      Field measurements were conducted in the Neuse River Estuary (NRE), a microtidal,

wind-driven estuary in eastern North Carolina. Connecting to Pamlico Sound, the NRE is nearly

isolated from the Atlantic Ocean by the Outer Banks barrier islands, which allow for limited tidal

exchange through three small inlets. As such, NRE astronomical tides are negligible, accounting

for approximately 1% of the variation in water level and velocity (Luettich et al., 2002). The

NRE is shallow (mean depth of ~3.5 m) and narrow (mean width of 6.5 km) with a large fetch

(length of ~70 km), which allows for the wind to be the main driver of flow patterns and

turbulent mixing throughout the water column. During the summer, the wind direction is

typically NE-SW, which is along-channel in the lower Neuse, but across-channel in the upper

Neuse. As a result, the NRE experiences episodic periods of strong salinity stratification, leading

to bottom water hypoxia due to eutrophication and lack of mixing (Paerl et al, 1998).

The upper Neuse (Fig. 2.1) was chosen as the study site due to the prevalence of strong stratification, making it an ideal location to examine stably stratified shear flows. Measurements of turbulent fluctuations were made during a 10-day period in August 2013 using an array of three 6-MHz acoustic Doppler velocimeters (ADVs; Nortek AS Vector) with synchronized, co-located fast conductivity and temperature (CT) sensors (PME, Inc.) mounted on a sawhorse frame (Fig. 2.2). Each ADV/CT pair synchronously sampled at 16 Hz. Each ADV sample volume was 0.013 m, and the CT sensor sample volume is 3-5 cm. The three ADVs were located at 1.3, 1.9, and 2.5 m above bottom, in 4 m of water, in order to observe mixing across the pycnocline. A pair of high-resolution pulse-coherent current profilers (Nortek Aquadopp HR) mounted upward and downward-looking on the sawhorse frame provided measurements of velocity in 3-cm bins, while sampling at 1 Hz and recording an average of pings every 5 seconds. A bottom-mounted ADCP (TRDI 1.2 MHz Workhorse) sampled every 1 second in mode 12 with 4 subpings per profile. Velocities were recorded in beam coordinates for the entire water column (4 m) in 0.25 m vertical bins, the first of which was centered 0.87 m above bottom.

An Autonomous Vertical Profiler (AVP) measured profiles of temperature and salinity, at 30-min intervals. These data were binned at 10-cm resolution. The AVP is a floating platform that lowers a CTD (YSI EXO Sonde) at a constant rate from the surface to the bottom (Reynolds-Fleming et al., 2002, Whipple et al. 2006). The temperature and salinity measurements were verified by a vertical array of 4 CTDs (SeaBird SBE-37SMP-ODO MicroCATs at 0.5, 1.0, 1.6, and 2.2 mab), 4 thermistors (SBE 56 at 0.5, 1.25, 2.0, and 2.8 mab), and 2 pressure sensors (RBR-DR1050 at 0.5 and 2.8 mab). Together with the velocity measurements from the ADCP, densities computed from the AVP salinity and temperature profiles were used to compute gradient Richardson numbers. Wind measurements were collected

during each vertical profile using the AVP's anemometer, located at a height of 5 m and sampled every 30 minutes.

Due to mechanical issues, the AVP did not collect data for a two-day period from 8/13 to 8/15. During this time, measurements from the CTD array were used in place of measurements from AVP CTD, and wind measurements were obtained from the Marine Corps Air Station at Cherry Point (Fig. 2.1).

Data Processing

Stratification and turbulence parameters were calculated using the following methods. The gradient Richardson numbers were calculated from velocity profiles collected by the ADCP and density profiles obtained from the YSI Sonde on the AVP. During the period when the AVP was not functioning, density profiles were instead calculated from the vertical CTD arrays. The ADCP data was averaged over 30 minutes to align with the density data, which was collected every 30 minutes by the Sonde on the AVP. Although the AVP density profiles have a resolution of 10 cm, the ADCP measurements were made with 0.25-m bins. However, the true resolution of these ADCP measurements is slightly coarser than 0.25-m, since the ADCP averages velocities over 3 adjacent bins using a Barlett filter during internal processing (MacKinnon and Gregg, 2005). Density data were therefore interpolated to align with the ADCP data. When the only density data available was from the CTD array, the ADCP data were spatially averaged and interpolated to align with the CTD measurements, which were 50-60 cm apart. Higher resolution gradient Richardson numbers were also computed using velocity data from the HR-ADPs instead of the ADCP. The HR-ADP velocity data only covered the middle of the water column and the resulting values of Ri_g differed from those calculated from the lower resolution ADCP measurements by an average of 20%. However, the values of Ri_g were often very large, so this

difference did not affect the conclusions about the stability of the flow. As a result, the Ri_g values presented in this study are those computed from the ADCP velocity data.

Velocity data from the ADVs were despiked using a kernel density-based algorithm (Islam and Zhu, 2013). Turbulence statistics were computed from 10-min segments of the ADV/CTs records. The presence of internal waves can result in the sensors sampling areas from parts of the water column with very different properties; for example, both above and below the pycnocline, during the same 10-min period. Therefore, the only times considered in the ADV/CT records were those in which the sensors remained in the same water mass throughout the 10-min period. To identify periods when the region of the water column sampled by the ADV was sufficiently stationary over a 10-min interval, we defined a nondimensional number, $J = \frac{H\frac{d\bar{s}}{dz}}{\sigma_s}$, where H is the water depth, σ_s is the standard deviation of salinity measured by the CT sensor over the 10-min interval, and $d\bar{s}/dz$ is the background vertical salinity gradient measured by the CTD on the AVP. J can be thought of as the ratio of the salinity difference between the top and bottom of the water column to the small-scale fluctuations in salinity at the CT sensor location due to a combination of internal waves and turbulence. Only 10-min intervals with $J > 100$, corresponding to salinity fluctuations less than 1% of the salinity difference between the top and bottom of the water column, were considered in the calculation of turbulence statistics. Removal of time intervals affected by internal waves also helps ensure that L_E is a reasonable estimate of the overturning scale.

The velocities for each 10-min ADV record were divided into segments of 1024 points, with 50% overlap. A Hann window was applied to each segment, and the power spectrum was calculated. Averaging over all of the segments resulted in a spectral estimate for each 10-min record with 95 degrees of freedom (Emery and Thomson, 2001).

Calculation of turbulence statistics

The turbulent dissipation rate was calculated for each 10-min interval by fitting a model for the inertial subrange of turbulence to the observed vertical velocity spectra. The model assumes that the inertial subrange of the observed turbulence follows a Kolmogorov -5/3 law (Pope, 2000). The model relies on Taylor's frozen turbulence approximation, which assumes turbulent eddies do not change significantly during the time taken to advect past the sensor. The model allows for the frozen inertial sub-range turbulence to be advected past the sensor by a steady horizontal current and random waves (Lumley and Terray, 1983; Rosman and Gerbi, 2017). The equation for the inertial sub-range portion of the power spectrum, in frequency space, is (Trowbridge and Elgar 2001):

$$P_{ww}(\omega) = \frac{24}{55}\alpha\varepsilon^{2/3}V^{2/3}\omega^{-5/3}I\left(\frac{\sigma}{V},\theta\right) \tag{2.5}$$

where P_{ww} is the vertical velocity spectrum, ω is the radian frequency, α is the empirical Kolmogorov constant, approximately equal to 1.5 (reviewed by Sreenivasan, 1995), V is the magnitude of the current, σ^2 is the variance of the wave-induced horizontal velocity; θ is the angle between the waves and current; and $I(\sigma/V,\theta)$ is a wave adjustment factor (Trowbridge and Elgar, 2001).

In applying the above model, a line with a -5/3 slope was fit to the inertial subrange of spectra on log-log axes for frequencies greater than that of the wave peak (Fig. 2.3). The frequencies of the inertial subrange were determined by first fitting a line of -5/3 to a range of frequencies always within the inertial subrange (1.5 - 3.75 Hz). Any spectra in which the -5/3 fit had an R2 of less than 0.7 was rejected, as turbulence estimates could not be estimated. For those spectra that were not rejected, the frequency range was then iteratively toward the wave peak (lower frequencies) and toward the noise floor (higher frequencies) and the -5/3 line was fit to

the new frequency range. Analysis of the vertical velocity spectra indicated that when the fit

reached the wave peak, the R^2 value of the -5/3 decreased by more than 0.001. Therefore, the

frequency range was only extended iteratively until the R^2 value decreased by more than 0.001.

Spectral estimates followed a chi-squared distribution, which for a Hann window have

$(8/3)(N/M) = 95$ degrees of freedom, where N is the number of data points and M is the half-

width length (Emery and Thomson, 2001). Confidence intervals for the spectra were calculated

and a -5/3 fit was applied to the upper and lower bounds to get a 95% confidence interval on the

dissipation. However, Bluteau et al. (2011) found that dissipation estimates are less reliable when

the turbulence becomes anisotropic, so the uncertainty is likely higher than computed

statistically. For $Re_b < 500$, they observed that ε could differ from the true value by two-orders of

magnitude. As a result, estimates of Re_b are presented in all turbulence classification schemes.

Computation of Reynolds stresses also required a wave-turbulence decomposition

method, as small errors in ADV orientation result in correlations between orthogonal wave

orbital velocity components that bias Reynolds stress estimates. A pressure correlation method

was used for wave-turbulence decomposition, in which it was assumed that motions correlated

with the displacement of the free surface were waves and did not correlate with turbulence. The

turbulence cospectrum, $Pu_1'u_3'$, was computed by subtracting the cospectrum of wave orbital

velocities from the cospectrum of raw velocities (Benilov and Filyushkin, 1970). Reynolds

stresses were then calculated by integrating over $Pu_1'u_3'$ (Bendat and Piersol, 2000). A typical

turbulence cospectrum is shown in Fig. 2.4a. The pressure correlation method successfully

removes the wave bias, leaving no significant remaining peak in the turbulence cospectrum (Fig.

2.4a) and variance-preserving cospectrum (Fig. 2.4b). Calculations of shear production used 10-

min averages of horizontal velocity from the Aquadopp HRs (3-cm resolution), which provided

70

measurements within 1 cm of the height of the ADVs. Likewise, the buoyancy fluxes were calculated from the cospectra, $P\rho'u_3'$, using the pressure correlation wave bias decomposition method described above.

To compute 95% confidence intervals for Reynolds stresses, confidence intervals were first computed for each cospectrum, $Pu_1'u_3'$, after applying the pressure correlation method by assuming it followed a chi-squared distribution with 90 degrees of freedom (Emery and Thompson, 2001). Reynolds stresses were then computed from the upper and lower bounds of $Pu_1'u_3'$, to get 95% confidence intervals on the estimated Reynolds stresses. The same procedure was applied to each $P\rho'u_3'$ to get confidence intervals for the buoyancy fluxes.

Ideally, k would be computed from the u_i' according to equation 2.1. However, processes other than turbulence and surface waves cause fluctuations in horizontal velocities and thus accurate estimates of $\overline{u_1'^2}$ and $\overline{u_2'^2}$, could not be obtained from ADV data. Instead, k was computed using a method adapted from Mater and Venayagamoorthy (2014), using the NT_L-ST_L parameter space (see Discussion). First the turbulence was classified as being shear-dominated ($Ri_g < 0.25$) or buoyancy-dominated ($Ri_g > 0.25$). Next for shear-dominated turbulence, it was assumed that the largest overturns (L_E) scaled with L_{kS}, and thus $k = (SL_E)^2$. Likewise, for buoyancy-dominated turbulence, L_E scaled with L_{kN}, so $k = (NL_E)^2$. Using the computed values of dissipation, NT_L and ST_L were calculated. Finally, for points falling into an inertia-dominated regime, defined as $NT_L < 1$ and $ST_L < 3.3$, the turbulent kinetic energy was recalculated as $k = (\varepsilon L_E)^{2/3}$, by assuming that L_E scaled with $L_{k\varepsilon}$. This critical shear parameter ($ST_L \sim 3.3$) was chosen, because it reflects the flor conditions in which production and dissipation are in approximate balance in the log layer of unstratified channel flow (Mater and Venayagamoorthy, 2014; Pope, 2000).

Results and Discussion

Experimental Conditions

Wind speeds during the measurement period were typically around 5 m/s (Fig. 2.5a) and were predominantly directed perpendicular to the axis of the upper estuary (NE-SW). The estuary was stratified for the entire study period with a median maximum N^2 of 0.14 s^{-2}. That indicates that the NRE was about as strongly stratified as most salt wedge estuaries, which typically have a maximum N^2 of around 0.1 s^{-2} (Peters, 1997; Kay and Jay, 2003; Wang et al., 2011). At the times and heights at which turbulence was observed, N^2 ranged from 10^{-5} to 10^{-1} s^{-2}, with a mean value of 10$^{-2.6}$ s^{-2} (Fig. 2.7a). The average shear when turbulence was observed was 0.13 s^{-2} (Fig. 2.7b).

There were three distinct wind events (towards N, NE, and SW) and four salinity stratification events: 1) initially stratified, 2) weakly stratified, 3) entrance of a salt wedge, 4) strongly stratified (Fig. 2.5b). The estuary was initially strongly stratified with surface-to-bottom salinity differences of 15 PSU, but this stratification weakened for several days during the northward wind. As the wind shifted to northeastward, which is down-estuary in the lower part of the NRE, the salt wedge was advected up-estuary, past the sensors. The study site remained strongly stratified for the rest of the experiment. Profiles of the along and across-channel currents (Fig. 2.5c-d) reveal a two-layer flow pattern throughout the deployment. Additionally, semidiurnal flow reversals indicate a wind-driven barotropic seiche (Luettich et al., 2002). A wave peak for waves of 1-3 second periods were present in most vertical velocity spectra, however, wave orbital motion only significantly affected the -5/3 region of the frequency spectrum in 10% of the 10-min intervals.

The water column was very stable and turbulence was scarce (Fig. 2.5b) for much of the deployment. However, persistent along-channel salinity gradients in both the upper and lower water column in the upper Neuse (Robbins and Bales, 1995) indicate that vertical mixing must occur. There was a wide-range of Ri_g during the measurement period (Fig. 2.6a), but $Ri_g < 0.25$ (cool colors) rarely occurred below the surface mixed layer. While there were periods in which $Ri_g < 0.25$ near the bottom boundary, the middle of the water column, where the ADV/CTs were placed, it was typically observed that $Ri_g \gg 0.25$. Time series of Ri_g at the height of each ADV/CT are shown in Fig. 2.6b-d. At 1.3 m and 1.9 m above bottom, $Ri_g < 0.25$ for only 15% of the 10-minute intervals. At 2.5 m above bottom, the flow was more unstable, with $Ri_g < 0.25$ for 57% of the 10-minute intervals. Here, the flow was considered turbulent when the vertical velocity spectrum had an inertial subrange with a slope of -5/3 at frequencies between 1.5 and 3.75 Hz. Turbulence was indeed scarce, with turbulence occurring only during 18%, 12%, and 13% of the 10-minute intervals for the ADV/CTs at 1.3, 1.9, and 2.5 m above bottom, respectively. The majority of the turbulence that was observed appeared to occur when $Ri_g \gg$ 0.25. The reasons for this surprising observation will be discussed in the following sections. Even given the fact that stratified estuaries typically have large values of Ri_g, the values observed in NRE were on average far greater than those of previous studies in strongly stratified estuaries (e.g., Holleman et al., 2016; Krvavica, 2016).

Turbulent Kinetic Energy Budget

All of the terms of the turbulent kinetic energy budget were approximately normally distributed on a log scale (Fig. 2.8). For 10-minute intervals in which the velocity spectra passed the -5/3 fit test, dissipation (Fig. 2.8a) had an average value of 2.5×10^{-6} m^2s^{-3}, which was half an order of magnitude greater than production estimates (Fig. 2.8b) and two orders of magnitude

greater than the buoyancy flux estimates (Fig. 2.8c). The mean dissipation was larger than values typically observed in the open ocean ($\varepsilon \sim 10^{-9}$ m^{2}s^{-3}; Gregg et al., 1993) but less than observed in previous studies of salt wedge estuaries, where $\varepsilon > 10^{-4}$ m^{2}s^{-3} (Geyer et al., 2008; Holleman et al., 2016).

To verify that the dissipation was in fact larger than the production, the dissipation estimates were recomputed using a higher noise floor (3.5 Hz instead of 3.75 Hz) to check that they were not being overestimated. These estimates did indicate that the noise floor had some effect on the dissipation values at 1.3 m above bottom, but not enough explain why dissipation was greater than production. The other possibility is that the production was underestimated. There were times in which the Aquadopp had lower estimates of the shear than the ADCP, especially at 1.3 m above bottom. However, even if the higher ADCP values were used, dissipation was still higher than production during these time periods.

Times series of the terms in the turbulent kinetic energy budget are shown in Fig. 2.9. Although turbulence was quite strong, 10-minute intervals in which our methods could observe it were scarce. The strongest and most frequent turbulence observed was at the lowest ADV (1.3 mab) and corresponded to when the salt wedge advected past the sensors on Aug. 10. During this time, the sensor was in the bottom boundary layer and experienced strong currents. Three relatively strong turbulent events were observed at the location of the top ADV (2.5 mab) during strong northward wind events on Aug. 6, 7, and 8. During these periods, the nearly up-estuary wind stress opposed normal estuarine circulation and reduced stratification in the upper part of the water column, making it more susceptible to vertical mixing.

Comparing the magnitudes of turbulent kinetic budget terms is difficult because uncertainties in the estimates are large. Estimates of dissipation rates of isotropic turbulence have

the smallest uncertainties, while estimates of production and buoyancy flux often have uncertainties so large that the confidence intervals include zero (Figs. 2.9, 2.10). The dissipation and production values were mostly the same order of magnitude within the uncertainty of the estimates. However, the turbulence associated with the advection of the salt wedge (Fig. 2.10) had higher dissipation rates than production at the height of the bottom sensor (Fig. 2.10a). Strong bottom shear during this event suggests that this was likely bottom boundary layer turbulence. The salt wedge event also appeared to produce some interfacial turbulence, as the best balance between production and dissipation occurred at the height of the middle sensor (Fig. 2.10b), which was closest to the height of the pycnocline at the onset of the salt wedge event. During the first wind event on Aug. 6, which coincided with the initial stratified salinity event, dissipation and production estimated from the topmost sensor were approximately equal. The two wind events on Aug. 7 and 8, aligned with the weakly stratified period, where dissipation rates estimated from the top sensor were mostly larger than production (Fig. 2.10c). Low values of Ri_g near the surface during these time periods (Fig. 2.6a) suggest that this turbulence could have been produced in the surface wind-mixed layer and transported downward past the sensor.

Turbulence Length Scales

The size of the turbulent overturns was estimated with L_E. All characteristic turbulent length scales were approximately log-normally distributed (Fig. 2.11). The length scales that characterize the largest turbulent eddies (all except L_K) have mean values around 0.1 m, with maximum values of 2-3 meters, or half the water column height. L_{kN} and L_{kS} are both slightly larger than their counterparts, L_O and L_C, suggesting anisotropic eddies were probably present. Additionally, it was observed that L_C was typically less than L_O and L_{kS} was less than L_{kN}. The gradient Richardson number can be expressed as $Ri_g = (L_C/L_O)^{4/3}$, so for $Ri_g < 0.25$, $L_C < L_O$,

75

and similarly $L_{kS} < L_{kN}$. However, $L_C < L_O$ does not require that $Ri_g < 0.25$, only that $Ri_g < 1$. Given the mean values of L_C and L_O, it was typical that $0.25 < Ri_g < 1$, which is consistent with values of Ri_g displayed in Fig 2.6. The values of L_K were several orders of magnitude smaller than the other turbulent length scales, which should be sufficient scale separation for an inertial turbulent cascade.

Time series of the turbulent length scales are shown in Figs. 2.12 and 2.13. During periods of strong turbulence, the largest overturns (L_E) reached 2-3 m. Throughout the experiment L_O, L_C, L_{kN}, and L_{kS} were all quite close to L_E, though L_O and L_{kN} were typically better at correlated with L_E than L_C and L_{kS} during periods of strong stratification. During the first two strong wind events (Aug. 6 and 7) and the salt wedge event (Aug. 9 and 11), L_C and L_{kS} were better estimates of L_E, suggesting that shear was more important than stratification in determining the size of the eddies. Since $L_{k\varepsilon}$ represents the largest eddies present when the effects of shear and buoyancy are negligible, it is not surprising that it typically overestimated the size of the overturns in this strongly stratified estuary.

There is also an inverse relationship between the largest scales and the smallest scale, L_K. The largest scales grow as turbulent intensity increases, reaching their peak values during the most energetic turbulence, before decaying as turbulence decays. L_K, on the other hand reaches a minimum during the most energetic turbulence.

Importantly, all of the turbulent length scales were smaller than the resolution of Ri_g (dashed line in Fig. 2.12-2.13) for much of the deployment, suggesting that the resolution of velocity and density measurements may not have been sufficient to resolve the shear and stratification at scales that affect turbulence. Therefore, although it appears that turbulence was observed at $Ri_g \gg 0.25$ (Fig. 2.6), this may be an artifact of the resolution of the velocity and

density profile measurements. If Ri_g could be resolved at the characteristic length scales observed, it is possible that $Ri_g < 0.25$. If Ri_g was in fact overestimated, then the ratio of the shear length scales (L_C and L_{kS} to the buoyancy length scales (L_O and L_{kN}) would also decrease. Under such strongly stratified conditions, the turbulent length scales are often less than 1 cm, making it unrealistic to get Ri_g at a high enough resolution to accurately determine the stability of water column when the turbulence is generated, even with the high resolution Aquadopp measurements. Additionally, many of the length scale estimates rely estimates of either N or S. Since these terms appear in the denominator of the length scale estimates, underestimation of those terms as a result of low-resolution measurements would result in overestimates of the length scales.

Mixing Efficiency

Under the strongly stratified conditions found in the NRE, the efficiency of mixing observed was typically much less than the value, $R_f = 0.17$, proposed by Osborn (1980). Values of R_f and $Re_b = \varepsilon / v N^2$ were divided by stratification event (Fig. 2.14a) and along-channel current velocity (Fig. 2.14b), sorted according to Re_b, and bin averaged into groups of 30 points. Bin averages in the energetic (isotropic) regime ($Re_b > 100$) suggest that R_f varies with Re_b, with the least efficient mixing occurring during periods of weak stratification (high Re_b, Fig. 2.14a) and strong along-channel currents (Fig. 2.14b). These results are in good agreement with the direct numerical simulations of Shih et al. (2005) and field observations of (Monismith et al., unpublished manuscript) who proposed a relationship of the form $R_f = C\,(\varepsilon/vN^2)^{-1/2}$, where C is a constant equal to 1.5 (Shih et al, 2005) or 2.7 (Monismith et al., unpublished manuscript). For values of $Re_b < 100$, R_f appears to decrease, which may be a result of reversible fluxes. This

result is consistent with the DNS studies of Venayagamoorthy and Koseff (2016), which found that R_f underestimates the flux Richardson number for low Re_b.

To understand how buoyancy affects turbulence, the data can be plotted in Re_t-Fr_t parameter space (Fig. 2.15). Following Ivey and Imberger (1991), the diagram is divided into 3 regions: 1) buoyancy-affected regime, but turbulence may be isotropic at the smallest scales, 2) buoyancy-controlled regime, 3) turbulence is suppressed by a combination of buoyancy and viscosity, leaving only internal wave motions. In theory, all of the turbulence should be found in Regions 1 and 2. However, the data indicate that some of the turbulence occurred in Region 3, where it should have been dampened by buoyancy and friction. This may be due to the anisotropy of the turbulence affecting the accuracy of the dissipation calculations. Under-resolution of N can also have affected where points fell in the parameter space. In a study charactering the effectiveness of using a fit to the inertial subrange to estimate dissipation, Bluteau et al (2011), suggest excluding all data with $Re_b < 100$, which affects all of the points in Region 3.

The Re_t-Fr_t diagram can also provide insight into how buoyancy affects the efficiency of vertical mixing, as R_f varies not only with Re_b, but also with Fr_t. The maximum value of flux Richardson number we observed was $R_f \sim 0.3$, which is in line with previous studies (Smyth et al., 2001; Mashayek and Peltier, 2013). The most efficient mixing was observed in buoyancy-controlled Region 2 (Fig. 2.15a), where values of Re_t become large enough to allow for efficient mixing of strongly stratified flow. These results differ from those of lab experiments (Ivey and Imberger, 1991), which found that the most efficient mixing occurred at the transition between regions 1 and 2 ($Fr_t = 1$). When $L_O \sim L_T$ ($Fr_t = 1$), the available potential energy stored in the largest overturn provides energy very efficiently to the inertial subrange, resulting in efficient

mixing. When the largest eddies are suppressed by buoyancy forces, the mixing is less efficient. However, the findings from controlled lab experiments (Ivey and Imberger, 1991) may not accurately reflect the characteristics of turbulence in the field. The findings in this study, that most efficient mixing was observed for Fr_t in the range 0.2-1 (Region 2) are consistent with other field studies (Davis and Monismith, 2011; Dunckley et al., 2012; Walter et al., 2014). Davis and Monismith (2011) suggested that this could be caused by internal wave forcing and nonlocal advection of TKE. Considering that L_E can overestimate the size of the overturns in strongly stratified environments, it is possible that Fr_t was underestimated, and the most efficient mixing did indeed occur for Fr_t close to unity.

A recent study (Mashayek et al., 2017) provides more insight into the utility of the Re_t-Fr_t parameter space. They determined that the key constituents of efficient mixing are that $L_E \geq L_O$ $(Fr_t = (L_O/L_E)^{2/3} \leq 1)$ and that there is a sufficient separation between the largest and smallest turbulent scales in the inertial subrange (sufficiently large Re_b), both of which are consistent with our findings. They suggest that in typical stably stratified shear flows, large initial overturns, which scale with L_E provide a large pool of potential energy for scales smaller than L_O, leading to a very efficient turbulence cascade when $L_E > L_O$. When these large overturns are present, the ratio of L_O/L_E is often used as a proxy for the age of decaying turbulence. It has been found that this ratio increases with the time from which turbulence is generated (Wijesekera and Dillon, 1997), so decaying turbulence in the buoyancy-affected Region 1 is older than turbulence in the buoyancy-dominated Region 2. Additionally, when $L_O/L_E < 1$ (Region 2), turbulence is anisotropic and affected by buoyancy (Mater and Venayagamoorthy, 2014). Therefore, our data suggest that anisotropic turbulence produced the most efficient mixing.

Interestingly, the part of the parameter space where the highest R_f occurred coincided with initially stratified and strongly stratified events (Fig. 2.15b). The first wind event (Aug. 6), associated with the initial period of stratification, appeared to have anisotropic turbulence, which resulted in efficient mixing. The final two wind events (Aug. 7 and 8) and the salt wedge event produced the strongest turbulence; the associated turbulent mixing was the least efficient. However, from their locations on the Re_t-Fr_t parameter space, there is no discernible difference between the turbulence likely generated at the surface during the last two wind events, and the bottom boundary turbulence produced during the advection of the salt wedge.

Given that some of the observed turbulence is likely anisotropic, and it could be affected by both shear and stratification, the NT_L-ST_L parameter space (Mater and Venayagamoorthy, 2014) is a better framework for understanding the state of the turbulence in our dataset. This framework classifies stratified shear flow into one of three regimes: inertia-dominated, shear-dominated, or buoyancy-dominated (Fig. 2.16). The highest R_f values occurred when the turbulence was anisotropic and fell in the buoyancy and shear-dominated regimes (Fig. 2.16a). However, some of the observed turbulence, including much of that associated with the advection of the salt wedge, appeared to fall into the inertia-dominated regime (Fig. 2.16f). In this regime, turbulence is expected to be isotropic and decaying, with $P < \varepsilon$. This was true of most of our observations that fell in inertia-dominated part of the parameter space (Fig. 2.16b). Some of this inertia-dominated turbulence had decayed to the point that at the time of observation, neither shear nor stratification still affected it, even though it was likely initially produced by shear, and previously affected by the background stratification. Thus, this turbulence behaves like unstratified turbulence, which is not well described by Ri_g. However, the decay time scale, T_L, for this turbulence was typically about 3-5 minutes, suggesting that not all of the turbulence was

decaying during the course of the 10-min interval. The length scales associated with this inertia-dominated turbulence were typically much smaller than the resolution of not only the density and shear measurements, but also the velocity measurements used to compute the dissipation. Therefore, it is difficult to accurately place these data points in the NT_L-ST_L parameter space.

Additionally, there may be some variability in the critical shear and buoyancy parameters used to determine the location of the inertia-dominated regime. The shear parameter was selected by Mater and Venayagamoorthy (2014) as the location where production and dissipation are in balance in a boundary layer. However, it appears that production was in balance with dissipation for some of the turbulence observed for $2 < ST_L < 3.3$ as well as for $0.7 < NT_L < 1$ (Fig 2.16b). Thus, it is possible that the inertia-dominated regime should occupy a smaller area of the parameter space. Finally, there is a lot of uncertainty in where the observations fall in the parameter space, so it is possible that some of the inertia-dominated turbulence could be classified as buoyancy or shear dominated.

In the buoyancy-dominated regime, $L_O/L_E < 1$ (Fig. 2.16c), indicating that the turbulence was anisotropic, which is consistent with the findings from the Re_t-Fr_t diagram. One advantage of the NT_L-ST_L parameter space is that it takes into account the effects of shear. As a result, an analogous ratio, L_C/L_E, was computed for turbulence affected by shear, which indicated that in the shear-dominated regime, $L_C/L_E < 1$, and thus the turbulence was anisotropic (Fig. 2.16d). Analysis of Re_b (Fig. 2.16e) indicates that the most energetic turbulence occurs in the inertia and shear-dominated regimes, while the least energetic turbulence is generally restricted to the buoyancy-dominated regime.

Overall, the NT_L-ST_L framework provided a more complete understanding of the characteristics of turbulence the stably stratified shear flows we observed. It also clarifies the

distinction between turbulence generated near the surface during wind events, and turbulence generated in the bottom boundary during the salt wedge event. Turbulence observed during the advection of the salt wedge, was generally classified as inertia-dominated turbulence, which was energetic, but not very efficient at mixing (Fig. 2.16f). However, some anisotropic turbulence was produced during the advection of the salt wedge. Shear-dominated and buoyancy-dominated turbulence typically occurred during periods of strong stratification. During the first wind event (Aug. 6), corresponding to the initial period of stratification, the turbulence was anisotropic and energetic, and it produced efficient mixing. In the NT_L-ST_L framework it now becomes apparent that the other two wind events (Aug. 7 and 8), were also energetic and anisotropic, but produced less efficient mixing. This lack of efficient mixing was likely due to the fact that the water column was more weakly stratified during the last two wind events than the first. This anisotropy, associated with shear, was not evident in the Re_t-Fr_t framework. The turbulence generated during the strongly stratified period (after Aug. 11) mostly fell into the buoyancy-dominated regime, which was the least energetic but had high mixing efficiencies.

Conclusions

Turbulence in strongly stratified estuaries, such as the NRE, is challenging to study, due to its scarcity, short time scales, and small length scales. In this study, we used some of the most accurate and high-resolution sensors available to attempt to characterize turbulence in the NRE, and the shear and density stratification that affect it. Our measurements include some of the strongest observed stratifications ($N^2 = 0.14\ s^{-2}$), yet high turbulent dissipation rates (mean $\varepsilon = 2.4 \times 10^{-6} m^2/s^3$). Turbulent length scales estimated from our measurements suggest that the overturns were often small (1-10 cm), smaller than the spatial resolution of velocity and density profile measurements (25 cm), making it difficult to quantify the effects buoyancy and shear on

turbulence properties. Application of a framework recently proposed by Mater and Venayagamoorthy (2014), suggested that some of the observed turbulence fell into an inertia-dominated regime, in which the turbulence was decaying, and eddies were no longer large enough to be affected by buoyancy or shear. While it is possible that points fell in this region due to measurement limitations, turbulence properties calculated from our measurements are consistent with it being decaying turbulence. Dissipation was generally larger than production and the Ellison length-scale was smaller than the Ozmidov scale and the Corrsin scale. Mixing efficiencies associated with this turbulence were generally quite low ($R_f < 0.15$). In the shear and buoyancy-dominated regimes, mixing tended to be more efficient, with peak values of $R_f \sim 0.3$.

We identified that turbulence in our measurements was generated by two distinct mechanisms: shear generation, associated with advection of a salt wedge, and wind mixing. The turbulence associated with the salt wedge appeared to be generated somewhere other than the discrete points where our turbulence sensors were located. Most of the turbulence we observed associated with this event appeared to have been decaying at the observed locations, and fell into an inertia-dominated regime, where mixing was inefficient. The turbulence generated by wind-shear in the upper part of the water column had length scales ~ 1 m, large enough that our measurements resolved shear and stratification at the relevant scales. This turbulence was generally anisotropic, occurring in the shear and buoyancy-dominated regimes. When the water column was strongly stratified, this wind-generated mixing produced efficient mixing.
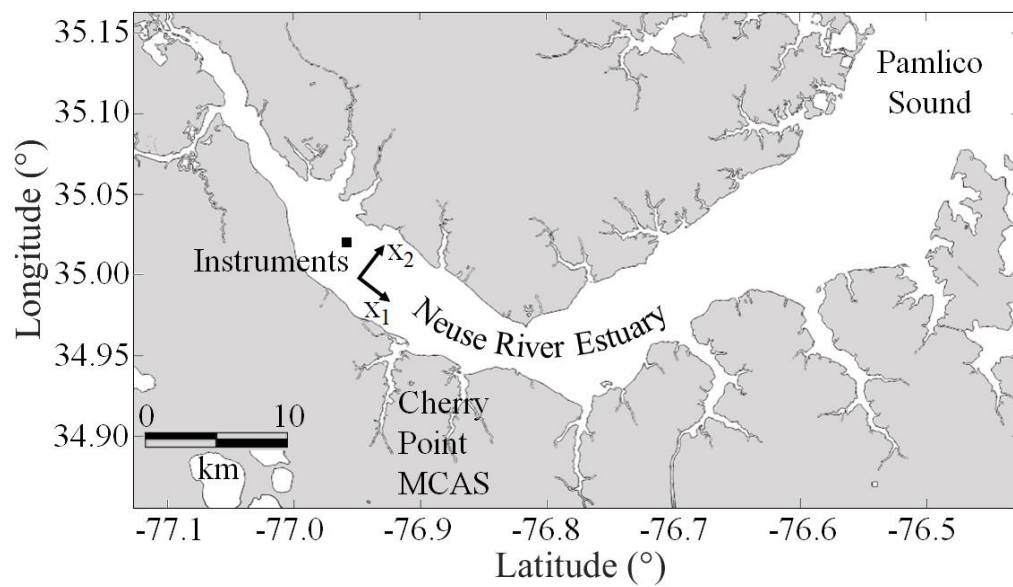
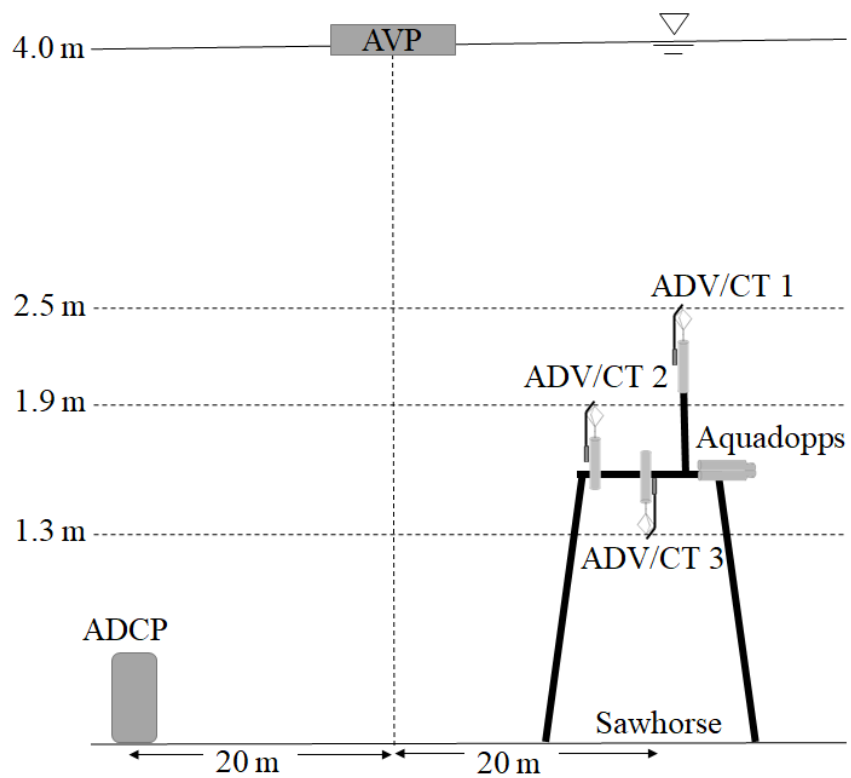Figure 2.1: Map of the Neuse River Estuary showing the location of the study site

Figure 2.2: Schematic diagram of instrument layout for the deployment. The CTD string was located 20 m north or the AVP (not shown).
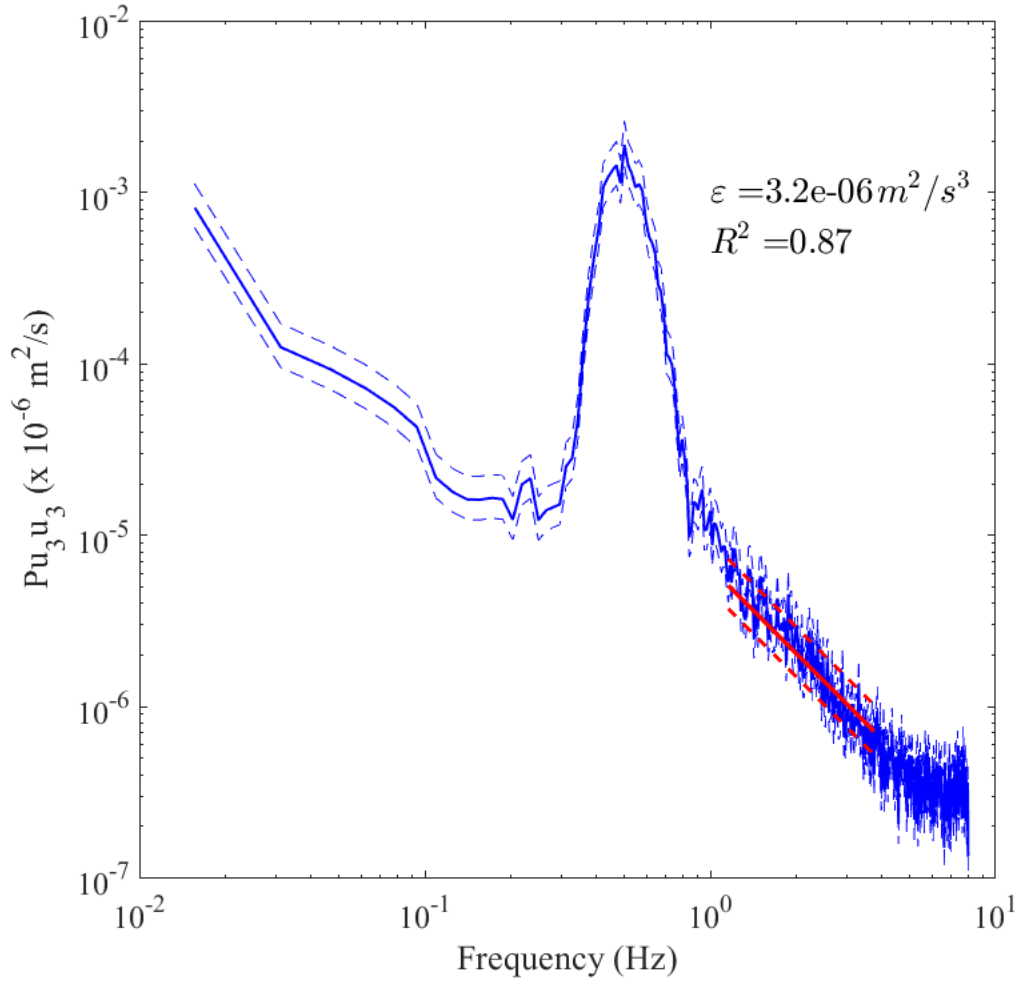
Figure 2.3: Example power spectrum of vertical velocity (blue) from ADV, located 2.5 m above

bottom, with -5/3 fit (red) used to compute the dissipation. Dashed lines represent 95%

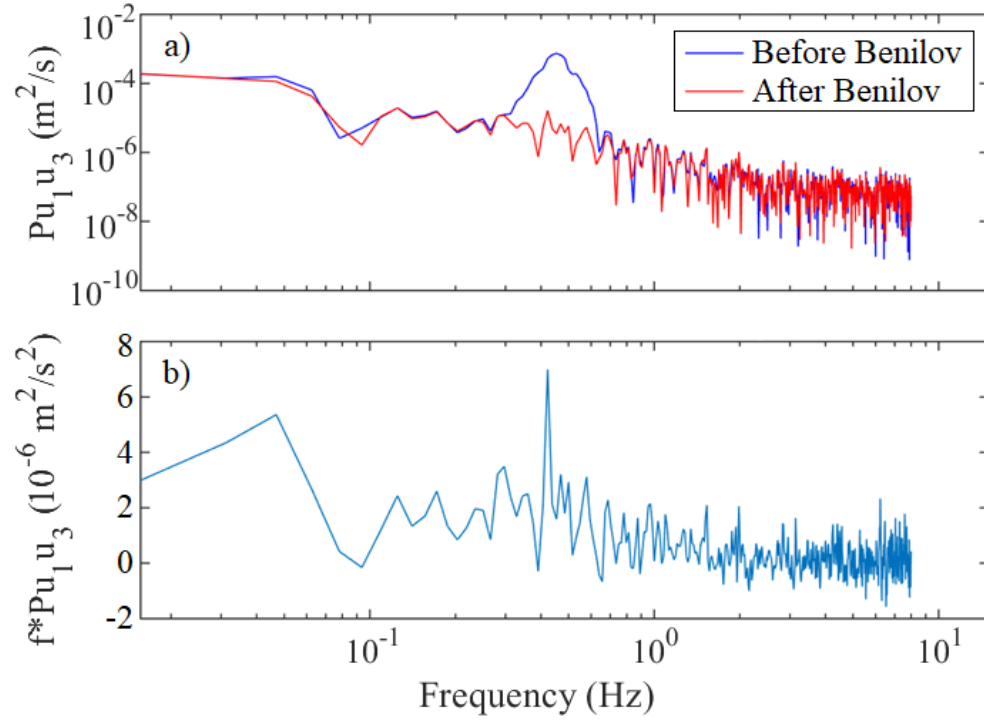confidence intervals on the spectrum (blue) and on the line of best fit (red).

Figure 2.4: a) Cospectrum and b) variance preserving cospectrum of along-channel and vertical velocity components. Panel a shows the original co-spectrum (blue) and the co-spectrum after the wave component has been removed using the pressure-correlation method (red). Panel b shows the variance preserving co-spectrum after the wave component has been removed.
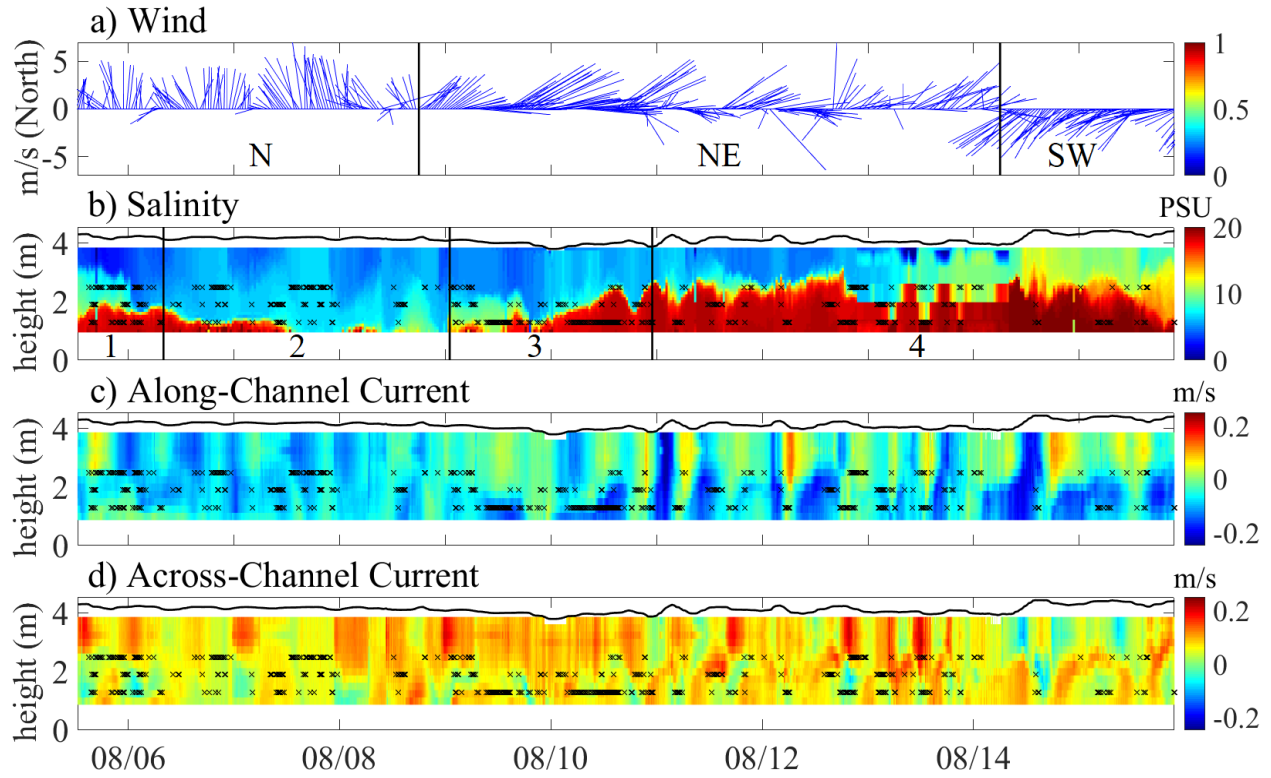
Figure 2.5: a) Wind direction, b) salinity profile, c) along-channel current profile, and d) across-channel current profile during August, 2013. Positive velocities correspond to down-estuary (along-channel) and towards the north shore (across-channel). During the experiment, there were three distinct wind events (towards N, NE, and SW) and four distinct salinity stratification events: 1) initially stratified, 2) weakly stratified, 3) entrance of salt wedge, 4) strongly stratified. Black x's respresent observations of turbulence at the heights of the ADVs (b-d).
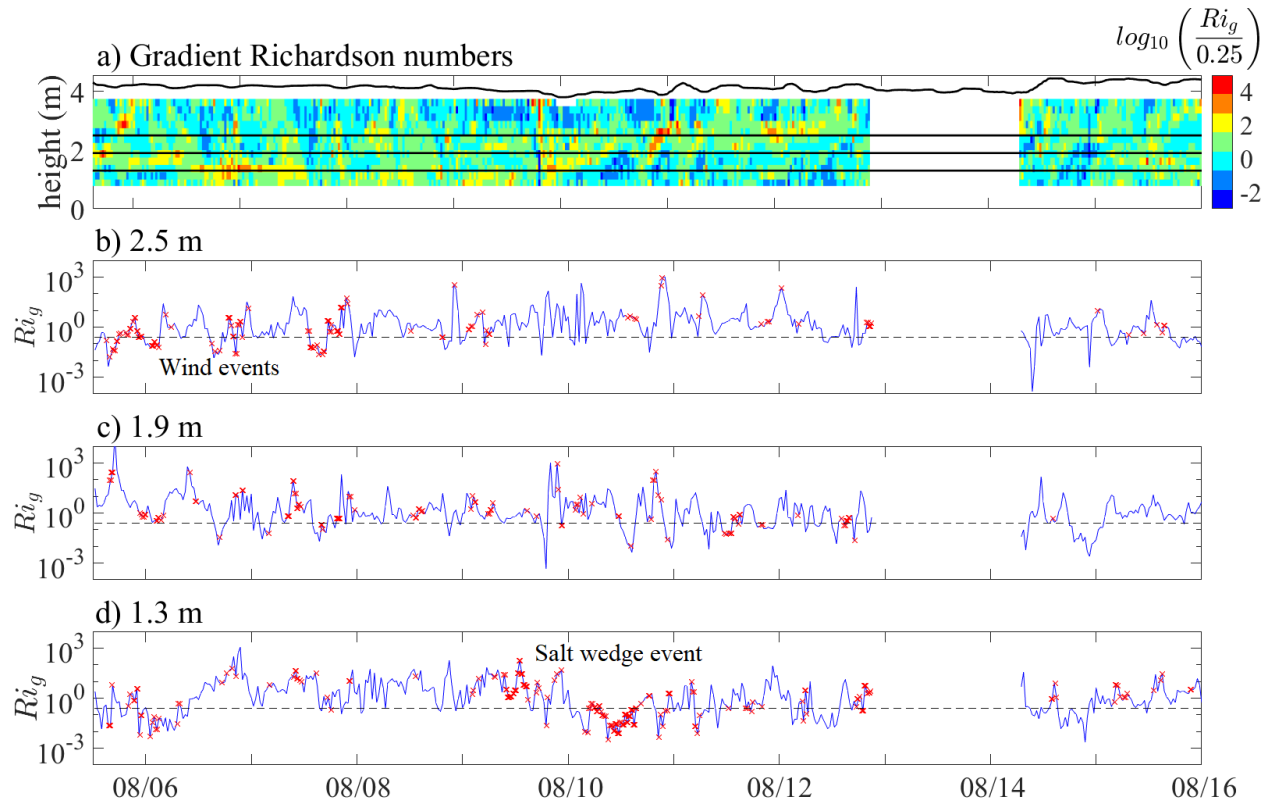
Figure 2.6: a) Profile of logarithm of normalized gradient Richardson numbers. Cool colors indicate sufficient shear to generate turbulence ($Ri_g < 0.25$). Horizontal black lines indicate heights of ADVs. Time series of gradient Richardson numbers at the heights of ADVs at b) 1.3 m, c) 1.9 m, and d) 2.5 m above bottom. A red x indicates a time when the vertical velocity spectrum had an inertial subrange with a slope of -5/3.
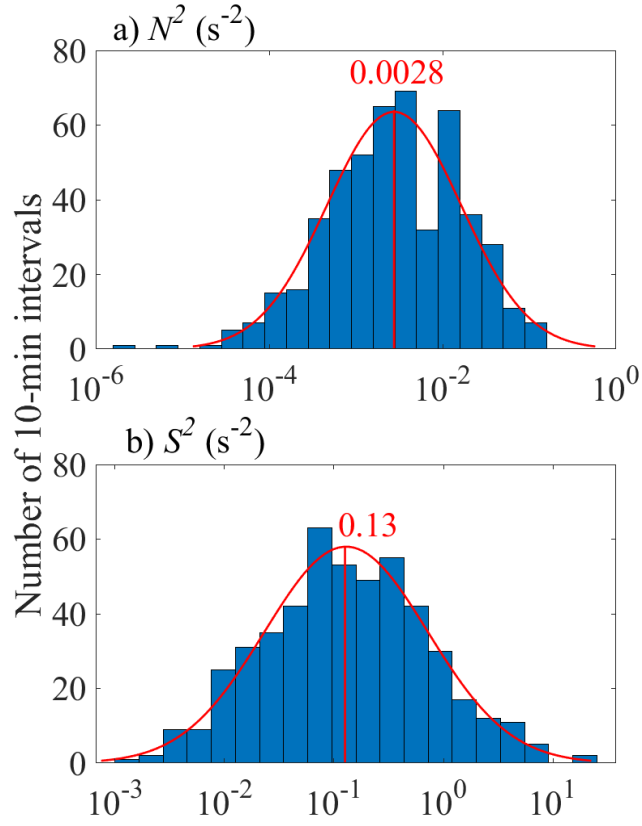
Figure 2.7: Histograms of a) N^2 and b) S^2 at the height of all 3 ADVs. Both are approximately normally distributed on a log scale. Mean values are indicated in red.
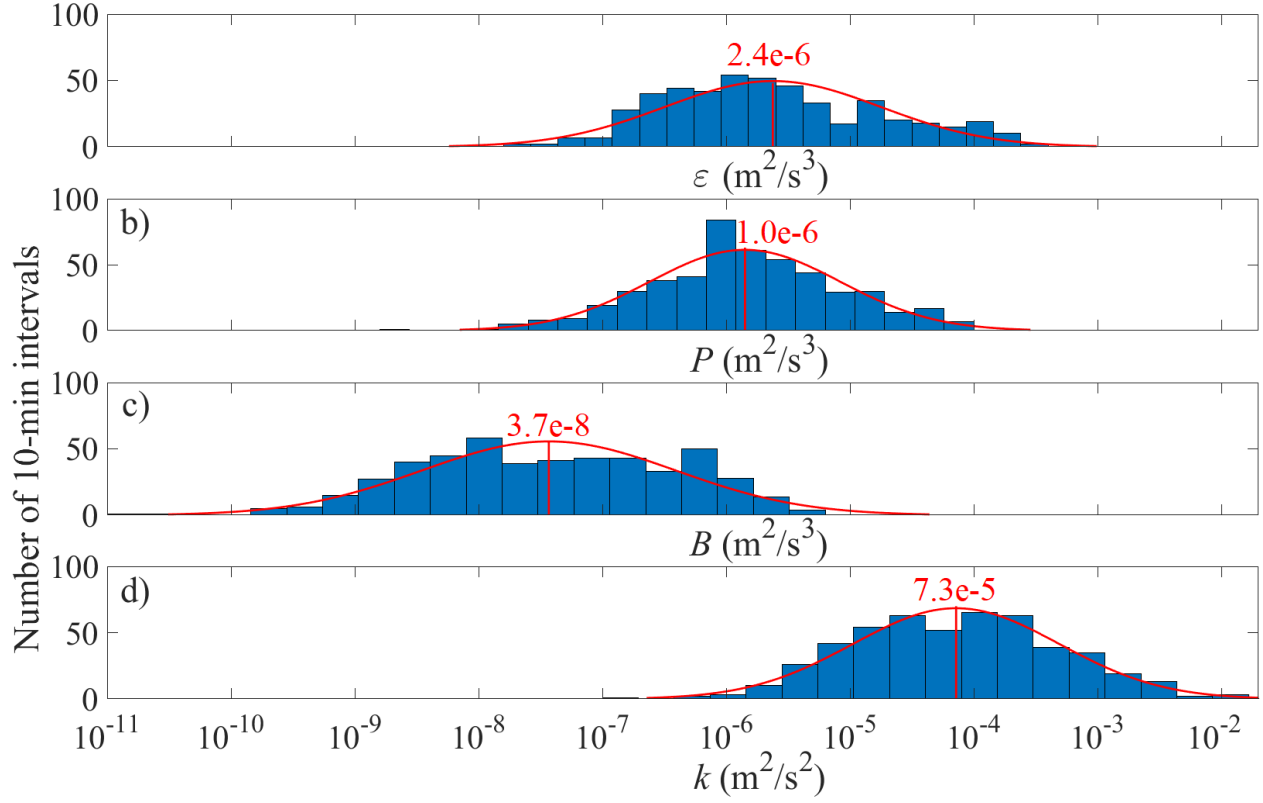
Figure 2.8: Histograms of a) dissipation, b) production, c) buoyancy flux, and d) turbulent kinetic energy from all 3 ADVs. All four terms are approximately normally distributed on a log scale. Mean values are indicated in red.
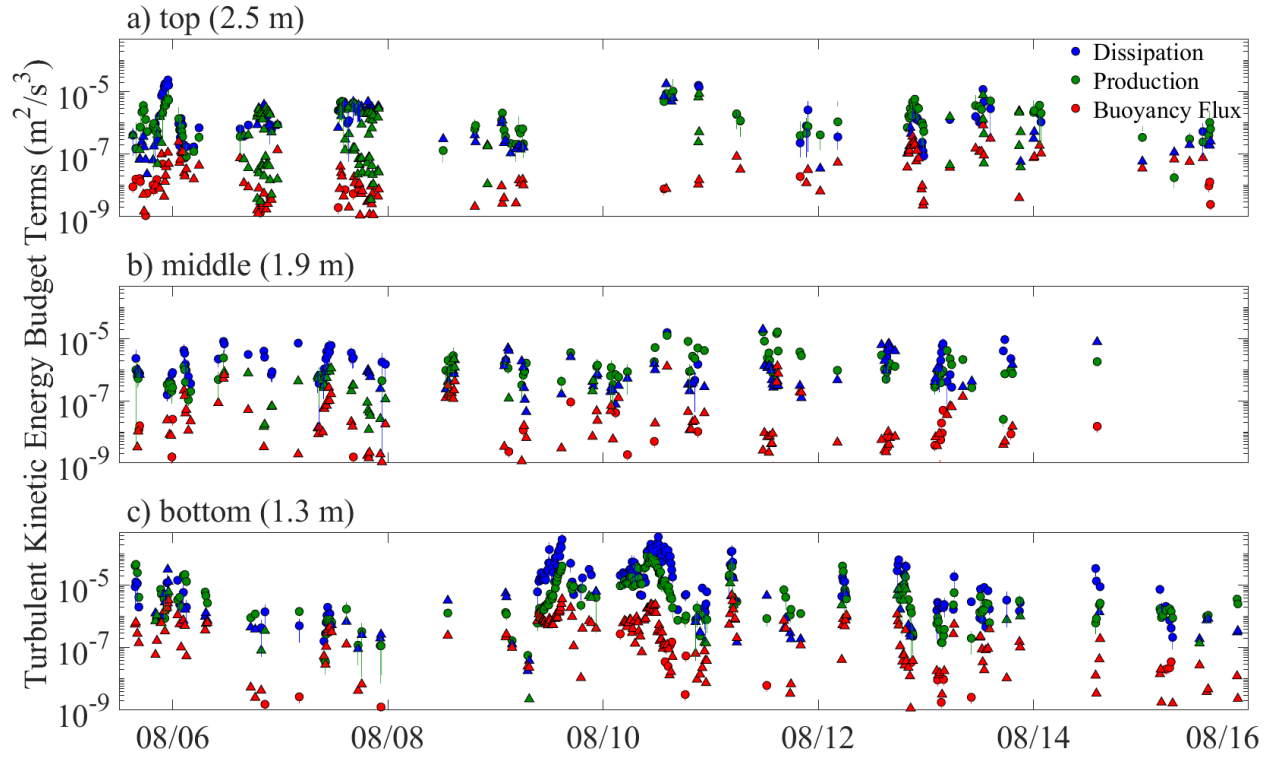
Figure 2.9: Time series of dissipation, production, and buoyancy flux at a) 2.5 m, b) 1.9 m, and c) 1.3 m above bottom. Error bars are 95% confidence intervals, but triangular points have larger uncertainties than the observed values.
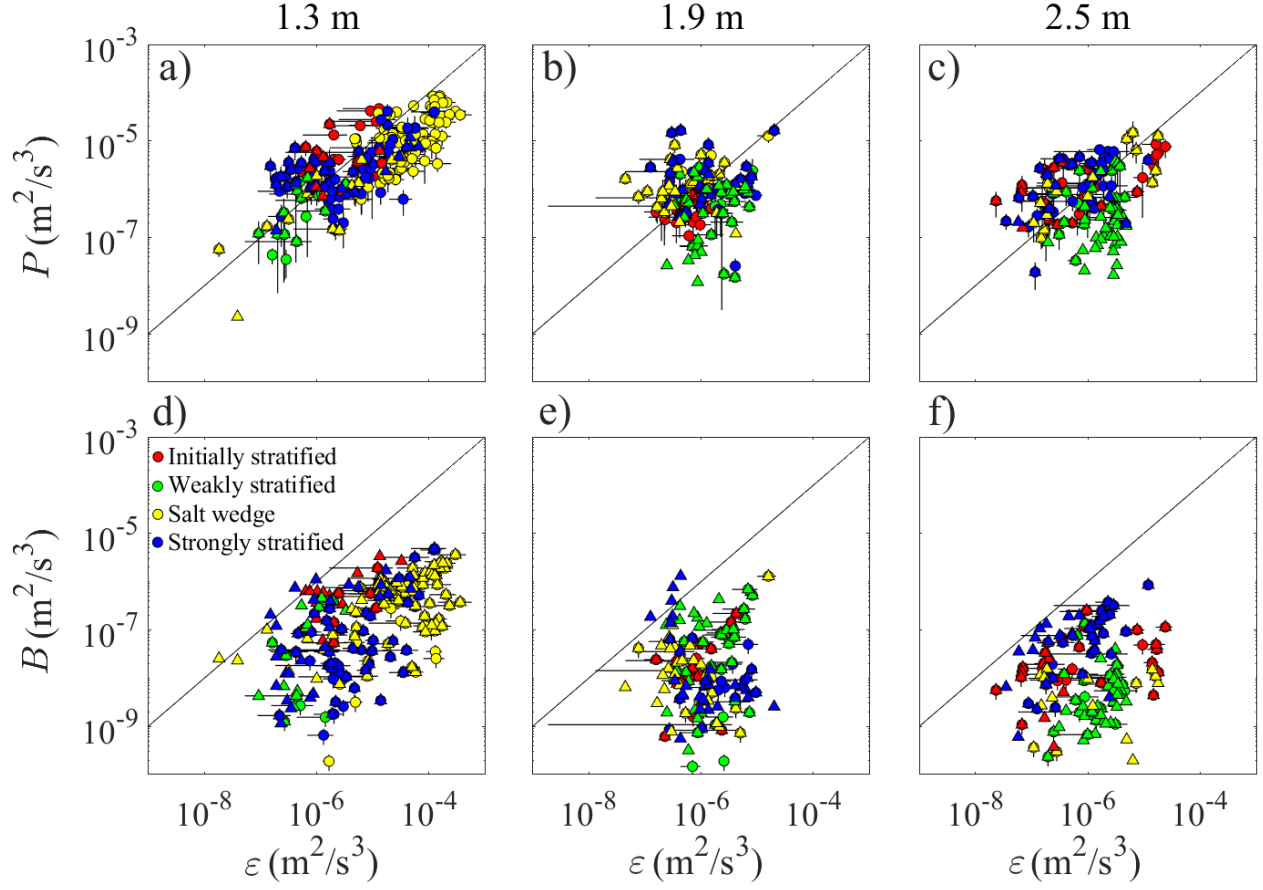
Figure 2.10: Production versus dissipation at a) 1.3 m, b) 1.9 m, and c) 2.5 m above bottom. Buoyancy flux versus dissipation at d) 1.3 m, e) 1.9 m, and f) 2.5 m above bottom. Points are colored by salinity stratification event (Fig. 5b). Error bars are 95% confidence intervals, but triangular points have larger uncertainties than the observed values.
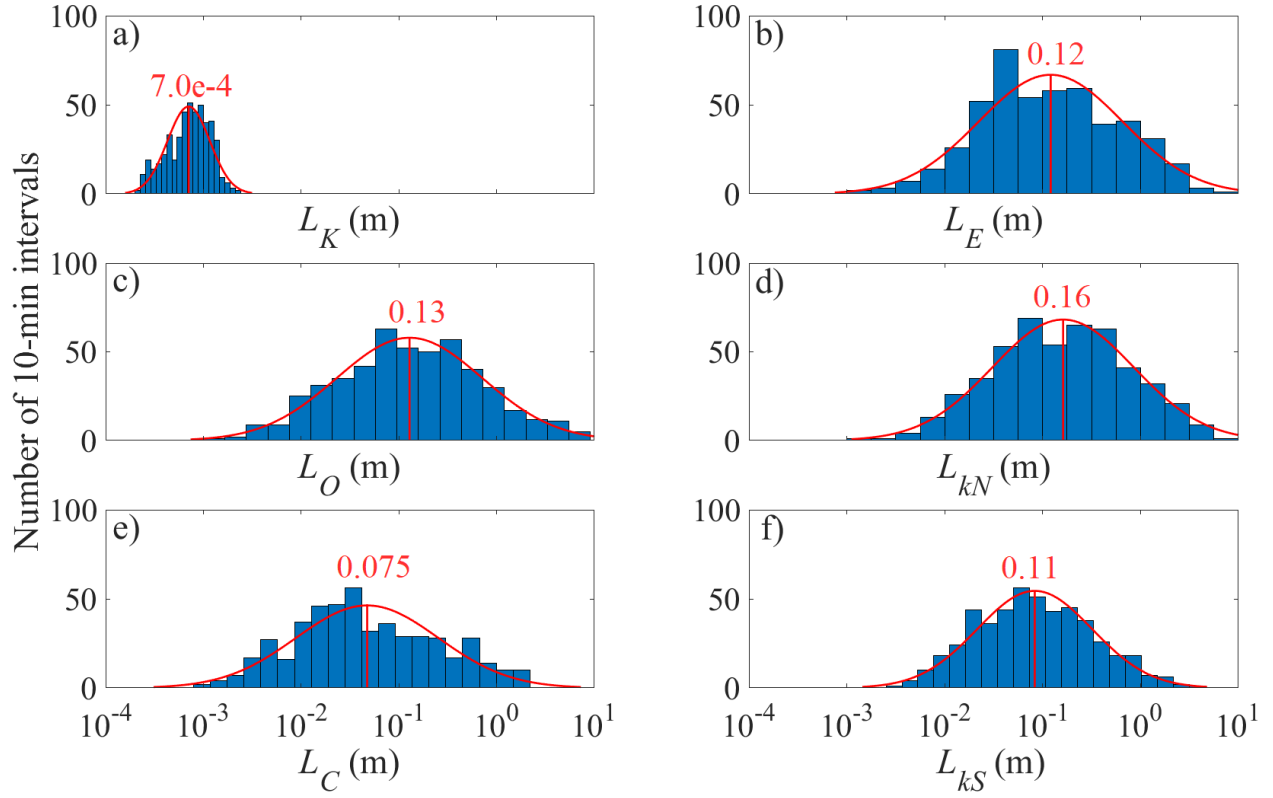
Figure 2.11: Histograms of important length scales: a) L_K, b) L_E, c) L_O, d) L_{kN}, e) L_C, and f) L_{KS}.

All length scales are approximately normally distributed on a log scale. Mean values are
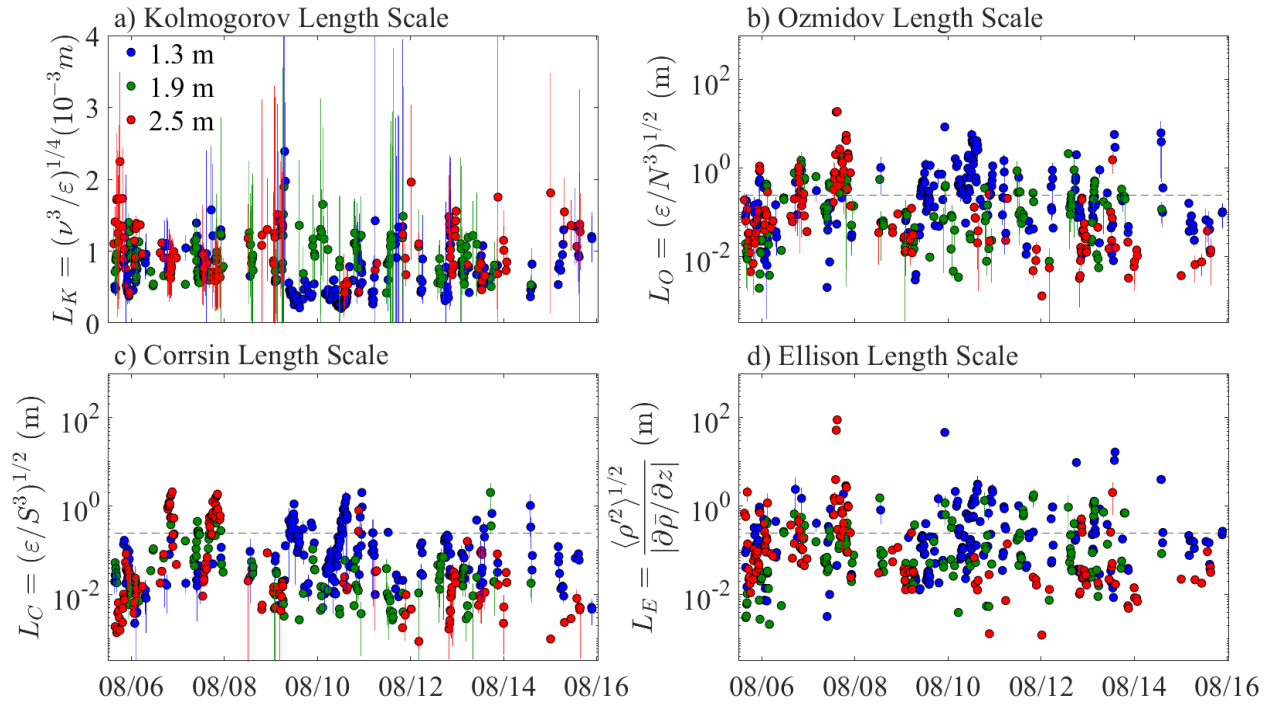
indicated in red.

Figure 2.12: a) Kolmogorov, b) Ozmidov, c) Corrsin, and d) Ellison length scales with 95% confidence intervals estimated from measurement from the three ADVs. The horizontal dashed lines indicate the resolution of the stratification and shear measurements (0.25 m).
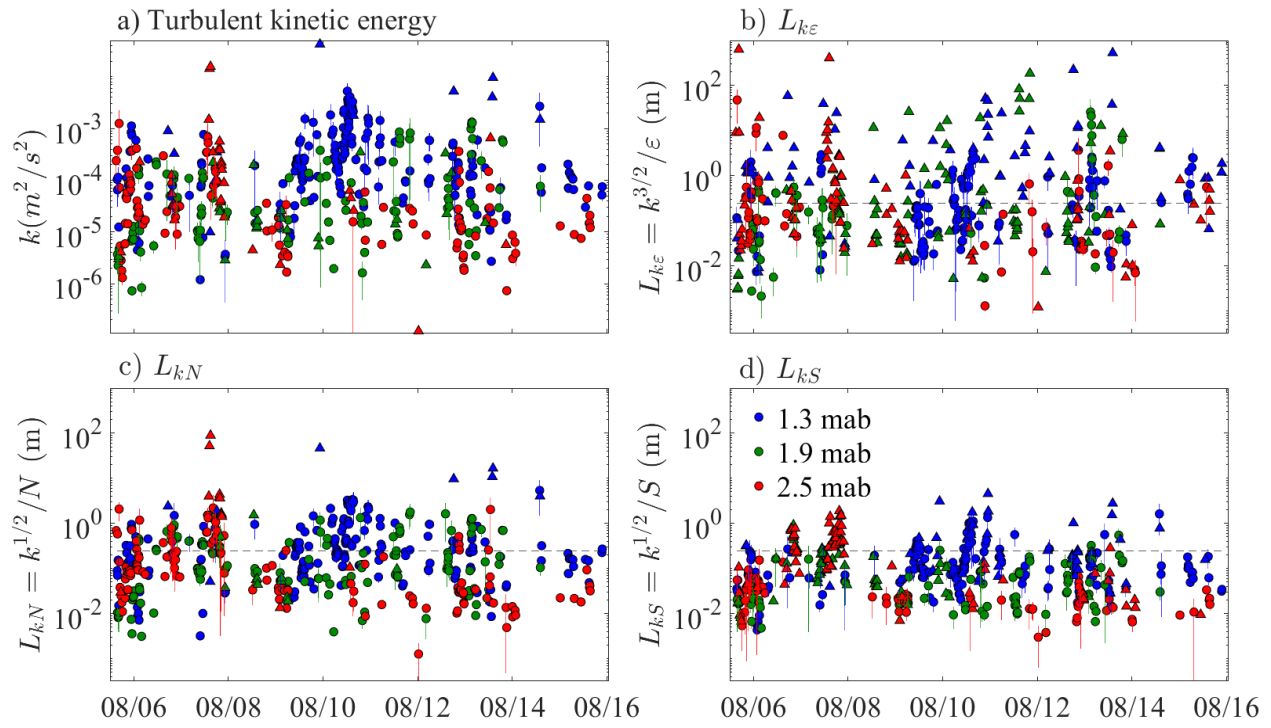
Figure 2.13: a) Turbulent kinetic energy, b) $L_{k\varepsilon}$, c) L_{kN}, and d) L_{kS} estimated from measurements from the three ADVs. Error bars are 95% confidence intervals, but triangular points have larger uncertainties than the observed values. The horizontal dashed lines indicate the resolution of the stratification and shear measurements (0.25 m).
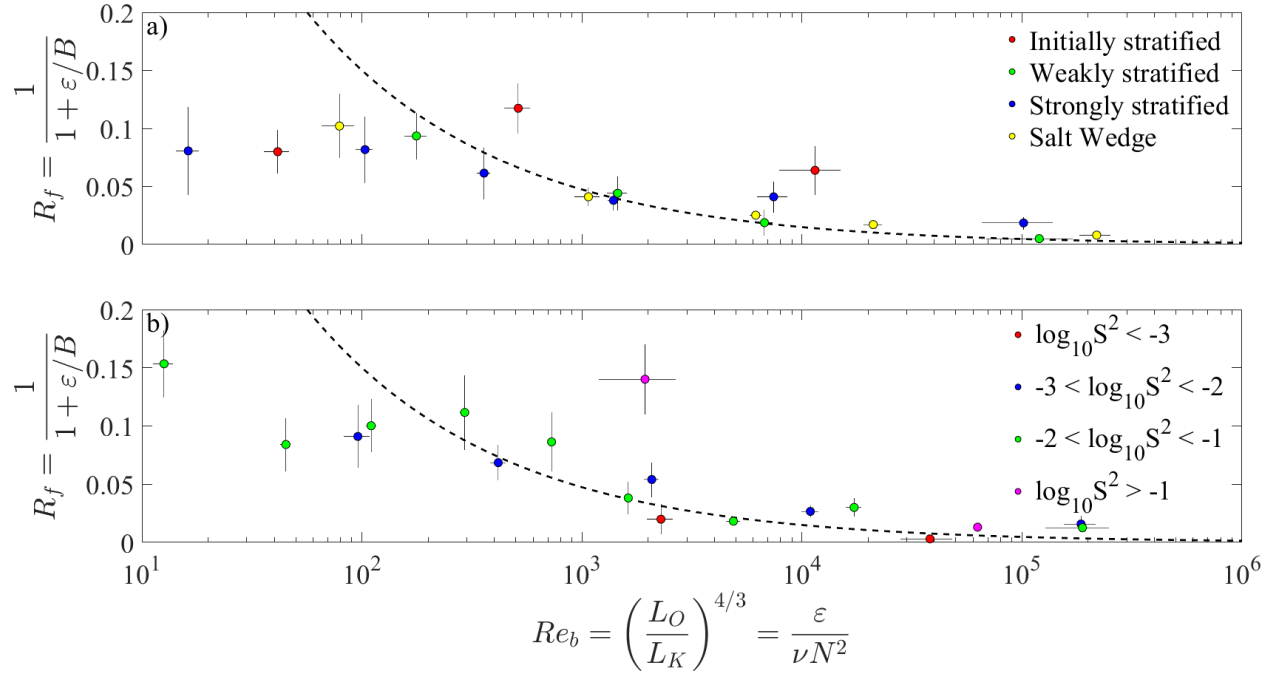
Figure 2.14: Flux Richardson number versus buoyancy Reynolds number with 95% confidence intervals, bin averaged by a) stratification event and b) S^2. The dashed line is the curve $R_f = 1.5 \, (\varepsilon/\nu N^2)^{-1/2}$ proposed by Shih et al. (2005).
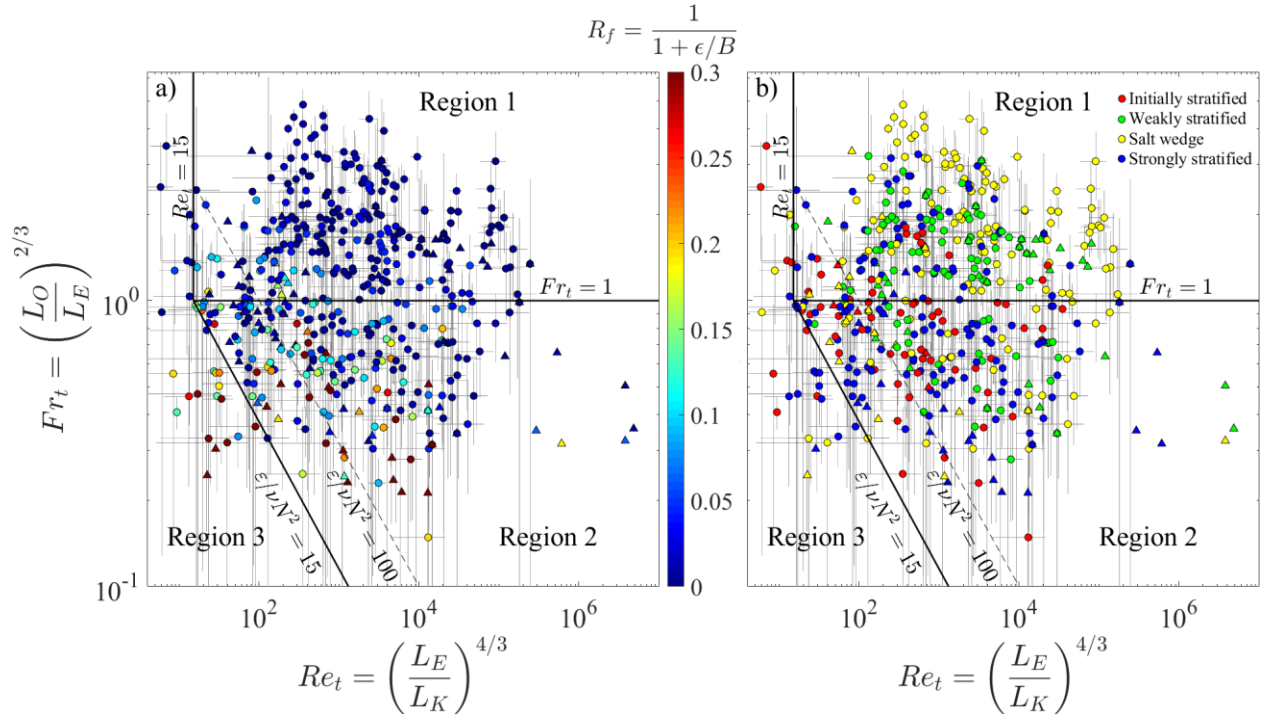
Figure 2.15: Turbulence measurements from all three ADVs plotted in the turbulent Froude number - Turbulent Reynolds number framework. Points are colored by a) Flux Richardson number and b) stratification event. Error bars are 95% confidence intervals, but triangular points have larger uncertainties than the observed values.
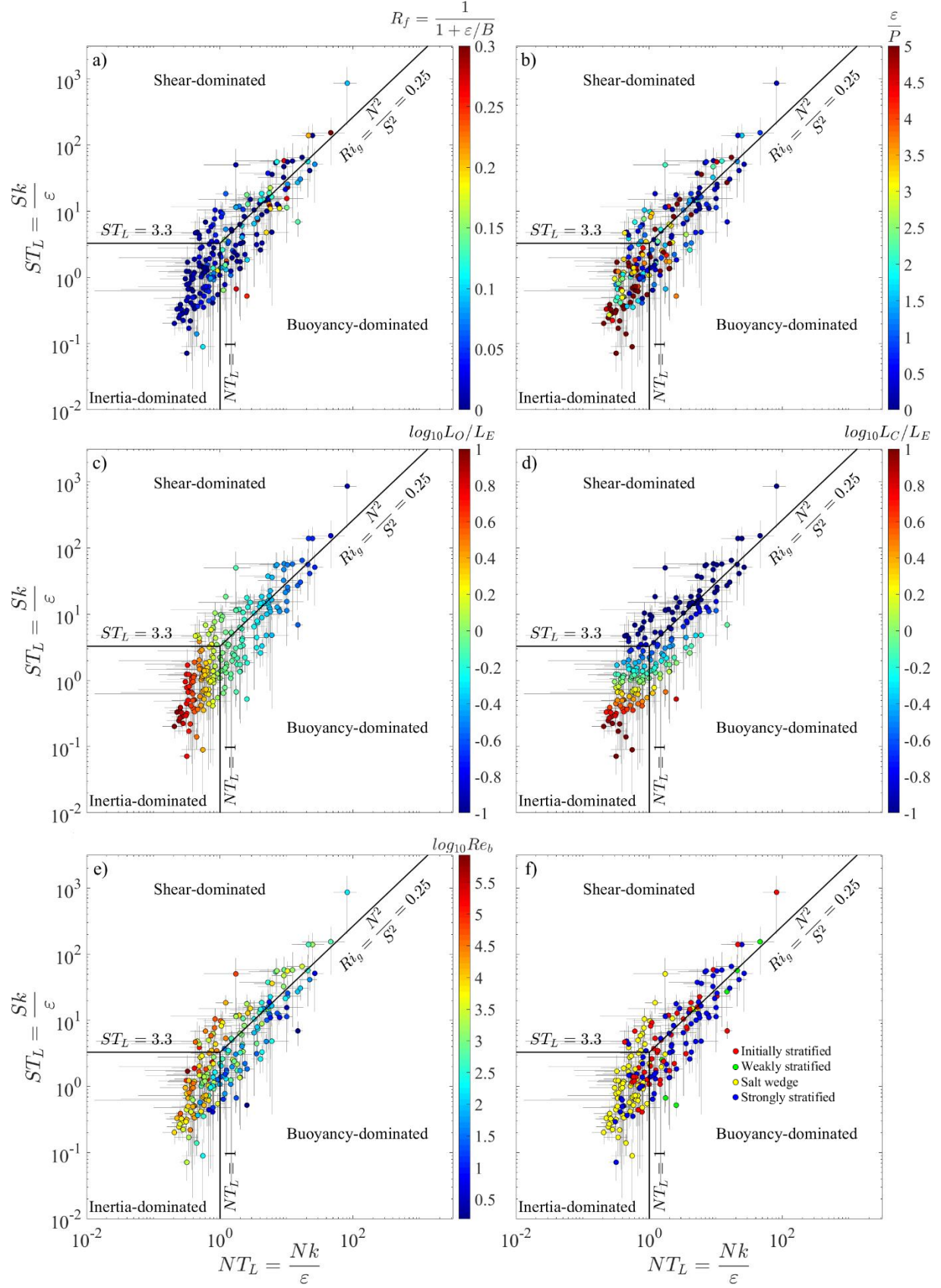
Figure 2.16: ST_L vs. NT_L colored by a) R_f, b) ε/P, c) L_O/L_E, d) L_C/L_E, e) $\log_{10} Re_b$, and f) stratification event. Error bars are 95% confidence intervals. Points with very large uncertainties are not shown.

REFERENCES

Akimoto, H. (2003). Global air quality and pollution. *Science*, *302*(5651), 1716-1719.

Benilov, A. Y., & Filyushkin, B. N. (1970). Application of methods of linear filtration to an analysis of fluctuations in the surface layer of the sea. *Izvestiya. Atmospheric and Oceanic Physics*, *6*, 810-819.

Bluteau, C. E., Jones, N. L., & Ivey, G. N. (2011). Estimating turbulent kinetic energy dissipation using the inertial subrange method in environmental flows. *Limnology and Oceanography: Methods*, *9*(7), 302-321.

Brethouwer, G., Billant, P., Lindborg, E., & Chomaz, J. M. (2007). Scaling analysis and simulation of strongly stratified turbulent flows. *Journal of Fluid Mechanics*, *585*, 343-368.

Corrsin, S. (1958). *Local isotropy in turbulent shear flow*. National Advisory Committee for Aeronautics RM 58B11.

Craig, P. D., & Banner, M. L. (1994). Modeling wave-enhanced turbulence in the ocean surface layer. *Journal of Physical Oceanography*, *24*(12), 2546-2559.

Davis, K. A., & Monismith, S. G. (2011). The modification of bottom boundary layer turbulence and mixing by internal waves shoaling on a barrier reef. *Journal of Physical Oceanography*, *41*(11), 2223-2241.

Dougherty, J. P. (1961). The anisotropy of turbulence at the meteor level. *Journal of Atmospheric and Terrestrial Physics*, *21*(2-3), 210-213.

Drazin, P. G., & Reid, W. H. (1981). *Hydrodynamic stability*. New York, NY: Cambridge University Press.

Dunckley, J. F., Koseff, J. R., Steinbuck, J. V., Monismith, S. G., & Genin, A. (2012). Comparison of mixing efficiency and vertical diffusivity models from temperature microstructure. *Journal of Geophysical Research: Oceans*, *117*(C10008).

Ellison, T. H. (1957). Turbulent transport of heat and momentum from an infinite rough plane. *J. Fluid Mech*, *2*(5), 456-466.

Emery, W. J., & Thomson, R. E. (2001). Data Analysis Methods in Physical Oceanography Elsevier. *Science BV Amsterdam, The Netherlands*.

Gargett, A. E. (1994). Observing turbulence with a modified acoustic Doppler current profiler. *Journal of Atmospheric and Oceanic Technology*, *11*(6), 1592-1610.

Geyer, W. R., Ralston, D. K., & Holleman, R. C. (2017). Hydraulics and mixing in a laterally divergent channel of a highly stratified estuary. *Journal of Geophysical Research: Oceans*, *122*, 4743–4760.

Geyer, W. R., Scully, M. E., & Ralston, D. K. (2008). Quantifying vertical mixing in estuaries. *Environmental Fluid Mechanics*, *8*(5-6), 495-509.

Grant, H. L., Stewart, R. W., & Moilliet, A. (1962). Turbulence spectra from a tidal channel. *Journal of Fluid Mechanics*, *12*(2), 241-268.

Gregg, M. C., D'Asaro, E. A., Riley, J. J., & Kunze, E. (2018). Mixing efficiency in the ocean. *Annual Review of Marine Science*, *10*, 443–473.

Gregg, M. C., Seim, H. E., & Percival, D. B. (1993). Statistics of shear and turbulent dissipation profiles in random internal wave fields. *Journal of physical oceanography*, *23*(8), 1777-1799.

Holleman, R. C., Geyer, W. R., & Ralston, D. K. (2016). Stratified turbulence and mixing efficiency in a salt wedge estuary. *Journal of Physical Oceanography*, *46*(6), 1769-1783.

Islam, M. R., & Zhu, D. Z. (2013). Kernel density–based algorithm for despiking ADV data. *Journal of Hydraulic Engineering*, *139*(7), 785-793.

Itsweire, E. C., Koseff, J. R., Briggs, D. A., & Ferziger, J. H. (1993). Turbulence in stratified shear flows: Implications for interpreting shear-induced mixing in the ocean. *Journal of Physical Oceanography*, *23*(7), 1508-1522.

Ivey, G. N., & Imberger, J. (1991). On the nature of turbulence in a stratified fluid. Part I: The energetics of mixing. *Journal of Physical Oceanography*, *21*(5), 650-658.

Kay, D. J., & Jay, D. A. (2003). Interfacial mixing in a highly stratified estuary 1. Characteristics of mixing. *Journal of Geophysical Research: Oceans*, *108*(C3), 3072.

Krvavica, N., Travaš, V., & Ožanić, N. (2016). A field study of interfacial friction and entrainment in a microtidal salt-wedge estuary. *Environmental fluid mechanics*, *16*(6), 1223-1246.

Luettich, R. A., Carr, S. D., Reynolds-Fleming, J. V., Fulcher, C. W., & McNinch, J. E. (2002). Semi-diurnal seiching in a shallow, micro-tidal lagoonal estuary. *Continental Shelf Research*, *22*(11), 1669-1681.

Luketina, D. A., & Imberger, J. (1989). Turbulence and entrainment in a buoyant surface plume. *Journal of Geophysical Research: Oceans*, *94*(C9), 12619-12636.

Lumley, J. L., & Terray, E. A. (1983). Kinematics of turbulence convected by a random wave field. *Journal of Physical Oceanography*, *13*(11), 2000-2007.

Mater, B. D., Schaad, S. M., & Venayagamoorthy, S. K. (2013). Relevance of the Thorpe length scale in stably stratified turbulence. *Physics of Fluids*, *25*(7), 076604.

Mater, B. D., & Venayagamoorthy, S. K. (2014). A unifying framework for parameterizing stably stratified shear-flow turbulence. *Physics of Fluids*, *26*(3), 036601.

Miles, J. W. (1961). On the stability of heterogeneous shear flows. *Journal of Fluid Mechanics*, 10(4), 496-508.

Monismith, S., Koseff, J., Walter, R., Squibb, M., Woodson, B., Davis, K., Pawlak, G. & Dunckley, J. (unpublished manuscript). Buoyancy fluxes in stratified flows: observations and parameterizations. *Journal of Physical Oceanography*, (Submitted).

Osborn, T. R. (1980). Estimates of the local rate of vertical diffusion from dissipation measurements. *Journal of Physical Oceanography*, *10*(1), 83-89.

Ozmidov, R. V. (1965). On the turbulent exchange in a stably stratified ocean. *Izv. Acad. Sci. USSR, Atmos. Oceanic Phys*, *1*(8), 853-860.

Paerl, H. W., Pinckney, J. L., Fear, J. M., & Peierls, B. L. (1998). Ecosystem responses to internal and watershed organic matter loading: consequences for hypoxia in the eutrophying Neuse River Estuary, North Carolina, USA. *Marine Ecology Progress Series*, *166*, 17-25.

Peltier, W. R., & Caulfield, C. P. (2003). Mixing efficiency in stratified shear flows. *Annual Review of Fluid Mechanics*, 35(1), 135-167.

Peters, H. (1997). Observations of stratified turbulent mixing in an estuary: Neap-to-spring variations during high river flow. *Estuarine, Coastal and Shelf Science*, *45*(1), 69-88.

Peters, H., & Bokhorst, R. (2000). Microstructure observations of turbulent mixing in a partially mixed estuary. Part I: Dissipation rate. *Journal of Physical Oceanography*, *30*(6), 1232-1244.

Pope, S. B. (2001). *Turbulent flows*. New York, NY: Cambridge University Press.

Rehmann, C. R., & Koseff, J. R. (2004). Mean potential energy change in stratified grid turbulence. *Dynamics of Atmospheres and Oceans*, *37*(4), 271-294.

Reynolds-Fleming, J. V., Fleming, J. G., & Luettich, R. A. (2002). Portable autonomous vertical profiler for estuarine applications. *Estuaries*, *25*(1), 142-147.

Robbins, J. C., & Bales, J. (1995). *Simulation of hydrodynamics and solute transport in the Neuse River Estuary* (No. 94-511). US Geological Survey; Earth Science Information Center, Open-File Reports Section.

Rohr, J. J., Itsweire, E. C., Helland, K. N., & Van Atta, C. W. (1988). An investigation of the growth of turbulence in a uniform-mean-shear flow. *Journal of Fluid Mechanics*, *187*, 1-33.

Rosman, J. H., & Gerbi, G. P. (2017). Interpreting fixed-location observations of turbulence advected by waves: Insights from spectral models. *Journal of Physical Oceanography*, *47*(4), 909-931.

Saddoughi, S. G., & Veeravalli, S. V. (1994). Local isotropy in turbulent boundary layers at high Reynolds number. *Journal of Fluid Mechanics*, *268*, 333-372.

Scotti, A. (2015). Biases in Thorpe-scale estimates of turbulence dissipation. Part II: energetics arguments and turbulence simulations. *Journal of Physical Oceanography*, *45*(10), 2522-2543.

Shih, L. H., Koseff, J. R., Ivey, G. N., & Ferziger, J. H. (2005). Parameterization of turbulent fluxes and scales using homogeneous sheared stably stratified turbulence simulations. *Journal of Fluid Mechanics*, *525*, 193-214.

Smyth, W. D., Moum, J. N., & Caldwell, D. R. (2001). The efficiency of mixing in turbulent patches: Inferences from direct simulations and microstructure observations. *Journal of Physical Oceanography*, *31*(8), 1969-1992.

Spigel, R. H., & Imberger, J. (1980). The classification of mixed-layer dynamics of lakes of small to medium size. *Journal of Physical Oceanography*, *10*(7), 1104-1121.

Stacey, M. T., Monismith, S. G., & Burau, J. R. (1999). Observations of turbulence in a partially stratified estuary. *Journal of Physical Oceanography*, *29*(8), 1950-1970.

Strang, E. J., & Fernando, H. J. S. (2001). Entrainment and mixing in stratified shear flows. *Journal of Fluid Mechanics*, *428*, 349-386.

Thorpe, S. A. (1977). Turbulence and mixing in a Scottish loch. *Philosophical Transactions of the Royal Society of London A: Mathematical, Physical and Engineering Sciences*, *286*(1334), 125-181.

Trowbridge, J., & Elgar, S. (2001). Turbulence measurements in the surf zone. *Journal of Physical Oceanography*, *31*(8), 2403-2417.

Venayagamoorthy, S. K., & Koseff, J. R. (2016). On the flux Richardson number in stably stratified turbulence. *Journal of Fluid Mechanics*, *798*.

Venayagamoorthy, S. K., & Stretch, D. D. (2010). On the turbulent Prandtl number in homogeneous stably stratified turbulence. *Journal of Fluid Mechanics*, *644*, 359-369.

Walter, R. K., Squibb, M. E., Woodson, C. B., Koseff, J. R., & Monismith, S. G. (2014). Stratified turbulence in the nearshore coastal ocean: Dynamics and evolution in the presence of internal bores. *Journal of Geophysical Research: Oceans*, *119*(12), 8709-8730.

Whipple, A. C., Luettich Jr, R. A., & Seim, H. E. (2006). Measurements of Reynolds stress in a wind-driven lagoonal estuary. *Ocean Dynamics*, *56*(3-4), 169-185.